ÉCOLE CENTRALE DE NANTES

MASTER CORO-IMARO
"CONTROL AND ROBOTICS"

2020 / 2021

Master Thesis Report

Presented by

Orcan Maktal

23 July 2021

Oscillation Control of an Underactuated Collaborative Parallel Robot

Supervisors & Jury

Jury:	Olivier KERMORGANT	Researcher at CNRS
	Isabelle FANTONI	Researcher at CNRS
Supervisor(s):	Sébastien BRIOT	Researcher at CNRS
	Vincent BÉGOC	Researcher at ICAM

Laboratory: Laboratoire des Sciences du Numérique de Nantes (LS2N)

Abstract

This master thesis presents robust trajectory planning methods that are used on an underactuated parallel robot, R-min. By their nature, underactuated mechanical systems have undesired residual oscillations when they are in action. This behavior is caused by elastic kind of like structure. Thus, the aim of this study is to annihilate residual oscillations or at least to attenuate to an acceptable level and to provide robustness with existing trajectory planning methods such as rest-to-rest trajectory planning and input shaping methods. Rest-to-rest trajectory planning method is an optimization based method which requires exact dynamic model of the system. Hence, this method is not robust against model uncertainties. On the contrary, input shaping methods provide robustness against model uncertainties upto some level. There are numerous input shaping methods in the literature but only 4 of them were selected to be implemented on a physical robot in the scope of this study. Mentioned rest-to-rest and other 4 input shaping methods were tested and compared with simple spline trajectory both in simulation and experiment. In the end, experimental results verified the predicted behavior of mentioned trajectory planning methods.

Keywords— underactuated, parallel robot, control, input shaping, rest-to-rest trajectory planning

Acknowledgments

I dedicate this thesis report to the loved ones I lost during this pandemic, sincerely thank to my beloved family and my fiancee for their undoubted trust in me and their support. I thank Prof. BRIOT and Prof. BÉGOC for giving me the opportunity to work on an interesting and recently emerging robotics field. I also thank PhD Guillaume JEANNEAU for his amical behavior and his cooperation. Last but not least, I thank to all Professors of IMARO who enlightened us and the staff who made life easier.

Notations

n : number of generalized coordinates
m : number of actuated generalized coordinates
r : number of unactuated generalized coordinates
k : maximum order of derivation to maintain required continuity
l : order of sliding-mode control
Δt : length of input shaper time
τ_d : undamped vibration period
$c(\cdot)$: abbreviation of $\cos(\cdot)$
$s(\cdot)$: abbreviation of $\sin(\cdot)$
$\boldsymbol{q}_1 = \begin{bmatrix} q_{11} & q_{21} \end{bmatrix}$: Actuated coordinates
$\boldsymbol{q}_2 = \begin{bmatrix} q_{12} & q_{22} \end{bmatrix}$: Proximal unactuated coordinates
$\boldsymbol{q}_3 = \begin{bmatrix} q_{13} & q_{23} \end{bmatrix}$: Distal unactuated coordinates
$\boldsymbol{q}_4 = \begin{bmatrix} q_4 & l_5 \end{bmatrix}$: Unactuated coordinates of preload bar
$\boldsymbol{M}$: Inertia matrix
$\boldsymbol{h}$: The vector of Coriolis, gravity and centrifugal effects
$\boldsymbol{J}$: The Jacobian matrix
t_{ss} : Settling-time

Abbreviations

UA : Underactuated
DoF : Degrees of Freedom
EE : End-effector
DGSP : Direct Geometrico-Static Problem
IGSP : Inverse Geometrico-Static Problem
IK : Inverse Kinematics
DKM : Direct Kinematic Model
IDM : Inverse Dynamic Model
CTC : Computed-Torque-Control
IS : Input Shaper
ZV IS : Zero-Vibration IS
ZVD IS : Zero-Vibration and Zero-Derivative IS
ZVDD IS : Zero-Vibration and Double Zero-Derivative IS
ZVDDD IS : Zero-Vibration and Triple Zero-Derivative IS
EI IS : Extra-Insensitive IS
TVIS : Time-Varying IS
MM IS : Multi-Mode IS
CDPR : Cable Driven Parallel Robot
STD : Standard Trajectories
RTR : Rest-to-Rest
P&P : Pick-and-Place
SI : Specified Insensitivity
DS : Dynamics Scaling
ODE : Ordinary Differential Equation
IVP : Initial Value Problem
BVP : Boundary Value Problem
RMS : Root-Mean-Square
SS : Steady-State

List of Figures

List of Tables

Contents

Introduction

With the technological advancements on the computational power of computers, recent advances in the control theory and demanding optimization problems arising from the energy consumption, weights and motor capabilities pushed researchers in a new field of robotics, *underactuated* (UA) robots. Thus, in the past decade, these robots have drawn attention by researchers increasingly in many aspects such as control [1][2][3][4][5][6][7], workspace analysis [8] and path planning [8][9][10][11][12][13]. These type of robots have major roles in space, mobile, structurally flexible robotics and underwater vehicles.

UA robots are characterized by their nature of having lesser actuators than the number of degrees-of-freedom (DoF) to be controlled, their nonlinear complex dynamics, *nonholonomic constraints* which are also known as the *internal dynamics*. The control of these systems are distinguished from other nonlinear systems. This property can be introduced in the design process for cost minimization, weight reduction and sufficient degrees of dexterity with extension of workspace [1][2][3][4][5][6][7].

R-min robot was designed to be used collaboratively in a work environment and to reduce the risk of injury in case of a collision with an operator. The robot design was based on the planar five-bar mechanism where 2 additional links are introduced on the forearms with passive revolute joints. This makes the robot a seven-bar mechanism with two degrees of underactuation. These additional DoF were taken care of by a passive link that connects the base and the *End-Effector* (EE) with a tension spring and a coupled revolute-prismatic joint pair at the base and a revolute joint at the EE [8][9].

Jeanneau et al. proposed a geometrico-static analysis of R-min robot to obtain forward and inverse geometric model and analysed it's workspace [8]. Moreover, these methods were used to obtain trajectories in joint level for static configurations of the robot. Later on, the authors used these trajectories in conventional PID *computed-torque-control* (CTC) to control R-min robot for *pick-and-place* (P&P) operations [9]. Ida et al. proposed *rest-to-rest* (RTR) trajectory planning for UA *cable driven parallel robot* (CDPR) whose dynamic model is perfectly known to eliminate undesired residual oscillations of the EE [10]. Then, Ida et al., by extending [10], proposed robust trajectory planning method, *input shaping* (IS), for UA CDPR which provides robustness against model uncertainties or parameter variations [11] which was detailed in [14]. Even more robust variations of this method were introduced in [15][16][17]. The implementation of one of the IS method was shown in [12]. Magee et al. pointed possible problems of ISs emerge from time and state dependence of dynamic parameters of flexible systems and proposed a method to overcome [18]. Thomsen et al. proposed *time-varying input shaper* (TVIS) for flexible systems[13]. These are some novel and existing trajectory planning methods for UA mechanical systems in the literature that are examined. Then, most suitable ones were implemented on R-min. In the end, their merits and demerits are elaborated and compared.

The aim of this study was, while exploiting the mentioned advantages of UA systems, to implement oscillation-free robust trajectory planning methods on an UA parallel robot, R-min, and to compare the performance in various criteria. After validating the success of mentioned methods in both simulation environment and experimentally, as expected, RTR, *zero-vibration and triple zero-derivative* (ZVDDD), *zero-vibration and double zero-derivative* (ZVDD), *extra-insensitive* (EI) and *zero-vibration and zero-derivative* (ZVD) methods were listed from best to worst in terms of residual oscillations.

The outline of this paper is developed as follows, in Section 1, detailed study of R-min is examined, in Section 2, trajectory planning methods in the literature are elaborated. Lastly, in Section 3, implemented trajectory methods are compared in terms of residual oscillation of unactuated coordinates, settling times and SS error of EE position.

Chapter 1

State of the art

1.1 Dynamics of underactuated systems

One of the distinguished property that differs UA systems from fully actuated systems is their dynamics. Robot dynamics are highly nonlinear systems that have been examined for decades in the sense of robustness, control, etc. In the last decade, UA systems have found their places in the literature because optimization demands have emerged day by day [1][2][3][4][5][6][7].

Conventional general dynamics equation of fully actuated systems can be represented as;

$$\mathbf{M}(\mathbf{q})\ddot{\mathbf{q}} + \mathbf{h}(\mathbf{q}, \dot{\mathbf{q}}) = \boldsymbol{\tau} \tag{1.1}$$

where $\mathbf{q} \in \mathbb{R}^n$ is the vector of generalized coordinates, $\mathbf{M(q)} \in \mathbb{R}^{n\times n}$ is the robot generalized inertia matrix(robot inertia matrix), $\mathbf{h}(\mathbf{q}, \dot{\mathbf{q}}) \in \mathbb{R}^n$ is the vector of Coriolis, centrifugal, gravity, friction effects and also spring effects (for R-min) and $\boldsymbol{\tau} \in \mathbb{R}^n$ is the vector of applied input force/torque to the system. For UA systems general dynamics equation can be represented as:

$$\begin{align}
\mathbf{M}(\mathbf{q})\ddot{\mathbf{q}} + \mathbf{h}(\mathbf{q}, \dot{\mathbf{q}}) &= \boldsymbol{u} \tag{1.2}\\
\begin{bmatrix} \mathbf{M}_{aa} & \mathbf{M}_{ad} \\ \mathbf{M}_{da} & \mathbf{M}_{dd} \end{bmatrix} \begin{bmatrix} \ddot{\mathbf{q}}_a \\ \ddot{\mathbf{q}}_d \end{bmatrix} + \begin{bmatrix} \mathbf{h}_a \\ \mathbf{h}_d \end{bmatrix} &= \begin{bmatrix} \boldsymbol{\tau} \\ \mathbf{0} \end{bmatrix} = \mathbf{u} \tag{1.3}\\
\mathbf{M}_{aa}\ddot{\mathbf{q}}_a + \mathbf{M}_{ad}\ddot{\mathbf{q}}_d + \mathbf{h}_a &= \boldsymbol{\tau} \tag{1.4}\\
\mathbf{M}_{da}\ddot{\mathbf{q}}_a + \mathbf{M}_{dd}\ddot{\mathbf{q}}_d + \mathbf{h}_d &= \mathbf{0} \tag{1.5}
\end{align}$$

Equation (1.3) is the decoupled system of Equation (1.2) where $\boldsymbol{u} \in \mathbb{R}^n$ combines the applied input $\boldsymbol{\tau}$ and null-input that comes from UA part, $\mathbf{M}_{aa} \in \mathbb{R}^{m\times m}$, $\mathbf{M}_{ad} \in \mathbb{R}^{m\times r}$, $\mathbf{M}_{dd} \in \mathbb{R}^{r\times r}$, $\mathbf{M}_{da} = \mathbf{M}_{ad}^T \in \mathbb{R}^{r\times m}$, $\mathbf{h}_a \in \mathbb{R}^m$, $\mathbf{h}_d \in \mathbb{R}^r$, $\boldsymbol{\tau} \in \mathbb{R}^m$ where n, m and $r = n - m$ are numbers of generalized, actuated generalized and unactuated generalized coordinates respectively.

By isolating $\ddot{\mathbf{q}}_a$ in Equation (1.4) and implementing to Equation (1.5) Equation (1.6) is obtained as;

$$\mathbf{M}_{da}\mathbf{M}_{aa}^{-1}(\boldsymbol{\tau} - \mathbf{M}_{ad}\ddot{\mathbf{q}}_d - \mathbf{h}_a) + \mathbf{M}_{dd}\ddot{\mathbf{q}}_d + \mathbf{h}_d = \mathbf{0} \tag{1.6}$$

Equation (1.6) is a second-order *nonholonomic constraint* also called as *internal dynamics*.

Equation (1.3) is provided in [9] and Equations (1.2), (1.4), (1.5) and (1.6) are obtained accordingly.

1.2 Holonomic constraints and nonholonomic constraints

1.2.1 Holonomic constraints

The DoF also indicates how to parametrize the *Configuration Space* (C-space) of the system. The C-space is denoted as a space that controlled coordinates are lying down. As an example, a five-bar mechanism has two DoF thus, C-space can be parametrized by two variables. This two-dimensional C-space is integrated into five-dimentional space. In the closed-loop form, two coordinate equations (x and y) and one angle equation are obtained whereas the configuration space size is five. Thus, two DoF are obtained by this way. These close-loop geometric equations are denoted as *holonomic constraints*. In the end, if the system is defined by n variables and subjected to k independent holonomic constraints that means the system has n-k DoF. These constraints are also called as *integrable constraints* since these geometric holonomic constraints also form velocity constraints. One can come back to these constraints by integrating velocity holonomic constraints [19][20].

1.2.2 Nonholonomic constraints

With holonomic constraints, one can determine the differential relationship between the state(s) and the input(s) as well as the close-loop geometric relationship. In contrast to holonomic constraints, with nonholonomic constraints, one can determine the differential relationship between the state(s) and the input(s) at best but not the close-loop geometric relationship. This indicates that the past state values are required in order to determine the current state. A vehicle is a good example because one nonholonomic constraint reduces some velocities of the vehicle and prevents it to slide directly to its sides but it does not reduce the configuration space. These side motions are still achievable by changing the wheel position while it is moving thus, the vehicle can reach any pose within it's 3-dimentional C-space [19][20].

UA mechanical systems have second-order nonholonomic behavior by their nature.

1.3 Design of R-min

In the literature, there is vast amount of UA serial kinematic structures. In comparison to parallel robots, serial robots have lower speed and stiffness whereas parallel robots have less workspace than serial robots. Thus, by introducing 2 passive links to forearms, the robot gains more workspace but also the weight does not increase relatively to the actuated configuration of the same seven-bar mechanism. The kinematic integrity of the system is maintained with a passive link that connects the base and the EE by a tension spring with coupled revolute-prismatic joint pair at the base and a revolute joint at the EE. In every engineering field, if there is a gain, there is a loss. In this case, residual oscillations on the passive additional joints is the loss [8].

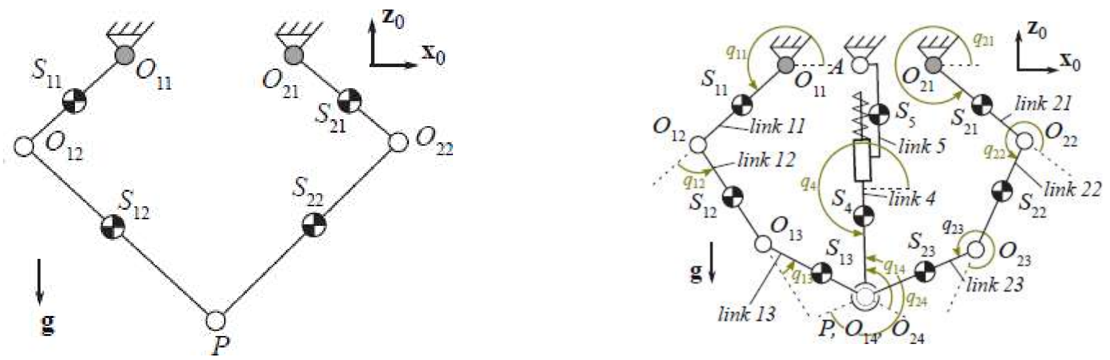

(a) Conventional five-bar mechanism

(b) R-min robot

Figure 1.1: Kinematic representation of five-bar and R-min [8]

Kinematic structure of R-min robot is represented in Figure 1.1b and it is composed of [8]:

- The robot has two actuated revolute joints on O_{i1}, and five passive revolute joints on O_{i2}, O_{i3} and P where (i=1,2).
- The mechanism has four DoF with two acuated joints. This makes the system UA with two unconstrained DoFs. In this form, the seven-bar mechanism is lack in stiffness, thus a passive mechanical system is composed of a passive link that connects the base and the EE by a tension spring with coupled revolute-prismatic joint pair at the base and a revolute joint at the EE. This passive system contributes the kinematic integrity of the system and also contributes as an elastic element.

R-min has more rigidity than UA seven-bar mechanism but less rigidity than conventional five-bar mechanism which is shown in Figure 1.1a. This makes R-min a good candidate to be utilized as a collaborative robot.

(a) Downward Force on the EE

(b) Asymmetric Upwards Force on the EE

(c) Asymmetric Upwards Force on the Intermediary Joint

(d) A human head in collision with R-min

Figure 1.2: Different configurations under different external forces [8]

In case of a collision which is represented in Figure 1.2d, the robot reconfigures itself and reduces the impact in comparison to five-bar mechanism. Whereas, in Figures 1.2a, 1.2b and 1.2c, it is shown that how forces acting on distal unactuated coordinate and EE changes the configuration of R-min. In case of downward forces, the EE position is obtained as if $l_{O_{i2}O_{i3}}$ is a rigid link and thus it acts like a five-bar mechanism which can be considered for pick and place operations [8].

The robot variables are listed as:

- $\mathbf{q}_a = [q_{11}\ q_{21}]^T$ is the vector of actuated joints, motorized at O_{i1} where $(i = 1, 2)$,
- $\mathbf{q}_d = [q_{12}\ q_{13}\ q_{22}\ q_{23}]^T$ is the vector of unactuated joints,
- $\mathbf{p} = [x\ z]^T$ is the position of the EE P,
- q_4 and $l_5 = ||\overrightarrow{AP}|| = \sqrt{x^2 + z^2}$ are the angle between $\mathbf{x}_0$ and the preload bar and the length of the preload bar respectively.

1.4 Specifications of R-min

The prototype has properties of:

- All links are made in aliminum hollow tubes, for link$_{11}$ and link$_{21}$ external diameter of 30mm, thickness of 5mm and for other links external diameter of 20mm, thickness of 2mm.
- Currently only positional measurements of actuated joint coordinates are measured (Velocities and accelerations are derived from position but acceleration is quite noisy).
- Tracking spring has stiffness of 80N/m and 0.2m length in the rest.
- Two direct drive SIMOTICS S-IFL6 are used (max torque is 70Nm, rated is torque 23.9Nm).
- Unactuated joints, q_{i3}, positions, velocities and accelerations are assumed as zero in control process and all the effects of these joints are disregarded.

1.5 Direct geometrico-static problem

Conventional robots have equilibrium positions which can be found from their holonomic constraints whereas for R-min robot, holonomic constraints are not sufficient to find the equilibrium positions but also gravitational effects, external forces and stiffness of the preload spring are required. This is caused by the unconstrained DoF in the mechanism. Thus, Jeanneau et al. proposed a method to solve the Direct Geometrico-Static Problem (DGSP) based on potential energy minimization of the system. As it can be understood from the the name, the method considers only the static configurations [8].

1.5.1 Problem definition of DGSP

Static positions exist in the solution of DGSP found by all configurations $\mathbf{q}_t = [\mathbf{p}^T \; \mathbf{q}_d^T]^T$ that minimizes the potential energy of the system subject to geometric constraints for a given set of actuated joint coordinates $\mathbf{q}_a$ [8].

1.5.2 Potential energy of the robot

Potential energy of the system is obtained from the potential energy, $U_{i,j}$, of the links (i, j) where $(i = 1, 2,\ j = 1, 2, 3)$ which depends on the masses m_{ij}, the position of the center of mass (CoM) S_{ij}, and the length l_{ij} of the links. O_{ij}, S_{ij} and O_{ij+1} are assumed to be aligned and $l_{S_{ij}}$ is the length of $||\overrightarrow{O_{ij}S_{ij}}||$. The extensive leg (prismatic joint), l_{S_4} is the distance between P and it's CoM S_4, l_{S_5} is the length between point A and it's CoM S_5, m_4, m_5 are their masses, U_4, U_5 are their potential energies respectively [8]. All these parameters are visualized in Figure 1.1b.

$$U_{i,1} = gm_{i1}l_{S_{i1}}\sin(q_{i1}) \tag{1.7}$$

$$U_{i,2} = gm_{i2}(l_{i1}\sin(q_{i1}) + l_{S_{i2}}\sin(q_{i1}+q_{i2})) \tag{1.8}$$

$$U_{i,3} = gm_{i3}(l_{i1}\sin(q_{i1}) + l_{i2}\sin(q_{i1}+q_{i2}) + l_{S_{i3}}\sin(q_{i1}+q_{i2}+q_{i3})) \tag{1.9}$$

$$U_4 = gm_4z(1 + \tfrac{l_{S_4}}{l_5}) \tag{1.10}$$

$$U_5 = gm_5l_{S_5}\sin(q_4) \tag{1.11}$$

$$U_S = \tfrac{1}{2}k(\sqrt{x^2+z^2} - l_0)^2 \tag{1.12}$$

where U_s is denoted as the potential energy caused by the spring, k is it's spring constant, and l_0 is the length in rest position. The total potential energy of the system becomes:

$$U = (\sum_{i=1}^{2}\sum_{j=1}^{3} U_{i,j}) + U_4 + U_5 + U_S - \mathbf{f}^T\mathbf{p} \tag{1.13}$$

where $\mathbf{f}$ is a conservative constant payload applied to the EE which shows up in the total potential energy.

The potential energy depends on $\mathbf{q}_a$, $\mathbf{q}_d$, $\mathbf{p}$ and $\mathbf{f}$. $\mathbf{q}_a$, $\mathbf{q}_d$ and $\mathbf{p}$ creates geometric holonomic constraint $\boldsymbol{\phi}(\mathbf{q}_a, \mathbf{q}_d, \mathbf{p}) = \mathbf{0} \in \mathbb{R}^4$ must be satisfied for any configuration and these constraints are shown below as:

$$\boldsymbol{\phi} = [\phi_{11}\ \phi_{12}\ \phi_{21}\ \phi_{22}]^T \tag{1.14}$$

$$\phi_{i1} = \overrightarrow{OO_{i1}}.\mathbf{x}_0 + l_{i1}\cos(q_{i1}) + l_{i2}\cos(q_{i1}+q_{i2}) + l_{i3}\cos(q_{i1}+q_{i2}+q_{i3}) - x \tag{1.15}$$

$$\phi_{i2} = \overrightarrow{OO_{i1}}.\mathbf{z}_0 + l_{i1}\sin(q_{i1}) + l_{i2}\sin(q_{i1}+q_{i2}) + l_{i3}\sin(q_{i1}+q_{i2}+q_{i3}) - z \tag{1.16}$$

where $i = (1, 2)$.

A solution to DGSP exists where U is at a local minima while Equation (1.14) is satisfied. This problem is formed as:

$$\mathbf{q}_t = argmin\ U(\mathbf{q}_a, \mathbf{q}_d, \mathbf{p}, \mathbf{f})\ subject\ to\ \boldsymbol{\phi}(\mathbf{q}_a, \mathbf{q}_d, \mathbf{p}) = \mathbf{0} \tag{1.17}$$

where $\mathbf{f}$ and $\mathbf{q}_a$ are kept constant.

This optimization problem is solved with Lagrange multipliers. The Lagrangian is defined as $\mathcal{L} = U + \boldsymbol{\lambda}^T\boldsymbol{\phi}$ where $\boldsymbol{\lambda} \in \mathbb{R}^4$ is the vector of Lagrange multipliers. Static equilibrium points can be found by solving:

$$\nabla_{\mathbf{q}_t} U(\mathbf{q}_a, \mathbf{q}_d, \mathbf{p}, \mathbf{f}) + \boldsymbol{\lambda}^T \nabla_{\mathbf{q}_t}\boldsymbol{\phi} = \mathbf{0},\ \boldsymbol{\phi}(\mathbf{q}_a, \mathbf{q}_d, \mathbf{p}) = \mathbf{0} \tag{1.18}$$

where $\nabla_{\mathbf{q}_t}$ denotes the gradient w.r.t. $\mathbf{q}_t$. The term $\boldsymbol{\lambda}$ is added into the Equation (1.18) because there exist 10 equations with only 6 parameters to be found.

A second-order condition is introduced because some equilibrium configurations are not stable in the solution space and it is given as:

$$\mathbf{H}^p = \mathbf{Z}^T\mathbf{H}\mathbf{Z} \succ 0 \tag{1.19}$$

where $\mathbf{H}$ is the Hessian of the Lagrangian obtained from the Hessian $\mathbf{H}^U_{\mathbf{q}_t}$ of the potential energy U w.r.t. the variables of $\mathbf{q}_t$ and from the Hessian $\mathbf{H}^{\phi_k}_{\mathbf{q}_t}$ of the holonomic constraint ϕ_k w.r.t. the variables of $\mathbf{q}_t$ as follows:

$$\mathbf{H} = \mathbf{H}^U_{\mathbf{q}_t} + \sum_k^4 \lambda_k \mathbf{H}^{\phi_k}_{\mathbf{q}_t} \tag{1.20}$$

$\mathbf{Z}$ is the kernel of $\nabla_{\mathbf{q}_t}\boldsymbol{\phi}$, i.e.

$$\nabla_{\mathbf{q}_t}\boldsymbol{\phi}\mathbf{Z} = \mathbf{0} \tag{1.21}$$

and Equations (1.7)-(1.21) are provided in [8].

Hessian

Assume V is a function to be minimized.

$$\underset{u}{min} V(\mathbf{u}, \mathbf{v}) \tag{1.22}$$

where $\mathbf{u}$, $\mathbf{v}$ are the variables to be found and parameters of the function respectively. The necessary condition to find the solution of Equation (1.21) is:

$$\frac{\partial V}{\partial \mathbf{u}} = \mathbf{0} \tag{1.23}$$

A function $\mathbf{f}$ is defined as $\mathbf{f}(\mathbf{u}, \mathbf{v}) = \frac{\partial V}{\partial \mathbf{u}^T}$ and zeros of this function are found. The Hessian of V is defined as the derivative of $\mathbf{f}$ w.r.t. $\mathbf{u}$ as:

$$\mathbf{H} = \frac{\partial \mathbf{f}}{\partial \mathbf{u}^T} \tag{1.24}$$

Let $\mathbf{u}_{(0)}$ is the solution of $\mathbf{f} = \mathbf{0}$. It will be a minimum for any variation $d\mathbf{u}_{(0)}$, the function V increases.

$$\forall d\mathbf{u}_{(0)},\ d\mathbf{u}_{(0)}^T \mathbf{H} d\mathbf{u}_{(0)} \tag{1.25}$$

where $\mathbf{H}$ should be positive definite and Equations (1.22)-(1.25) are provided in [21].

1.6 Inverse geometrico-static problem

1.6.1 Problem definition of IGSP

In the same sense of DGSP, Inverse Geometrico-Static Problem (IGSP) is examined to determine actuated and unactuated joints sequence $\mathbf{q}_{ad} = [\mathbf{q}_a^T\ \mathbf{q}_d^T]^T$ from desired trajectory positions $\mathbf{p}$ but it cannot be solved from the potential energy, since the compression of the preload bar is given by the position $\mathbf{p}$. Thus, equilibrium forces acting on the EE is examined [8].

1.6.2 Forces acting on the EE

The equilibrium configurations exist where total forces acting on the EE is zero ($\sum_{\mathbf{f}} = 0$) which is found by:

$$\sum\nolimits_{\mathbf{f}} = \mathbf{f}_{13} + \mathbf{f}_{23} + \mathbf{f}_4 + \mathbf{f} \tag{1.26}$$

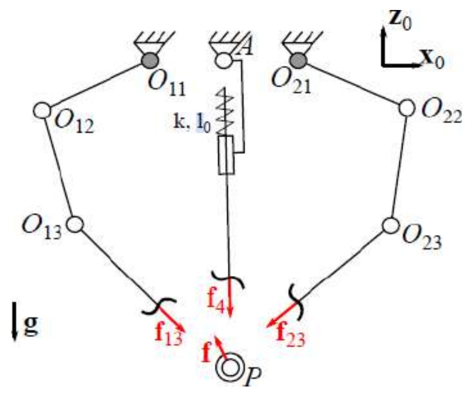

Figure 1.3: Forces acting on the EE [8]

With the assumption of no external forces acting on the links $(i2)$ and $(i3)$, gravity and joint forces form equilibrium forces applied by forearms $(i3)$ to the EE is shown in Figure 1.3 and their components are given as:

$$\mathbf{f}_{i3}^T \mathbf{x}_0 = \frac{g(m_{i\alpha} - m_{i\beta})}{\tan(\theta_{i3}) - \tan(\theta_{i2})} \tag{1.27}$$

$$\mathbf{f}_{i3}^T \mathbf{z}_0 = \frac{g(m_{i\alpha}\tan(\theta_{i3}) - m_{i\beta}\tan(\theta_{i2}))}{\tan(\theta_{i3}) - \tan(\theta_{i2})} \tag{1.28}$$

where $\theta_{i2} = q_{i1} + q_{i2}$, $\theta_{i3} = q_{i1} + q_{i2} + q_{i3}$ and

$$m_{i\alpha} = \frac{l_{S_{i2}}}{l_{i2}} m_{i2} + m_{i3}, \; m_{i\beta} = m_{i3} \frac{l_{S_{i3}}}{l_{i3}} \tag{1.29}$$

and components of the force of the preload system is given as:

$$\mathbf{f}_4^T \mathbf{x}_0 = -\left(k(l_0 - l_5) + \tfrac{\eta g}{l_5} \sin(q_4)\right) \cos(q_4) \tag{1.30}$$

$$\mathbf{f}_4^T \mathbf{z}_0 = -k(l_0 - l_5) \sin(q_4) + m_4 g + \tfrac{\eta g}{l_5} \cos^2(q_4) \tag{1.31}$$

where $\eta = l_{S_4} m_4 + l_{S_5} m_5$.

$$\begin{aligned} \mathbf{q}_{ad} = argmin \ \textstyle\sum_{\mathbf{f}}(\mathbf{q}_a, \mathbf{q}_d, \mathbf{p}, \mathbf{f}) \ subject \ to \ \boldsymbol{\phi}(\mathbf{q}_a, \mathbf{q}_d, \mathbf{p}) = \mathbf{0} \\ and \ \textstyle\sum_{\mathbf{f}}(\mathbf{q}_a, \mathbf{q}_d, \mathbf{p}, \mathbf{f}) = \mathbf{0} \end{aligned} \tag{1.32}$$

Equation (1.32) can be treated as the Equation (1.17) by following the same methodology and the Equations (1.26)-(1.32) are provided in [8].

1.7 Dynamic model of R-min

1.7.1 Kinematic model

Direct kinematic model

Kinematic model represents the relationship between velocities of system elements. Different from Sections 1.5 and 1.6 $\mathbf{q}_a \in \mathbb{R}^{4\times1}$ is defined as $\mathbf{q}_a = \begin{bmatrix} \mathbf{q}_1^T & \mathbf{q}_2^T \end{bmatrix}^T$ and $\mathbf{q}_d \in \mathbb{R}^{4\times1}$ is defined as $\mathbf{q}_d = \begin{bmatrix} \mathbf{q}_3^T & \mathbf{q}_4^T \end{bmatrix}^T$ where

$$\boldsymbol{A}\dot{\boldsymbol{p}} + \boldsymbol{B}\dot{\boldsymbol{q}}_a = \mathbf{0} \tag{1.33}$$

where $\mathbf{A} \in \mathbb{R}^{2\times2}$, $\mathbf{p} \in \mathbb{R}^{2\times1}$, $\mathbf{B} \in \mathbb{R}^{2\times4}$. $\boldsymbol{B}$ can be decomposed into:

$$\mathbf{B} = \begin{bmatrix} \mathbf{B}_1 \\ \mathbf{B}_2 \end{bmatrix} \tag{1.34}$$

Thus, Equation (1.33) can be written as:

$$\mathbf{A}\dot{\mathbf{p}} + \mathbf{B}_1\dot{\mathbf{q}}_1 + \mathbf{B}_2\dot{\mathbf{q}}_2 = 0 \tag{1.35}$$

In final form, DKM is written as:

$$\dot{\mathbf{p}} = -\mathbf{A}^{-1}\mathbf{B}\dot{\mathbf{q}}_a \tag{1.36}$$

$$\dot{\mathbf{p}} = \mathbf{J}\dot{\mathbf{q}}_a \tag{1.37}$$

Unactuated coordinate kinematics

Unactuated coordinate velocities can be expressed as:

$$\mathbf{J}_t\dot{\mathbf{p}} = \mathbf{J}_{ta}\dot{\mathbf{q}}_a + \mathbf{J}_{td}\dot{\mathbf{q}}_d \tag{1.38}$$

where $\mathbf{J}_t \in \mathbb{R}^{4\times2}$, $\mathbf{J}_{ta} \in \mathbb{R}^{4\times4}$ and $\mathbf{J}_{td} \in \mathbb{R}^{4\times4}$.

1.7.2 Second order kinematic model

Second order kinematic model can be expressed as:

$$\mathbf{A}\ddot{\mathbf{p}} = -\mathbf{B}_1\ddot{\mathbf{q}}_1 - \mathbf{B}_2\ddot{\mathbf{q}}_2 + \mathbf{b}_c \tag{1.39}$$

$$\mathbf{J}_t\ddot{\mathbf{p}} = \mathbf{J}_{ta}\ddot{\mathbf{q}}_a + \mathbf{J}_{td}\ddot{\mathbf{q}}_d + \mathbf{d}_c \tag{1.40}$$

where $\mathbf{b}_c$ and $\mathbf{d}_c$ are obtained as:

$$\mathbf{b}_c = -\dot{\mathbf{B}}_1\dot{\mathbf{q}}_1 - \dot{\mathbf{B}}_2\dot{\mathbf{q}}_2 \tag{1.41}$$

$$\mathbf{d}_c = \dot{\mathbf{J}}_{ta}\dot{\mathbf{q}}_a + \dot{\mathbf{J}}_{td}\dot{\mathbf{q}}_d \tag{1.42}$$

By isolating $\ddot{\mathbf{p}}$ in Equation (1.39), and implementing it into Equation (1.40), second order kinematics of unactuated coordinates is obtained as:

$$\ddot{\mathbf{q}}_d = \mathbf{J}_d\ddot{\mathbf{q}}_a + \mathbf{J}_{td}^{-1}(\mathbf{J}_t\mathbf{A}^{-1}\mathbf{b}_c - \mathbf{d}_c) \tag{1.43}$$

where

$$\mathbf{J}_d = \mathbf{J}_{td}^{-1}(\mathbf{J}_t\mathbf{J} - \mathbf{J}_{ta}) \tag{1.44}$$

1.7.3 Dynamic model

The dynamic model can be expressed as:

$$\begin{bmatrix} \boldsymbol{\tau} \\ \mathbf{0} \end{bmatrix} = \mathbf{M}\ddot{\mathbf{q}}_a + \mathbf{h} \tag{1.45}$$

Equation (1.45) can be decomposed into:

$$\boldsymbol{\tau} = \mathbf{M}_{11}\ddot{\mathbf{q}}_1 + \mathbf{M}_{12}\ddot{\mathbf{q}}_2 + \mathbf{h}_1 \tag{1.46}$$

$$\mathbf{0} = \boldsymbol{M}_{21}\ddot{\mathbf{q}}_1 + \mathbf{M}_{22}\ddot{\mathbf{q}}_2 + \mathbf{h}_2 \tag{1.47}$$

By isolating $\ddot{\boldsymbol{q}}_2$ in (1.47) and implement it into Equation (1.46), Equation (1.49) is obtained as:

$$\ddot{\mathbf{q}}_2 = -\mathbf{M}_{22}^{-1}(\mathbf{M}_{21}\ddot{\mathbf{q}}_1 + \mathbf{h}_2) \tag{1.48}$$

$$\boldsymbol{\tau} = (\mathbf{M}_{11} - \mathbf{M}_{12}\mathbf{M}_{22}^{-1}\mathbf{M}_{21})\ddot{\mathbf{q}}_1 + \mathbf{h}_1 - \mathbf{M}_{12}\mathbf{M}_{22}^{-1}\mathbf{h}_2 \tag{1.49}$$

Expression of $\ddot{\boldsymbol{q}}_1$ from $\ddot{\boldsymbol{p}}$

By multiplying Equation (1.49) with $\boldsymbol{B}_2$, Equation (1.50) is obtained as:

$$\mathbf{B}_2\ddot{\mathbf{q}}_2 = -\mathbf{B}_2\mathbf{M}_{22}^{-1}(\mathbf{M}_{21}\ddot{\mathbf{q}}_1 + \mathbf{h}_2) \tag{1.50}$$

By using Equations (1.39) and (1.50), (1.51) is obtained as:

$$\mathbf{A}\ddot{\mathbf{p}} + \mathbf{B}_1\ddot{\mathbf{q}}_1 - \mathbf{B}_2\mathbf{M}_{22}^{-1}(\mathbf{M}_{21}\ddot{\mathbf{q}}_1 + \mathbf{h}_2) = \mathbf{b}_c \tag{1.51}$$

and finally, by isolating $\ddot{\boldsymbol{q}}_1$ in Eqn. (1.51) and $\ddot{\boldsymbol{q}}_1$ is obtained in terms of $\ddot{\boldsymbol{p}}$ as:

$$\ddot{\mathbf{q}}_1 = (\mathbf{B}_1 - \mathbf{B}_2\mathbf{M}_{22}^{-1}\mathbf{M}_{21})^{-1}(-\mathbf{A}\ddot{\mathbf{p}} + \mathbf{B}_2\mathbf{M}_{22}^{-1}\mathbf{h}_2 + \mathbf{b}_c) \tag{1.52}$$

1.7.4 Implementation of friction in the dynamic model

Friction model definition

Friction model of any joint is simply considered as:

$$f_{s_q} = k_q atan(l_q \dot{q}) \tag{1.53}$$

where k_q, l_q are the friction coefficients of corresponding joint and $\dot{q}$ is the joint velocity.

Friction model implementation

Friction model implementation for R-min is computed as:

$$-\mathbf{f}_{f_a} + \mathbf{u} = -\mathbf{f}_{f_a} + \begin{bmatrix}\boldsymbol{\tau}\\ \mathbf{0}\end{bmatrix} = \frac{d}{dt}\frac{\partial L}{\partial \dot{\mathbf{q}}_a} - \frac{\partial L}{\partial \mathbf{q}_a} + \mathbf{A}_q^T \boldsymbol{\lambda} \tag{1.54}$$

$$-\mathbf{f}_{f_d} = \frac{d}{dt}\frac{\partial L}{\partial \dot{\mathbf{q}}_d} - \frac{\partial L}{\partial \mathbf{q}_d} + \mathbf{B}_q^T \boldsymbol{\lambda} \tag{1.55}$$

where

$$\mathbf{f}_{f_a} = \begin{bmatrix} k_{q_{11}} atan(l_{q_{11}} \dot{q}_{11}) & k_{q_{21}} atan(l_{q_{21}} \dot{q}_{21}) & k_{q_{12}} atan(l_{q_{12}} \dot{q}_{12}) & k_{q_{22}} atan(l_{q_{22}} \dot{q}_{22}) \end{bmatrix}^T \tag{1.56}$$

$$\mathbf{f}_{f_d} = \begin{bmatrix} k_{q_{13}} atan(l_{q_{13}} \dot{q}_{13}) & k_{q_{23}} atan(l_{q_{23}} \dot{q}_{23}) & k_{q_4} atan(l_{q_4} \dot{q}_4) & k_{l_5} atan(l_{l_5} \dot{l}_5) \end{bmatrix}^T \tag{1.57}$$

By isolating $\boldsymbol{\lambda}$ in Equation (1.55) and implementing it into Equation (1.54), Equation (1.58) is obtained as:

$$-\mathbf{f}_{f_a} + \mathbf{u} = \underbrace{\begin{bmatrix}\mathbf{I} & \mathbf{J}_d^T & \mathbf{J}^T\end{bmatrix} \mathbf{M}_t \begin{bmatrix}\mathbf{I}\\ \mathbf{J}_d\\ \mathbf{J}\end{bmatrix}}_{\mathbf{M}} \ddot{\mathbf{q}}_a + \underbrace{\begin{bmatrix}\mathbf{I} & \mathbf{J}_d^T & \mathbf{J}^T\end{bmatrix} (\mathbf{h}_t + \mathbf{M}_t \begin{bmatrix}\mathbf{0}\\ \mathbf{a}_d\\ \mathbf{a}_t\end{bmatrix})}_{\mathbf{h}} + \mathbf{f}^\star_{fd} \tag{1.58}$$

where

$$\mathbf{f}_{fa} = \begin{bmatrix}\mathbf{f}_{f_{a1}}\\ \mathbf{f}_{f_{a2}}\end{bmatrix} \tag{1.59}$$

$$\mathbf{f}^\star_{fd} = \mathbf{J}_d^T \mathbf{f}_{f_d} = \begin{bmatrix}\mathbf{f}^\star_{f_{d1}}\\ \mathbf{f}^\star_{f_{d2}}\end{bmatrix} \tag{1.60}$$

Equations (1.59) and (1.60) represent the friction forces caused by actuated and unactuated coordinates respectively. Thus, friction model in dynamic model is established as:

$$-\mathbf{f}_{f_{a1}} + \boldsymbol{\tau} = \mathbf{M}_{11}\ddot{\mathbf{q}}_1 + \mathbf{M}_{12}\ddot{\mathbf{q}}_2 + \mathbf{h}_1 + \mathbf{f}^\star_{f_{d1}} \tag{1.61}$$

$$-\mathbf{f}_{f_{a2}} = \mathbf{M}_{21}\ddot{\mathbf{q}}_1 + \mathbf{M}_{22}\ddot{\mathbf{q}}_2 + \mathbf{h}_2 + \mathbf{f}^\star_{f_{d2}} \tag{1.62}$$

By isolating $\ddot{\mathbf{q}}_2$ in Equation (1.62), Equation (1.63) is obtained as:

$$\ddot{\mathbf{q}}_2 = -\mathbf{M}_{22}^{-1}(\mathbf{f}_{f_{a2}} + \mathbf{M}_{21}\ddot{\mathbf{q}}_1 + \mathbf{h}_2 + \mathbf{f}^\star_{f_{d2}}) \tag{1.63}$$

By multiplying Equation (1.63) with $\mathbf{B}_2$, Equation (1.64) is obtained as:

$$\mathbf{B}_2\ddot{\mathbf{q}}_2 = -\mathbf{B}_2\mathbf{M}_{22}^{-1}(\mathbf{f}_{f_{a2}} + \mathbf{M}_{21}\ddot{\mathbf{q}}_1 + \mathbf{h}_2 + \mathbf{f}^{\star}_{f_{d2}}) \tag{1.64}$$

By using Equations (1.39) and (1.64), Equation (1.65) is obtained as:

$$\mathbf{A}\ddot{\mathbf{p}} + \mathbf{B}_1\ddot{\mathbf{q}}_1 - \mathbf{B}_2\mathbf{M}_{22}^{-1}(\mathbf{f}_{f_{a2}} + \mathbf{M}_{21}\ddot{\mathbf{q}}_1 + \mathbf{h}_2 + \mathbf{f}^{\star}_{f_{d2}}) = \mathbf{b}_c \tag{1.65}$$

and finally, by isolating $\ddot{\mathbf{q}}_1$ in Equation (1.65), Equation (1.66) is obtained as:

$$\ddot{\mathbf{q}}_1 = (\mathbf{B}_1 - \mathbf{B}_2\mathbf{M}_{22}^{-1}\mathbf{M}_{21})^{-1}(-\mathbf{A}\ddot{\mathbf{p}} + \mathbf{B}_2\mathbf{M}_{22}^{-1}\mathbf{f}_{f_{a2}} + \mathbf{B}_2\mathbf{M}_{22}^{-1}\mathbf{h}_2 + \mathbf{B}_2\mathbf{M}_{22}^{-1}\mathbf{f}^{\star}_{f_{d2}} + \mathbf{b}_c) \tag{1.66}$$

Estimation of friction coefficients

First, joint level trajectories are obtained from *Inverse Dynamic Model* (IDM) for given EE trajectories without friction model. After that, trajectories are implemented and validated with experimentation. Then, an optimization process is established to fit joint positions and torques obtained from IDM into joint positions and torques obtained from encoders. For this process, optimization parameters are 16 friction parameters for 8 joints.

1.7.5 Implementation of IDM

IDM is computed with the Equations (1.33)-(1.52) and implemented in the *Matlab* environment. The system of equations is solved as *ordinary differential equations* (ODEs) with built-in Matlab function *ode45*. This system is classified as *initial value problem* (IVP) with states $\begin{bmatrix}\boldsymbol{q}_a & \dot{\boldsymbol{q}}_a\end{bmatrix} = \begin{bmatrix}\boldsymbol{q}_1 & \boldsymbol{q}_2 & \dot{\boldsymbol{q}}_1 & \dot{\boldsymbol{q}}_2\end{bmatrix}$. The knowledge of initial state values are obtained from static configuration solution by IGSP shown in Section 1.6. The inputs of the system are position and acceleration of EE positions, $\boldsymbol{p}$ and $\ddot{\boldsymbol{p}}$ respectively. For each time instant, ODE computes the state values by integrating from $\ddot{\boldsymbol{q}}_a$. The computation diagram of the dynamic model is shown in Figure 1.4.

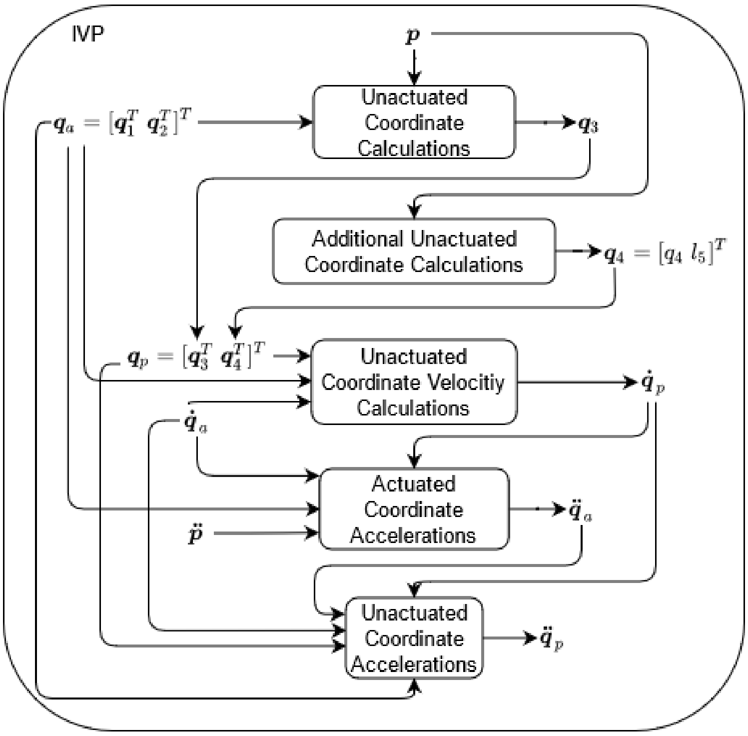

Figure 1.4: Dynamic model in the form of IVP

1.8 Control of R-min

Passing from EE space to joint space, either with IGSP or IDM, necessary computations which are elaborated in Sections 1.6 and 1.7 must be calculated. Then, trajectories in joint space can be given to the system to compute necessary input $\boldsymbol{\tau}$.

Jeanneau et al. assumed link$_{i2}$, link$_{i3}$ and the EE position are perfectly aligned for the simplicity of the control. Thus q_{i3}, $\dot{q}_{i3}$, $\ddot{q}_{i3}$ are considered as 0 during motion [9]. Of course, due to UA nature of the robot leads to error in the EE position while tracking a pick-and-place trajectory. Simulation results and the tracking error are shown in Figure 1.5.

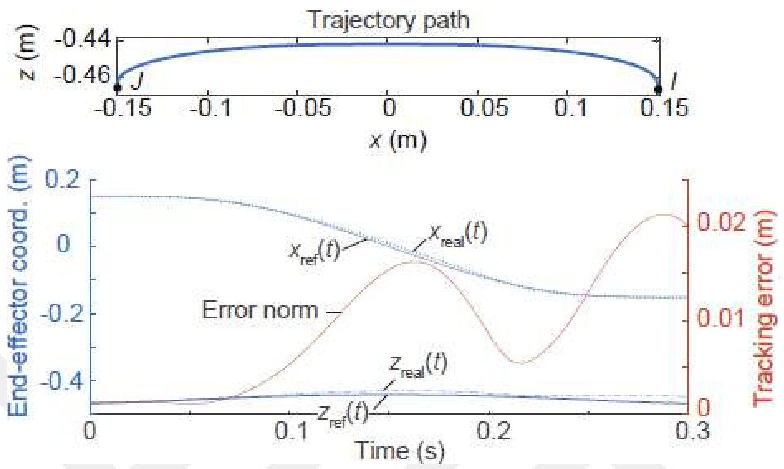

Figure 1.5: Pick-and-place trajectory (up), simulation results and tracking error (down) [9]

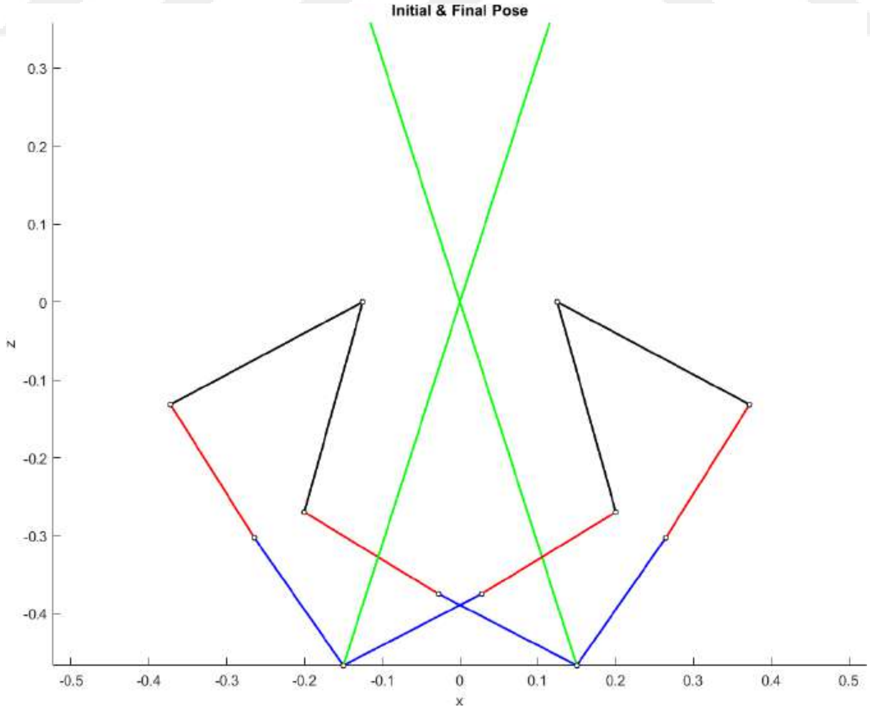

Figure 1.6: Kinematic representation of initial (right) and final (left) positions of R-min for P&P operation

Jeanneau et al. by using the IGSP solution [8], obtained static trajectories and used it to drive R-min for given trajectories. PID Computed torque control (CTC) diagram of R-min robot is shown in Figure 1.7.

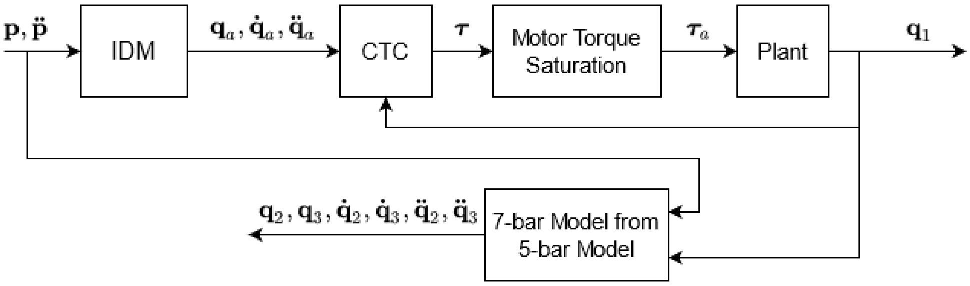

Figure 1.7: Control diagram of R-min

Position and acceleration of EE position, is obtained from spline trajectory. Then, by giving it to IDM, $\mathbf{q}_a = \begin{bmatrix} \mathbf{q}_1^T & \mathbf{q}_2^T \end{bmatrix}^T$ are obtained. Actuated and proximal passive coordinate positions, velocities and accelerations are given to CTC. Since the motor rated torques are limited, torque saturation is applied. Finally, applied torques $\boldsymbol{\tau}_a$ are given to R-min. There are 2 sensor measurements obtained from the system which are online encoder sensor measurement located on actuated coordinates $\mathbf{q}_1$ and offline high framerate camera that measures blobs located on each revolute joint in the system. Thus, actual positions of all joint and EE are obtained by image processing with high precision and the results are compared with simulations. Simulations are made in the *Adams* environment that is controlled with PID CTC in *Simulink* integrated with *Adams*. The simulation and experimental results of IGSP trajectory is shown in Figures 1.8 and 1.9 as:

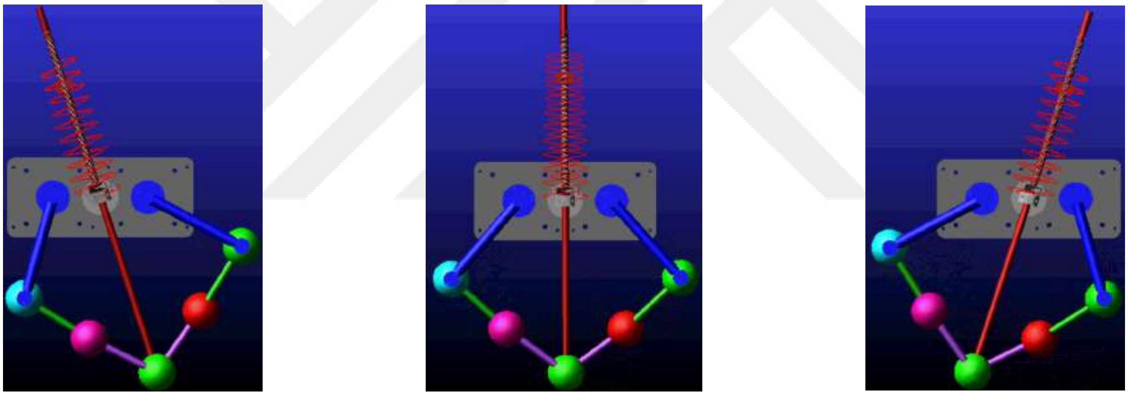

(a) t=0s (b) t=0.185s (c) t=0.55s

Figure 1.8: IGSP (Trial 3) in *Adams* simulation environment

(a) t=0s (b) t=0.185s (c) t=0.55s

Figure 1.9: IGSP (Trial 3) on R-min

Chapter 2

Trajectory planning for UA system

Trajectory planning has been used for decades in kinematic and dynamic level to control mechanical systems. In the last decade, a search of new ways to plan trajectories emerges in the field of UA robotics as well as the control strategies for these systems. Trajectory planning has a key role for the elimination of residual oscillations. For P&P operations, initial positions, velocities and accelerations are the essential considerations. In spite of this, intermediary positions, velocities and accelerations have no importance except feasibility problems of actual systems. Existing trajectory planning method for R-min is obtained by creating a spline trajectory between 2 stationary points in EE level. Then by giving these points to IGSP, trajectories are obtained in joint level [8]. This method is only applicable to slow (static) motion. On the other hand, applying this trajectory as a fast motion introduces residual oscillations to the system. To achieve fast and stable motion, dynamics of the system must be considered. Thus, five methods which are suitable in this sense, were investigated in the scope of this study. First one, RTR trajectory planning, proposes to use *boundary conditions* (BCs) to define the problem and solves it numerically with optimization techniques which does not consider model uncertainties [10]. The remaining ones are IS methods which take into account the model uncertainties and provide robustness against them [11][12][13][14][15][16][17][18]. The only drawback of IS methods is that the introduced time delay to the original (unshaped) trajectory. However, for RTR trajectory, the time of motion is predefined. The compromise is between residual unactuated coordinate oscillations and the time of motion. For P&P operations the speed is essential thus RTR is the first choice. In Section 3, simulation and experimental results are compared and it is concluded that RTR has acceptable residual oscillations and faster than ISs by far.

2.1 RTR trajectory planning

Ida et al. investigated a method to eliminate residual oscillations while tracking a predetermined geometrically constrained trajectory between 2 static poses within predetermined time for an underactuated CDPR whose dynamic equation is subject to Equation (1.3). The robot is controlled by 3 cables which are connected to the moving platform whose position $\mathbf{p} = [x, y, z]$ and orientation (in Euler angles) $\boldsymbol{\epsilon} = [\phi, \theta, \chi]$ but only the position of the EE is controlled.

The mentioned spatial robot has three actuated coordinates, $m = 3$, $n = 6$ generalized coordinates and thus three unactuated coordinates, $r = 3$ and whose dynamics are perfectly known.

The method proposes for actuated joints $\mathbf{q}_a = \mathbf{q}_a(u(t))$ where $u(t)$ is the motion law with initial and final states $u(0) = 0$ and $u(T)$=1 where T is the duration of motion. To fulfill the necessary conditions of transition between 2 stationary poses are taken care of boundary conditions. The continuity and the differentiability of the motion law are essentials. To achieve the motion without residual oscillations, stationary conditions of $\mathbf{q}_d$ should also be considered for BCs which can be obtained by isolating $\ddot{\mathbf{q}}_d$ in Equation (1.5). To solve it, state-space representation is introduced as [10]:

$$\mathbf{x} = \begin{bmatrix} \mathbf{q}_d \\ \dot{\mathbf{q}}_d \end{bmatrix} \tag{2.1}$$

$$\dot{\mathbf{x}} = \begin{bmatrix} \dot{\mathbf{q}}_d \\ -\mathbf{M}_{dd}^{-1}(\mathbf{M}_{da}\ddot{\mathbf{q}}_a + \mathbf{h}_d) \end{bmatrix} = \mathbf{f}(\mathbf{x}, \mathbf{q}_a, \dot{\mathbf{q}}_a, \ddot{\mathbf{q}}_a) \tag{2.2}$$

The BCs for RTR trajectory are given as:

$$\mathbf{x}(0) = \begin{bmatrix} \mathbf{q}_d(\mathbf{q}_a(0)) \\ \mathbf{0} \end{bmatrix} \tag{2.3}$$

$$\mathbf{x}(T) = \begin{bmatrix} \mathbf{q}_d(\mathbf{q}_a(T)) \\ \mathbf{0} \end{bmatrix} \tag{2.4}$$

where $\mathbf{q}_a(0)$ and $\mathbf{q}_a(T)$ are the stable equilibrium poses of the actuated coordinates and $\mathbf{q}_d(\mathbf{q}_a(0))$ and $\mathbf{q}_d(\mathbf{q}_a(T))$ are the stable equilibrium poses of the unactuated coordinates at the static equilibrium poses of the actuated coordinates. $\dot{\mathbf{x}} \in \mathbb{R}^{2r}$ and only $2r$ can be satisfied out of $4r$ proposed by Equations (2.3) and (2.4). Thus, additional $2r$ amount of scalar optimization parameters, $\boldsymbol{\kappa} = [\kappa_1, \cdots, \kappa_{2r}] \in \mathbb{R}^{2r}$ are introduced to solve the problem to convert actuated coordinates into $\mathbf{q}_a = \mathbf{q}_a(\boldsymbol{\kappa}, t)$. And boundary value problem (BVP) becomes [10]:

$$\begin{gathered} \dot{\mathbf{x}} = \mathbf{f}(\mathbf{x}(\boldsymbol{\kappa}, t), \mathbf{q}_a(\boldsymbol{\kappa}, t), \dot{\mathbf{q}}_a(\boldsymbol{\kappa}, t), \ddot{\mathbf{q}}_a(\boldsymbol{\kappa}, t)) \\ \mathbf{x}(0) = \mathbf{x}_0, \quad \mathbf{x}(T) = \mathbf{x}_T \end{gathered} \tag{2.5}$$

The motion law should be designed so that actuated coordinates can fulfill the initial and final conditions defined by the task. So, a function $\gamma(\boldsymbol{\kappa}, t)$ is introduced to modify the motion law $u(\gamma((\boldsymbol{\kappa}, t))$ which is defined as:

$$u(\gamma(\boldsymbol{\kappa}, t)) = \textstyle\sum_{i=k+1}^{2k+1} a_i \gamma^i(\boldsymbol{\kappa}, t) \tag{2.6}$$

$$\gamma(\boldsymbol{\kappa}, 0) = 0, \quad \gamma(\boldsymbol{\kappa}, T) = 1, \quad \forall \boldsymbol{\kappa} \in \mathbb{R} \tag{2.7}$$

where

$$a_i = \frac{(-1)^{i-k-1}(2k+1)!}{i.k!(i-k-1)!(2k+1-i)!} \tag{2.8}$$

and k denotes the maximum order of derivation upto required continuity.

Ida et al. decided to go with $k = 3$ to impose the continuity of the jerk for start and end positions. $\gamma(\boldsymbol{\kappa}, t)$ is chosen as:

$$\gamma(\boldsymbol{\kappa}, t) = \alpha t + \sum_{i=2}^{2r+1} \kappa_{i-1} t^i, \;\; \alpha = \frac{1 - \sum_{i=2}^{2r+1} \kappa_{i-1} T^i}{T} \tag{2.9}$$

In the end, actuated coordinates has a shape of $\mathbf{q}_a(u(\gamma(\boldsymbol{\kappa}, t))$ and by chain rule, $\dot{\mathbf{q}}_a$ is obtained as:

$$\dot{\mathbf{q}}_a = \frac{\partial \mathbf{q}_a}{\partial u} \frac{\partial u}{\partial \gamma} \frac{\partial \gamma}{\partial t} = \mathbf{q}_a' u^* \dot{\gamma} \tag{2.10}$$

and the second-order derivation of a chain derivative is a cumbersome process and not elaborated here and given as:

$$\ddot{\mathbf{q}}_a = \mathbf{q}_a''(u^* \dot{\gamma})^2 + \mathbf{q}_a'(u^* \ddot{\gamma} + u^{**} \dot{\gamma}^2) \tag{2.11}$$

where $(\cdot)'$ and $(\cdot)^*$ are partial derivatives w.r.t. u and γ respectively. One should note that, for the case $r \geq 2$ and Equation (2.7) is satisfied, there is nothing to be imposed for $\gamma(\boldsymbol{\kappa}, t)$.

Solution of the RTR can be found numerically but it does not guarantee success. Thus, Ida et al. imposed IVP instead of BVP by excluding the final state, $\mathbf{x}(T)$ because the solution was not obtained. The IVP is defined as:

$$\dot{\mathbf{x}} = \mathbf{f}(\mathbf{x}(\boldsymbol{\kappa}, t), \mathbf{q}_a(\boldsymbol{\kappa}, t), \dot{\mathbf{q}}_a(\boldsymbol{\kappa}, t), \ddot{\mathbf{q}}_a(\boldsymbol{\kappa}, t)) \tag{2.12}$$

$$\mathbf{x}(0) = \mathbf{x}_0 \tag{2.13}$$

Ida et al. proposed an optimization method to minimize a function $\mathbf{F}$ to satisfy the end conditions, Equation (2.4), of the BVP with unkown $\boldsymbol{\kappa}$ as:

$$\mathbf{F}(\boldsymbol{\kappa}) = \mathbf{x}(\boldsymbol{\kappa}, T) - \mathbf{x}_T = \mathbf{0} \tag{2.14}$$

Equations (2.1)-(2.14) are given and the aforementioned optimization process is detailed in [10]. Some of the experimental results using the methodology examined above are shown below as:

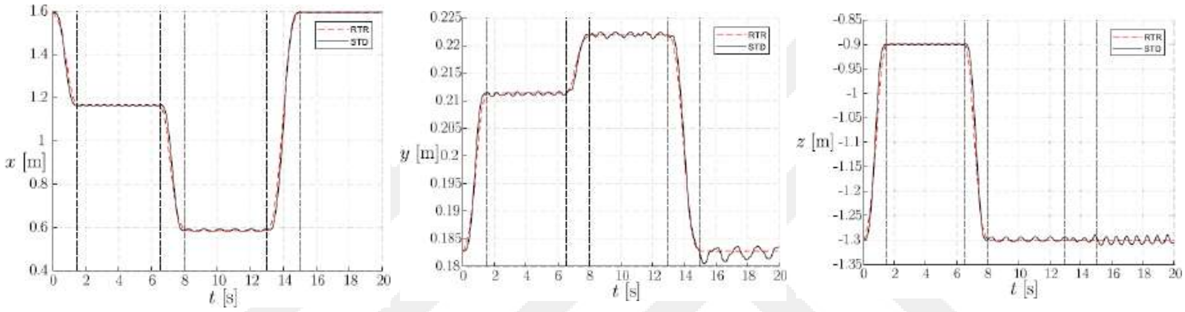

(a) x (b) y (c) z

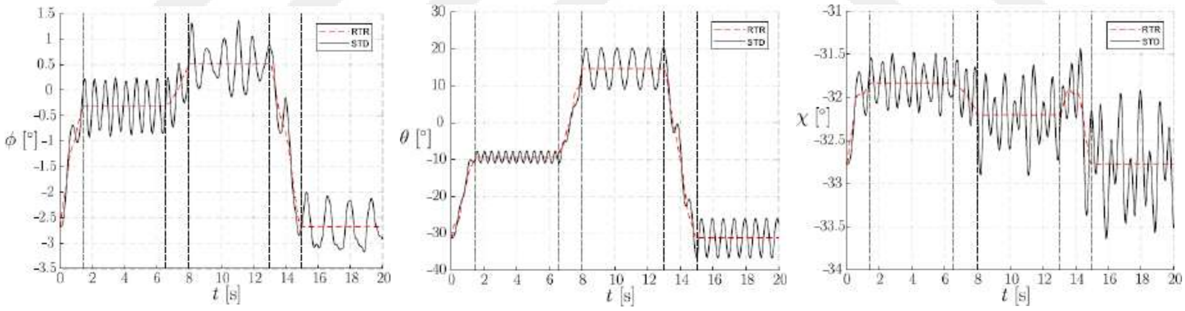

(d) ϕ (e) θ (f) χ

Figure 2.1: EE Positions and orientations with different trajectory planning [10]

In Figure 2.1 proposed RTR trajectory planning method is compared with *Standard Trajectories* (STD) which were created with splines. It is clearly seen that, RTR trajectory planning method eliminates residual oscillations for the UA CDPR.

2.1.1 RTR trajectory planning on R-min

BVP is an extension IVP which is shown in Figure 1.4. Additional to initial state values, final state values are also imposed to define the bounds of the ODE problem. For R-min, these bound conditions are initial and final positions, velocities and accelerations of $\mathbf{q}_1$, $\mathbf{q}_2$ and $\mathbf{q}_3$. RTR trajectory planning method does not only satisfy these bounds as constraints but also lowers residual oscillations of the distal unactuated coordinates $\mathbf{q}_3$. Such computationally expensive operation can be handled with optimization. *Matlab* provides wide variety of optimization methods in its toolbox but optimizing ODE is a cumbersome process with many possible failures due to the matrices that are used to solve the ODE becoming ill-conditioned matrices and this phenomenon introduces discontinuities in the objective function as well as in the nonlinear inequality constraints for some values of the optimization parameters.Hence the number of optimization methods that can solve this type of problem by default Matlab optimization algorithms are narrowed to *fmincon* and *patternsearch*. Also, because of the complexity of the model and the trajectory definition, gradient and the hessian functions of objective function and constraints w.r.t. the optimization parameters are not given. Of course, if the gradient and hessian functions were supplied, *fmincon* could perform much better solution however, in this case, the optimization is done by numerical finite differentiation. To avoid this, derivative-free optimization algorithm *patternsearch* was used. The optimization process diagram is shown in Figure 2.2.

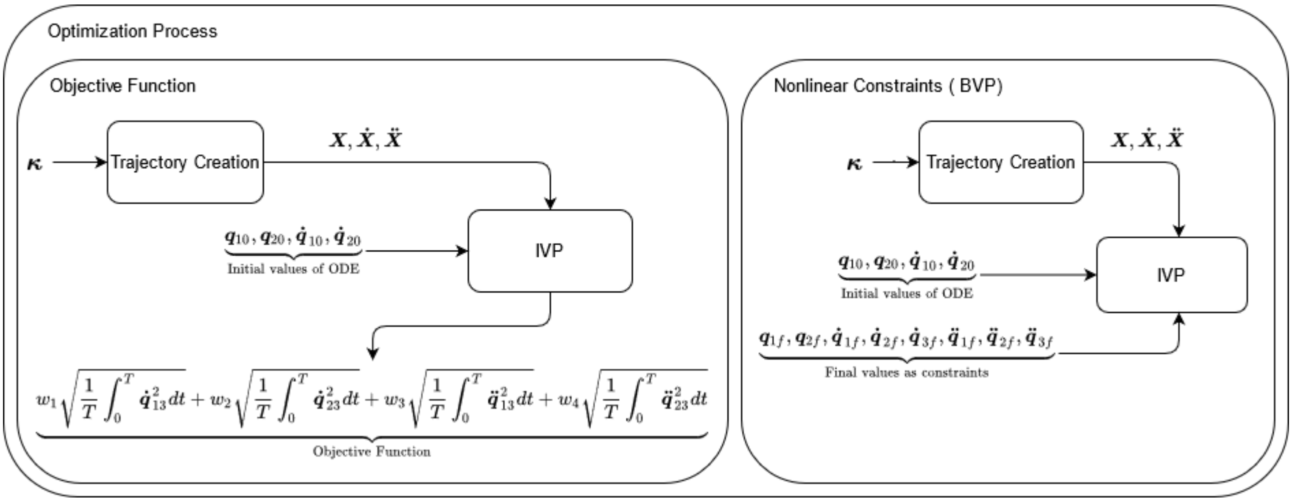

Figure 2.2: Optimization process diagram

where in both objective function and nonlinear constraints, the same $\boldsymbol{\kappa}$ values are used at each iteration.

Optimization

The optimization process is defined for fixed time step, T, and initial starting point of $\boldsymbol{\kappa} \in \mathbb{R}^{r\times 1}$ values are always zero.

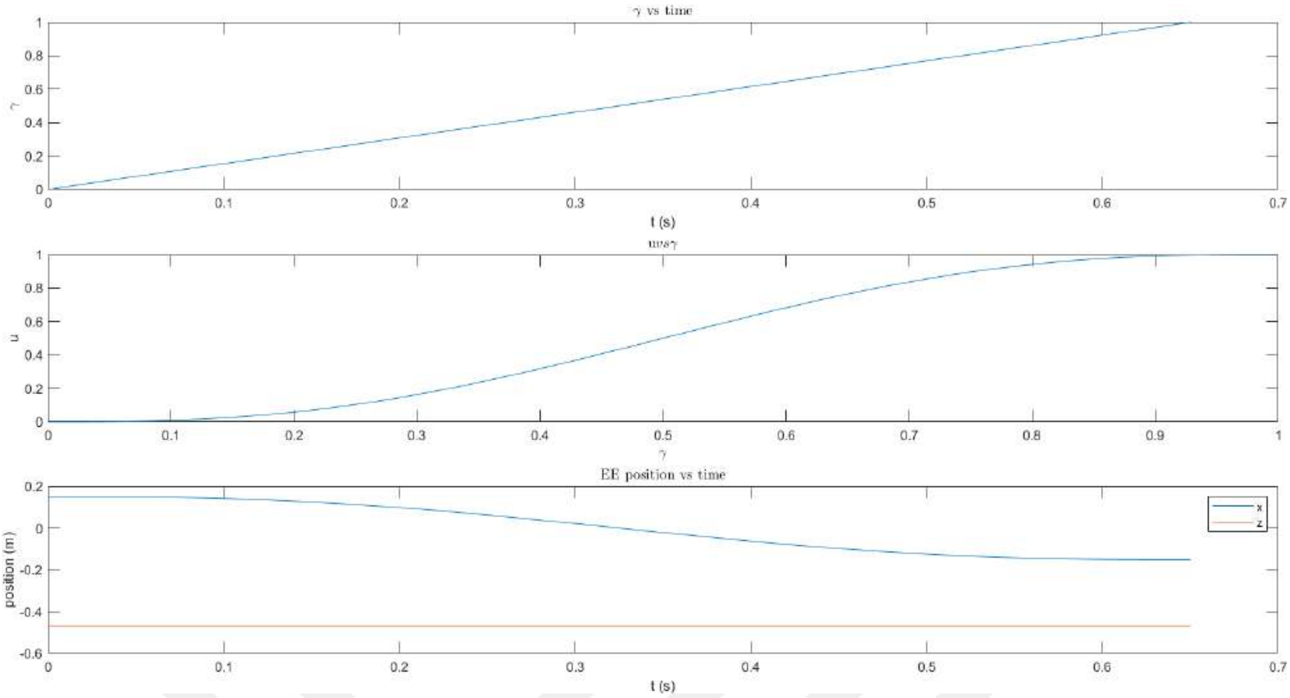

Figure 2.3: γ vs time
u vs γ
EE position vs time

As an example, in Figure 2.3, the trajectory that is used at the zero iteration of the optimization and it is defined between $\mathbf{X} = \begin{bmatrix} x & z \end{bmatrix}^T \begin{bmatrix} 0.15 & -0.4666 \end{bmatrix}^T m$ and $\begin{bmatrix} -0.15 & -0.4666 \end{bmatrix}^T m$ for $T = 0.283$ with the frequency of $2000Hz$.

In Figure 2.4, the obtained trajectory from optimization is shown as:

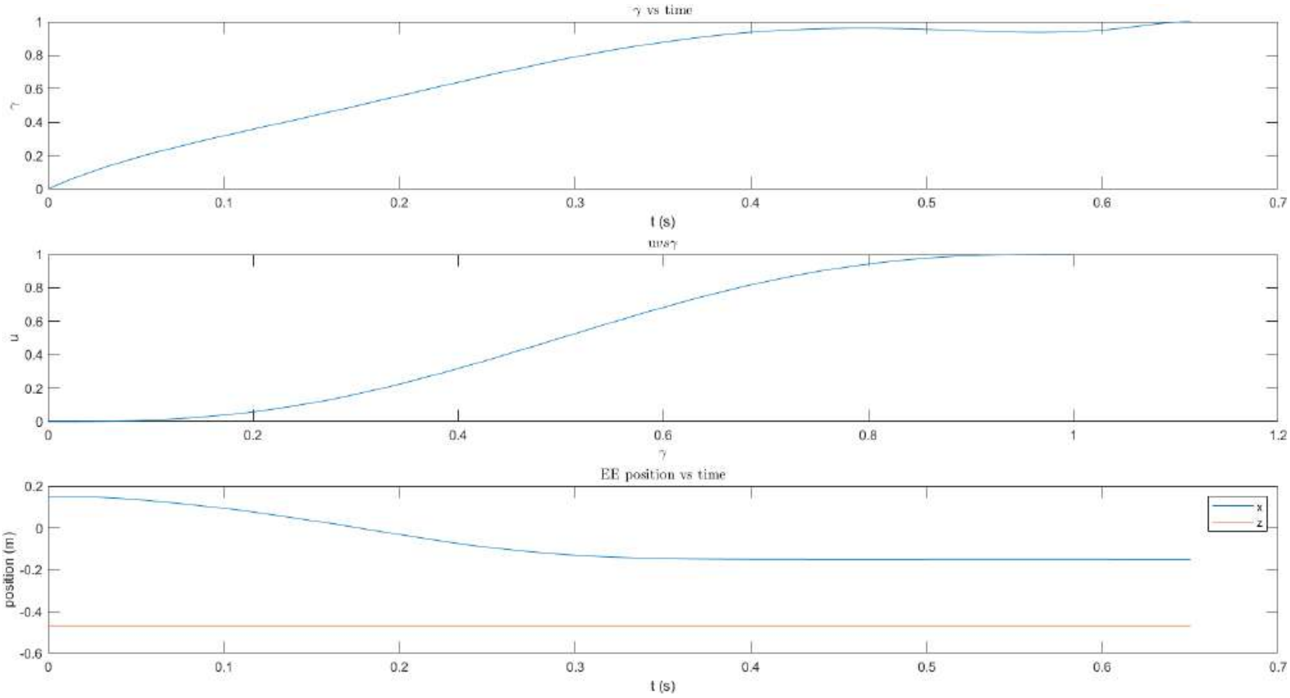

Figure 2.4: γ vs time
u vs γ
EE position vs time

Objective function

The desired behavior of R-min is to go as fast as possible between 2 stationary points with unactuated coordinates to oscillate as low as possible. The residual oscillations are limited by reducing the *root-mean-square* (RMS) of distal unactuated coordinate velocities and accelerations. Thus the objective function is defined as:

$$F = \sum_{i=1}^{2} w_i \sqrt{\frac{1}{T}\int_0^T [\dot{q}_{i3}]^2 dt} + \sum_{i=1}^{2} w_{i+2} \sqrt{\frac{1}{T}\int_0^T [\ddot{q}_{i3}]^2 dt} \tag{2.15}$$

where w_i for i=1,...,4 are the weights of each RMS term. To scale RMSs of velocities and accelerations, weights are chosen based on the importance of RMS of different parameters.

Constraints

The nonlinear constraints are defined to satisfy initial and final positions, velocities and accelerations of the generalized coordinates, to satisfy physical constraints such as max rated motor torques. All mentioned constraints are modeled as inequality constraints. The initial and final position of the EE are satisfied by Equation (2.7). Final velocities and accelerations are satisfied as:

$$at \quad t = T \quad |\dot{q}_{i3}| \leq \dot{q}_{i3_{treshold}} \frac{deg}{s} \quad for \quad i = 1, 2 \tag{2.16}$$

$$at \quad t = T \quad |\ddot{q}_{i3}| \leq \ddot{q}_{i3_{treshold}} \frac{deg}{s^2} \quad for \quad i = 1, 2 \tag{2.17}$$

whereas physical constraints, such as motor maximum rated torque constraints are defined as:

$$max(|\tau_1|) \leq 23.9Nm \tag{2.18}$$

$$max(|\tau_2|) \leq 23.9Nm \tag{2.19}$$

Actuated coordinate velocities and accelerations $\dot{\mathbf{q}}_1$, $\ddot{\mathbf{q}}_1$ are passively satisfied by Equation (2.7) and proximal unactuated coordinate velocities and accelerations $\dot{\mathbf{q}}_2$, $\ddot{\mathbf{q}}_2$ are passively satisfied by their coupled dynamic behavior with both $\mathbf{q}_1$ and $\mathbf{q}_3$.

2.2 Input shaping

Input shaping is a method to eliminate residual oscillations in the system to be controlled. It is based on convolving a sequence of impulses, also called as the input shaper. The duration of shaped input takes Δt time more than the unshaped input. An IS can have as many impulses as possible and the duration can be as long as possible but one should note that the desired input shaper duration should be as short as possible due to the fact that it affects system rise time [14][12][17].

The IS eliminates residual oscillations for elastic systems which R-min can be considered as one. Properties of the IS are listed as [14]:

- If an IS does not generate residual oscillations, then convolution of that IS with any function also does not generate residual oscillations.
- If an IS does not generate residual oscillations, *Laplace* transform of that IS is 0 at the modeling frequency.
- Impulse(s) of the IS that do not generate residual oscillations must be present at suitable time instant(s) with suitable amplitude(s).

These quantities are obtained by satisfying a set of constraints. The amplitude of residual oscillations caused by IS can be found from the ratio of residual oscillation with IS to without IS. For a second-order system with natural frequency ω and damping ratio ζ, the percentage of oscillation ratio, V, is shown below as [14]:

$$V(\omega,\zeta) = e^{-\zeta\omega t_n}\sqrt{C(\omega,\zeta)^2 + S(\omega,\zeta)^2} \tag{2.20}$$

$$C(\omega,\zeta) = \textstyle\sum_{i=1}^{n} A_i e^{\zeta\omega t_i}\cos(\omega\sqrt{1-\zeta^2}t_i) \tag{2.21}$$

$$S(\omega,\zeta) = \textstyle\sum_{i=1}^{n} A_i e^{\zeta\omega t_i}\sin(\omega\sqrt{1-\zeta^2}t_i) \tag{2.22}$$

where A_i, t_i, n are the amplitude, the time instant and number impulses respectively. One should select the time instant of the first impulse of the IS, t_1, to be placed at 0 to minimize the delay.

$$t_1 = 0 \tag{2.23}$$

Also, to have same desired final positions with both unshaped input and shaped input, the sum of all amplitudes must be equaled to 1 [14] as:

$$\sum_{i=1}^{n} A_i = 1 \tag{2.24}$$

To obtain zero residual oscillation with the shortest IS, $V = 0$ condition must be satisfied. Thus, Equations (2.21) and (2.22) also become 0 independently as:

$$\textstyle\sum_{i=1}^{n} A_i e^{\zeta\omega t_i}\cos(\omega\sqrt{1-\zeta^2}t_i) = 0 \tag{2.25}$$

$$\textstyle\sum_{i=1}^{n} A_i e^{\zeta\omega t_i}\sin(\omega\sqrt{1-\zeta^2}t_i) = 0 \tag{2.26}$$

The shortest IS is not considered in the solution of Equations (2.25) and (2.26) as the impulse magnitudes tend to go $\pm\infty$ to decrease the time of IS. To prevent this problem, all impulses, A_i are positive definite [14].

$$A_i \geq 0 \tag{2.27}$$

The desired IS found by satisfying Equations (2.23)-(2.26) subject to Equation (2.27). Thus, four equations require four unknown to solve. For an impulse, there exist two variables, so $n = 2$ impulses are sufficient to define this problem. Thus Equations (2.24), (2.25) and (2.26) become:

$$A_1 + A_2 e^{\zeta\omega t_2}\cos(\omega\sqrt{1-\zeta^2}t_2) = 0 \tag{2.28}$$

$$A_2 e^{\zeta\omega t_2}\sin(\omega\sqrt{1-\zeta^2}t_2) = 0 \tag{2.29}$$

$$A_1 + A_2 = 1 \tag{2.30}$$

Equations (2.28)-(2.31), obtained amplitudes and time instances are provided in [14].

Solution of the problem mentioned above is called as zero-vibration input shaper (ZV IS) because it provides zero residual oscillations when the system model is perfect. Thus, it is highly sensitive to model uncertainties and/or errors [14]. Singhose et al. proposed different ISs for two-mode systems and examined their merits and demerits from simulation results. There are two methods to obtain multimode shapers [14]:

- By convolution of shapers that are calculated separately for each mode.
- By the simultaneous solution of constraint equations for all existing modes.

One should note that modes are basically frequencies in other words. For example, if a system has a behavior of harmonic motion, the system is multi-mode system.

2.2.1 IS methods

There exist many types of convolved ISs [14][15][16][17]:

- ZV : zero-vibration IS, which is obtained by satisfying Equations (2.23)-(2.26).
- ZVD : zero-vibration and zero-derivative IS is obtained exactly with the same methodology as ZV plus derivative of Equation (2.20) is equal to 0 at the modeling frequency.
- ZVDD : zero-vibration and double zero-derivative IS is obtained exactly with the same methodology as ZVD plus one more derivative of Equation (2.20) is equal to 0 at the modeling frequency.
- ZVDDD : zero-vibration and triple zero-derivative IS is obtained exactly with the same methodology as ZVDD plus one more derivative of Equation (2.20) is equal to 0 at the modeling frequency.
- EI : extra-insensitive IS, which proposes limited, small, non-zero residual oscillation magnitude, $V \neq 0$, at the modeling frequency. In the literature, most encountered limiting factor is to allow 5% residual oscillations and obtained by $V = 0.05$ to increase robustness in the neighbor frequencies.

Vaughan et al. investigated robust IS methods for elastic systems by exploiting their structures and pushing their limits [15]. From Figures 2.5 and 2.6, it is clearly seen that as the order of derivative increases, input which is shaped by an IS becomes more insensitive to model errors and thus it increases the robustness. ZV must be used for perfectly known system which introduces least time delays but in reality, nothing is perfect and estimations are true at some level. Thus, more robust IS methods such as ZVD, EI, ZVDD and ZVDDD are introduced for non-perfectly known systems.

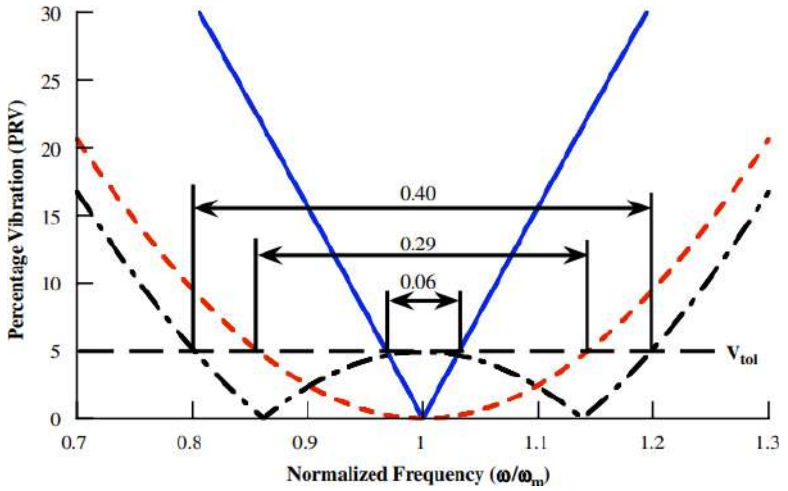

Figure 2.5: Sensitivity curve of single-mode system [15]
− ZV
−− ZVD
− · − EI

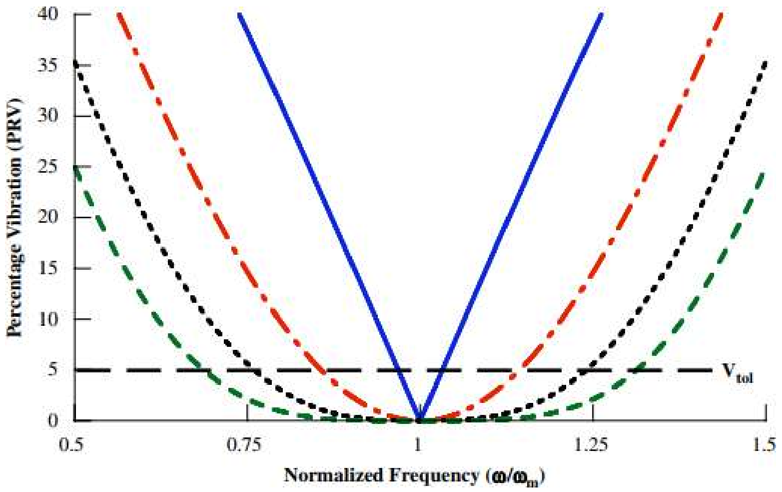

Figure 2.6: Sensitivity curve of single-mode system [15]
− ZV
− · − ZVD
· · · ZVDD
−− ZVDDD

After cumbersome calculations, for all IS methods impulse magnitudes and time of occurrence of these impulses are formulated. In the following sections they are elaborated.

ZVD

ZVD has 3 impulses to shape the input and they are given as:

$$A_1 = \frac{1}{D}, \quad A_2 = \frac{2K}{D}, \quad A_3 = \frac{K^2}{D} \tag{2.31}$$

where

$$K = e^{\frac{-\xi\pi}{\sqrt{1-\xi^2}}}, \quad D = K^2 + 2K + 1 \tag{2.32}$$

with impulse times

$$t_1 = 0, \quad t_2 = \frac{\tau_d}{2}, \quad t_3 = 2\tau_d \tag{2.33}$$

where τ_d is the undamped vibration period and denoted as:

$$\tau_d = \frac{2\pi}{\omega\sqrt{1-\xi^2}} \tag{2.34}$$

EI (option 1)

EI is an example of tolerable vibration IS methods which provides more robustness to model uncertainties than ZVD but it comes with a prescribed oscillation percentage. Unlike ZVD method, $V(\omega, \xi)$ is equaled to small non-zero oscillation percentage. For most applications, this is taken as 5%. EI IS introduces the same amount of time delays with ZVD but it has different impulse magnitudes. Its impulse magnitudes and times are given as [15]:

$$A_1 = \frac{1+V_{tol}}{4}, \quad A_2 = \frac{1-V_{tol}}{2}, \quad A_3 = \frac{1+V_{tol}}{4} \tag{2.35}$$

$$t_1 = 0, \quad t_2 = \frac{\tau_d}{2}, \quad t_3 = 2\tau_d \tag{2.36}$$

where V_{tol} is the tolerated vibration percentage.
For systems with viscous damping, EI IS impulse magnitudes and times are given as:

$$A_1, \quad A_2 = 1 - (A_1 + A_3), \quad A_3 \tag{2.37}$$

$$t_1 = 0, \quad t_2, \quad t_3 = 2\Delta t \tag{2.38}$$

where

$$A_1 = 0.24968 + 0.24962V_{tol} + 0.80008\xi + 1.23328V_{tol}\xi + 0.49599\xi^2 + 3.17316V_{tol}\xi^2 \tag{2.39}$$

$$A_3 = 0.25149 + 0.21474V_{tol} - 0.83249\xi + 1.41498V_{tol}\xi + 0.85181\xi^2 - 4.90094V_{tol}\xi^2 \tag{2.40}$$

and

$$\begin{aligned} t_2 = \; & \frac{1}{\frac{2\pi}{\omega\sqrt{1-\xi^2}}}(0.49990 + 0.46159V_{tol}\xi + 4.26169V_{tol}\xi^2 + 1.75601V_{tol}\xi^3 + 8.57843V_{tol}^2\xi \\ & -108.644V_{tol}^2\xi^2 + 336.989V_{tol}^2\xi^3) \end{aligned} \tag{2.41}$$

EI (option 2)

The EI IS that is used on R-min is this one because in simulation environment, option 1 gave worse result than option 2 in terms of the amount of residual oscillations. It is based on an optimization algorithm which satisfies Equations (2.24) and (2.27) with the same impulse times and the same amount of impulses. The difference between this EI IS method and Vaughan et al.'s EI IS method is that this method provides more robustness but in contrast it introduces more time delays.

Thus, the objective of the optimization problem is to maintain this percentage at the modeling frequency as:

$$F = |V(\omega, \xi) - 0.05| = |V_1(\omega_1, \xi_1) - 0.05| + |V_2(\omega_2, \xi_2) - 0.05| \tag{2.42}$$

where V_1 and V_2 are defined as:

$$V_1 = e^{-\xi_1\omega_1 t_n}\sqrt{C(\omega_1, \xi_1)^2 + 2(\omega_1, \xi_1)^2} \tag{2.43}$$

$$V_2 = e^{-\xi_2\omega_2 t_n}\sqrt{C(\omega_2, \xi_2)^2 + 2(\omega_2, \xi_2)^2} \tag{2.44}$$

$$C_1(\omega_1, \xi_1) = \textstyle\sum_{i=1}^{3} A_{1i}e^{\xi_1\omega_1 t_i}\cos(\omega_1\sqrt{1-\xi_1^2}t_i) \tag{2.45}$$

$$S_1(\omega_1, \xi_1) = \textstyle\sum_{i=1}^{3} A_{1i}e^{\xi_1\omega_1 t_i}\sin(\omega_1\sqrt{1-\xi_1^2}t_i) \tag{2.46}$$

$$C_2(\omega_2, \xi_2) = \textstyle\sum_{i=1}^{3} A_{1i}e^{\xi_2\omega_2 t_i}\cos(\omega_2\sqrt{1-\xi_2^2}t_i) \tag{2.47}$$

$$S_2(\omega_2, \xi_2 1) = \textstyle\sum_{i=1}^{3} A_{1i}e^{\xi_2\omega_2 t_i}\sin(\omega_2\sqrt{1-\xi_2^2}t_i) \tag{2.48}$$

$$\tag{2.49}$$

where F is the objective function. The reason there are two different percentage of oscillation ratios, V_1 and V_2 is because R-min is two-mode system. The optimization parameters are the 3 impulse magnitudes, A_i where (i=1,2,3), which satisfies both $V_1 = 0.05$ and $V_2 = 0.05$. The constraints are given in Equations (2.24) and (2.27). Impulse times are chosen the same with ZVD IS as in Equation (2.33).

ZVDD

ZVDD provides more robustness to model uncertainties than ZVD and EI, it introduces more time delays than ZVD and less than EI. It has one more impulse than ZVD and EI. Its impulse magnitudes and times are given as:

$$A_1 = \tfrac{1}{D}, \quad A_2 = \tfrac{3K}{D}, \quad A_3 = \tfrac{3K^2}{D}, \quad A_4 = \tfrac{K^3}{D} \tag{2.50}$$

$$t_1 = 0, \quad t_2 = \tfrac{\tau_d}{2}, \quad t_3 = \tau_d, \quad t_4 = \tfrac{3\tau_d}{2} \tag{2.51}$$

where K is the same as Equation (2.32) and D is denoted as:

$$D = K^3 + 3K^2 + 3K + 1 \tag{2.52}$$

ZVDDD

ZVDDD provides more robustness to model uncertainties than ZVD, EI and ZVDD but it introduces more time delays than all except EI IS. It has 1 more impulse than ZVDD. It's impulse magnitudes and times are given as:

$$A_1 = \tfrac{1}{D}, \quad A_2 = \tfrac{4K}{D}, \quad A_3 = \tfrac{6K^2}{D}, \quad A_4 = \tfrac{4K^3}{D}, \quad A_5 = \tfrac{K^4}{D} \tag{2.53}$$

$$t_1 = 0, \quad t_2 = \tfrac{\tau_d}{2}, \quad t_3 = \tau_d, \quad t_4 = \tfrac{3\tau_d}{2}, \quad t_5 = 2\tau_d \tag{2.54}$$

where K is the same as Equation (2.32) and D is denoted as:

$$D = K^4 + 4K^3 + 6K^2 + 4K + 1 \tag{2.55}$$

2.2.2 Multi-mode shapers

For multimode systems like R-min, there exist 2 methods in the literature which are *convolved multi-mode shapers* and *simultaneous multi-mode shapers*. These 2 methods are elaborated in the following sections.

Convolved two-mode shapers

Their shaped input durations, robustness against modeling errors which is examined through *sensitivity curve* and residual oscillation behaviors are compared. Sensitivity curve is a plot obtained by the ratio of residual oscillation over frequency. The robustness can be increased by ensuring the slope of sensitivity curve to be zero. ZVD is less sensitive to modeling errors because at the system frequency, ZVD has a larger width than ZV which is shown in Figure 2.7 [14].

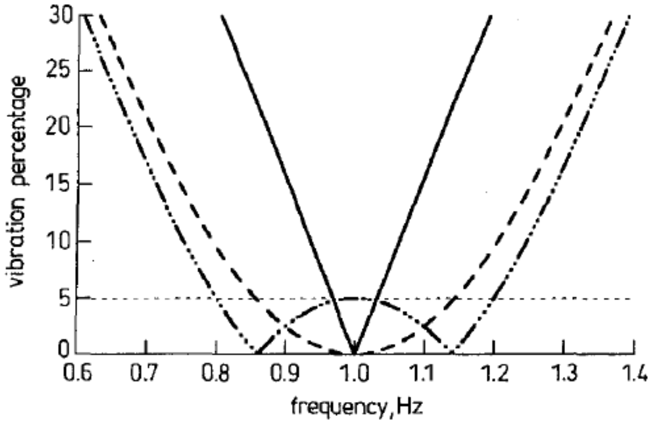

Figure 2.7: Sensitivity curve of single-mode 1Hz system [14]
− ZV
−− ZVD
− · · · − EI

Simultaneous two-mode shapers

Simultaneous solution of ZV-ZV two-mode shaper satisfies Equations (2.25) and (2.26) at system frequencies which are shown in Equations (2.56) and (2.57) whereas ZVD-ZVD shapers satisfies also the derivatives of Equation (2.20) at system frequencies, Equations (2.58) and (2.59) which provide robustness against modeling errors.

$$\sum_{i=1}^{n} A_i e^{\zeta_j \omega_j t_i} \cos(\omega_j \sqrt{1-\zeta_j^2} t_i) = 0, \;\; j = 1, 2 \tag{2.56}$$

$$\sum_{i=1}^{n} A_i e^{\zeta_j \omega_j t_i} \sin(\omega_j \sqrt{1-\zeta_j^2} t_i) = 0, \;\; j = 1, 2 \tag{2.57}$$

$$\sum_{i=1}^{n} A_i t_i e^{\zeta_j \omega_j t_i} \cos(\omega_j \sqrt{1-\zeta_j^2} t_i) = 0, \;\; j = 1, 2 \tag{2.58}$$

$$\sum_{i=1}^{n} A_i t_i e^{\zeta_j \omega_j t_i} \sin(\omega_j \sqrt{1-\zeta_j^2} t_i) = 0, \;\; j = 1, 2 \tag{2.59}$$

For EI-EI two-mode shapers, Equations (2.58) and (2.59) are satisfied but not (2.56) and (2.57) which allow small amount of residual oscillations.

2.2.3 Comparison of convolved and simultaneous shapers

Singhose et al. simulated the application of ZV-ZV, ZVD-ZVD, EI-EI, EI-SI (*specified insensitivity*) two-mode convolved and direct shapers on systems and compared their total time delays and performances [14].

The main disadvantage of direct method is that it is not easy to obtain the shaper as it is for convolved method which convolves single-mode shapers.

For both shaper methods, they must be obtained by an optimization method.

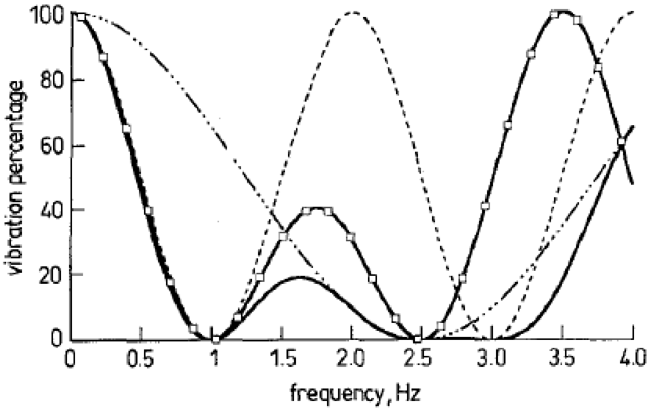

Figure 2.8: Sensitivity curve of two-mode ZVD-ZVD ISs for $1Hz$ and $2.5Hz$ systems [14]
— convolved
–□– direct
– · · · – $2.5Hz$
–– $1Hz$

One should note that elimination of residual oscillations at $3Hz$ with convolved shaper is obtained due to the fact that it treats as convolution of single-mode shapers. For single-mode shapers odd frequency multipliers are eliminated, thanks to $1Hz$ frequency.

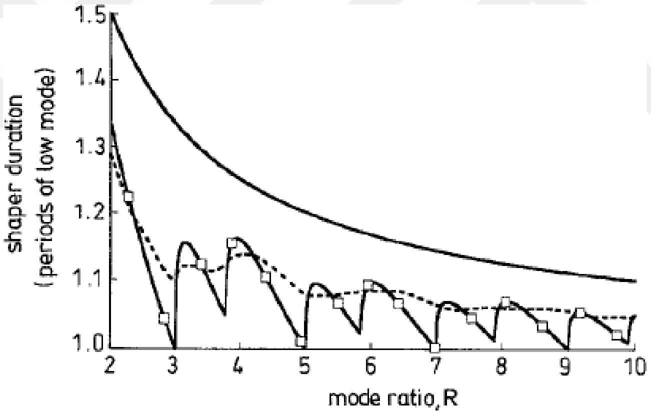

Figure 2.9: Shaper durations of two-mode systems over frequency ratio, R [14]
— convolved ZVD-ZVD
–□– Direct ZVD-ZVD
–– direct EI-SI

where SI constraints are implemented around a high frequency to make shaper insensitive to residual oscillations of which their percentages are kept under a value, V. SI constraints assure acceptable level of robustness against high frequency modelling errors. Direct shapers perform with less time delays than their convolved ones because they use less number of impulses which can be seen in Figure 2.9. Also, direct ZVD-ZVD has time delay advantage over direct EI-SI. For robustness against errors, in the low system frequency, performances of direct and convolved methods are nearly identical whereas convolved method is more robust to modeling errors for higher system frequency which can be seen in Figure 2.8. One should decide which merit is more important for considered system [14].

For convolved shapers, the total time delay is equal to sum of individual time delays introduced for each mode as:

$$t_n = T_{w_1} + T_{w_2} \tag{2.60}$$

whereas direct shapers do not satisfy Equations (2.60) and total time delay is always less than the sum of individual time delays of each shaper.

$$t_n < T_{w_1} + T_{w_2} \tag{2.61}$$

2.2.4 IS to eliminate residual oscillations for UA system

Ida et al. extended the RTR trajectory generation to robust generic trajectory generation with the help of methods *dynamic scaling* (DS), and IS which proposed in [14] for aforementioned UA CDPR. The main drawback of [10], the robustness against model uncertainties was not examined for the proposed method but in [11], the proposed method has proven it's merits against model uncertainties for both simulation and experimental studies. The trajectory defined between 2 set points is given as [11]:

$$\mathbf{q}_a(t) = \mathbf{q}_{a,s} + (\mathbf{q}_{a,f} - \mathbf{q}_{a,s})u(t) \tag{2.62}$$

The desired behavior of the robot to move between 2 stationary points with non-residual oscillations, $u(t)$ must be designed considering this. Thus, *multi-mode zero-vibration input shaper* (MMZVIS) is introduced to shape $\mathbf{q}_a(t)$ trajectories. Equation (2.62) becomes:

$$\mathbf{q}_a(t) * S(t) = \mathbf{q}_{a,s} + (\mathbf{q}_{a,f} - \mathbf{q}_{a,s})(u(t) * S(t)),\ \ S(t) = \sum_{i=1}^{n} A_i \delta_i (t - t_i) \tag{2.63}$$

where $\delta(t = t_i) = 1$, $\delta(t \neq t_i) = 0$ is an impulse function, A_i is the impulse magnitude and n is the number of impulses. $A_{\%}(f)$, the magnitude of the Fourier transform of $S(t)$ at the frequency f is shown as:

$$A_{\%}(f) = \sqrt{\Big(\sum_{i=1}^{n} A_i \cos(2\pi f t_i)\Big) + \Big(\sum_{i=1}^{n} A_i \sin(2\pi f t_i)\Big)} = 0 \ \Rightarrow (A_i, t_i) \tag{2.64}$$

where IS supposes to eliminate residual oscillations at frequency f. Because of the process of IS is cumbersome and introduces additional time delay to the system, Δt, Ida et al. proposed DS to be used on the reference trajectory. The trajectory parameters can be obtained by setting $U(f) = 0$ or Ü= $(-2\pi f)^2 U(f) = 0$ for desired frequency. This method allows to determine the total time of robust trajectory, $T + \Delta t$. One should note that, with DS, optimal time T_{opt_d} is bounded by the lowest frequency. Also, in comparison to convolved method total time, robust DS trajectory total time is less and bounded as $T_{opt_d} + \Delta t_d \leq T_{opt_{conv}} + \Delta t_{conv}$. 4 trajectories are applied with DS only, IS version of DS and trapezoidal IS motion laws (IS-T) with different Ts [11].

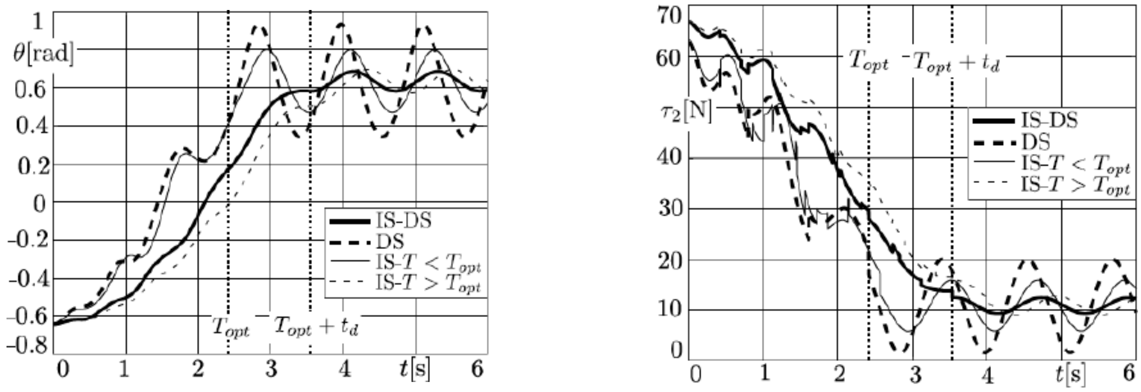

(a) θ (b) τ_2

Figure 2.10: Critical oscillations on θ and τ_2 [11]

As it can be seen from Figure 2.10, IS is more resilient to residual oscillations. Also, for larger T values, IS provides less residual oscillations but for fast motions, T should be small, thus IS may not be a suitable option whereas DS allows to determine the best case of T. However, DS was not investigated in this master thesis.

2.2.5 IS on R-min

To be tested, four IS methods are chosen. These are ZVD, EI, ZVDD, ZVDDD ISs. Since R-min is a two-mode system, a MM IS method must be selected. For the sake of simplicity of calculations, convolved two-mode IS method is chosen. Implementation of single mode 3 impulse input shaping (ZVD) is shown in Figure 2.11.

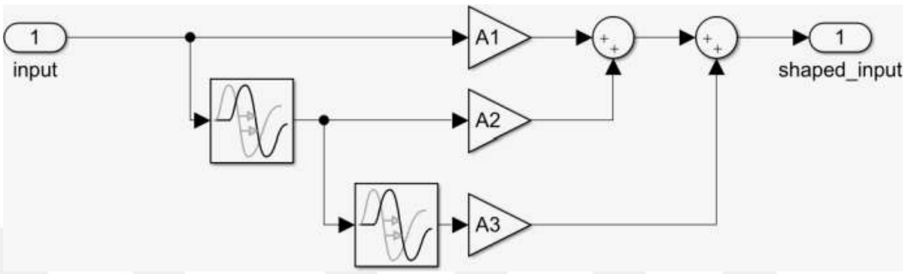

Figure 2.11: IS representation with 3 impulses in *Matlab* [12]

To achieve MM IS, output which is shaped for lower ω becomes the input of higher ω to be shaped hence convolved MM IS obtained.

2.2.6 Dynamic characteristics of R-min

Identification of dynamic characteristics of R-min is important due to shape the input trajectory at the modeling frequency.

As an example multi-DoF undamped system's equation of motion is represented as [22]:

$$\mathbf{M}\frac{d^2\mathbf{x}}{dt^2} + \mathbf{K}\mathbf{x} = \mathbf{0} \tag{2.65}$$

where $\mathbf{K}$, $\mathbf{x}$ are the stiffness matrix of the system and displacement respectively. To find harmonic solution of $\mathbf{x}$, the solution is assumed to be $\mathbf{X}\sin(\omega t)$. By substituting this expression into (2.66), following equation of motion is obtained as:

$$-\mathbf{M}\mathbf{X}\omega^2\sin(\omega t) + \mathbf{K}\mathbf{X}\sin(\omega t) = \mathbf{0} \quad \Rightarrow \quad \mathbf{K}\mathbf{X} = \omega^2\mathbf{M}\mathbf{X} \tag{2.66}$$

The form of Equation (2.66) can be represented as:

$$\mathbf{K}\mathbf{u} = \lambda\mathbf{M}\mathbf{u} \tag{2.67}$$

Equation (2.67) is denoted as *generalized eigenvectors* and *generalized eigenvalues.* To obtain natural frequency, following calculation is made as:

$$\omega_i = \sqrt{\lambda_i} \tag{2.68}$$

Both left and right arm of R-min have their own natural frequencies. These frequencies are obtained as:

$$\boldsymbol{\omega} = \begin{bmatrix} \omega_1 \\ \omega_2 \end{bmatrix} = \sqrt{eig(\mathbf{M}_{22}^{-1}\mathbf{K})} \tag{2.69}$$

Natural frequencies come from the part of $\overrightarrow{O_{i2}O_{i3}} - \overrightarrow{O_{i3}P}$ where (i=1,2). That's why $\mathbf{M}_{22}$ is taken for the calculations of natural frequency.

For rigid systems, natural frequency is constant throughout motion. For elastic systems, natural frequency can vary throughout motion. Also, change in the natural frequency is affected by the speed of the followed trajectory. Considering these, for every RTR trajectory generation, natural frequencies of the system must be analysed and modeling frequency must be chosen accordingly.

Natural frequency is computed throughout the trajectory between $\begin{bmatrix} x & z \end{bmatrix} = \begin{bmatrix} 0.15 & -0.4666 \end{bmatrix} m$ to $\begin{bmatrix} x & z \end{bmatrix} = \begin{bmatrix} -0.15 & -0.4666 \end{bmatrix} m$ EE positions within $0.283 sec$. After comparing the effects of different modeling frequencies and modeling damping ratios, modeling frequencies are selected according to the significant part of the motion which is the middle part. Hence, the modeling frequencies are selected as $\boldsymbol{\omega} = \begin{bmatrix} 5.95 & 6.5 \end{bmatrix} Hz$ and the modeling damping ratios are selected $\boldsymbol{\xi} = \begin{bmatrix} 0.7 & 0.7 \end{bmatrix}$. Also, it is clearly seen from the Figure 2.12 that for chosen modeling frequencies, including ZVD which is the least effective IS method among all IS methods used on R-min will provide robustness against ±5% of the normalized frequencies which is acceptable for R-min since the modeling errors are not considered more than 5%. Clearly, ZVDDD is expected to be the most effective IS method against model uncertainties and residual oscillations.

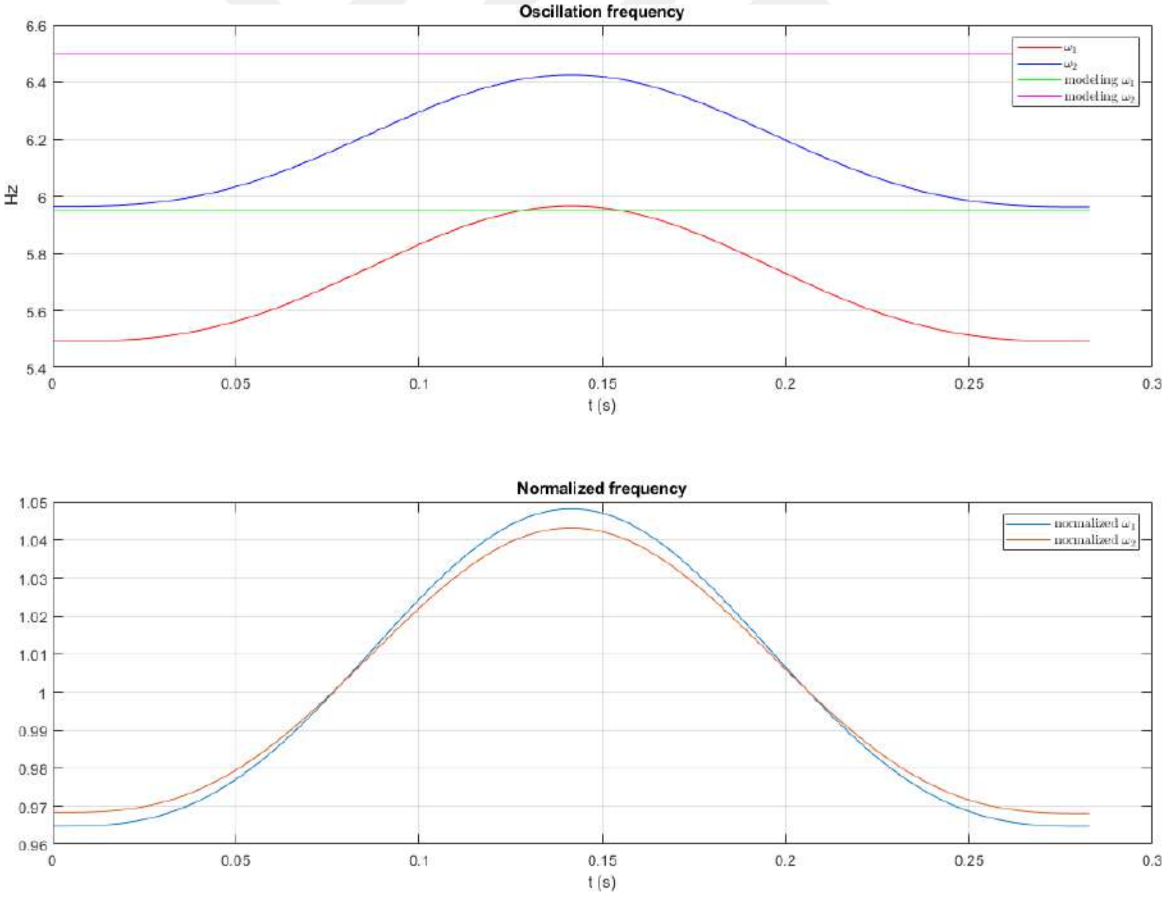

Figure 2.12: Natural frequencies vs time with chosen modeling frequencies (up) Normalized frequency vs time (down)

2.2.7 Impulse magnitudes and times of ISs

Computed MM IS impulse magnitudes and times are given as:

	ZVD	EI	ZVDD	ZVDDD
$A_{11} = A_{12}$	0.914	0.8778	0.87381	0.83539
$A_{21} = A_{22}$	0.084	0.07081	0.12055	0.15367
$A_{31} = A_{32}$	0.001933	0.0514	0.005544	0.0106
$A_{41} = A_{42}$	–	–	$8.49E^{-5}$	$3.25E^{-4}$
$A_{51} = A_{52}$	–	–	–	$3.7366E^{-6}$
t_{11} (s)	0	0	0	0
t_{12} (s)	0	0	0	0
t_{21} (s)	0.11767	0.11767	0.11767	0.11767
t_{22} (s)	0.10771	0.10771	0.10771	0.10771
t_{31} (s)	0.23534	0.23534	0.23534	0.23534
t_{32} (s)	0.21543	0.21543	0.21543	0.21543
t_{41} (s)	–	–	0.35301	0.35301
t_{42} (s)	–	–	0.32314	0.32314
t_{51} (s)	–	–	–	0.47068
t_{52} (s)	–	–	–	0.43085

Table 2.1: Multi-mode IS impulse magnitudes and times

2.2.8 IS on systems with time and state dependent dynamics

All IS methods are used on R-min are designed for time and state independent dynamics which means system ω and ξ are constant. However, for elastic systems, ω and ξ are functions of position e.g. joint angles and other various parameters. Magee et al. extended IS method applied to systems with time and state independent dynamics to systems with time and state dependent dynamics. Thus, a change in ω and ξ changes impulse magnitudes and times and this phenomenon introduces undesired residual oscillations by the shaper itself [18].

To visualize this phenomenon, trajectories in EE level were created with different methods which is shown as in Figure 2.13. These trajectories are just extension of the trajectories shown in Figure 2.16 by adding rest time at the end of their motion.

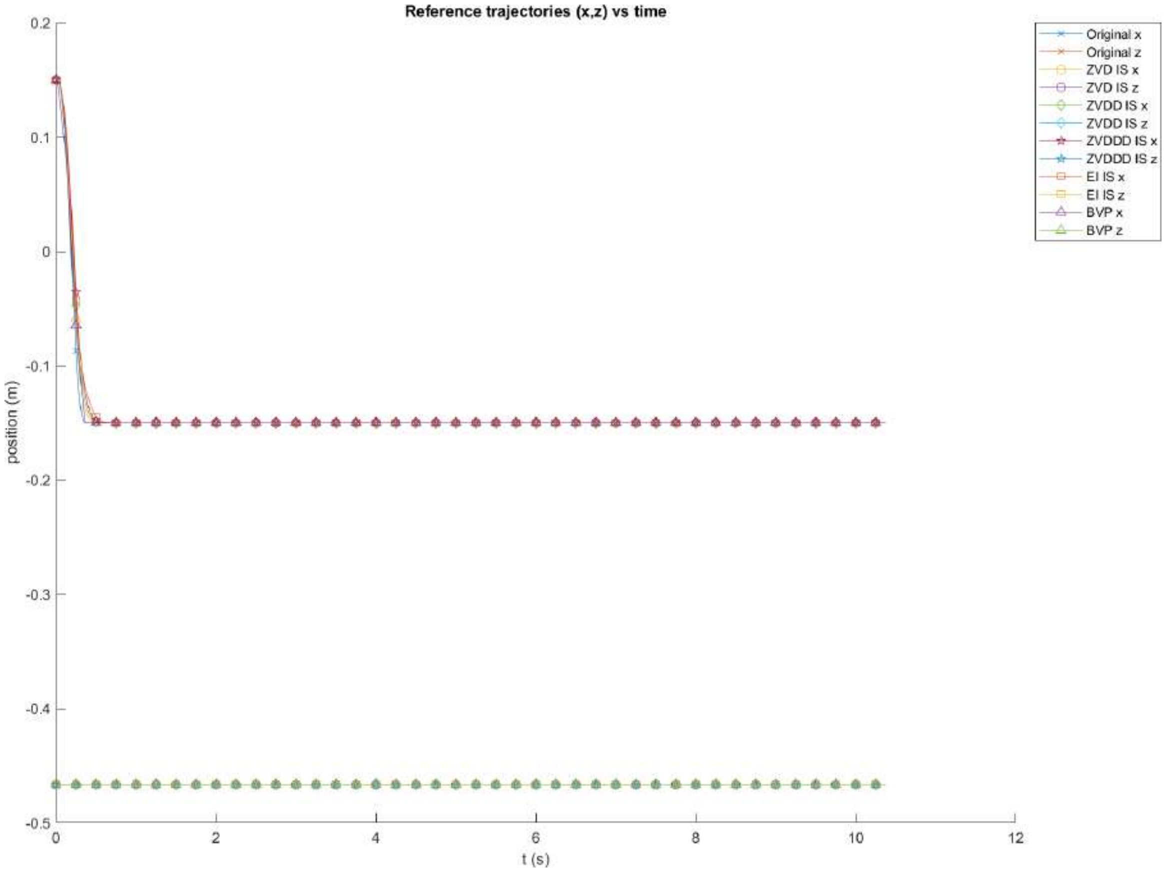

Figure 2.13: Reference EE trajectories

and passing from EE level to joint level is done by IDM which is detailed in Section 1.7 and shown in Figure 2.14.

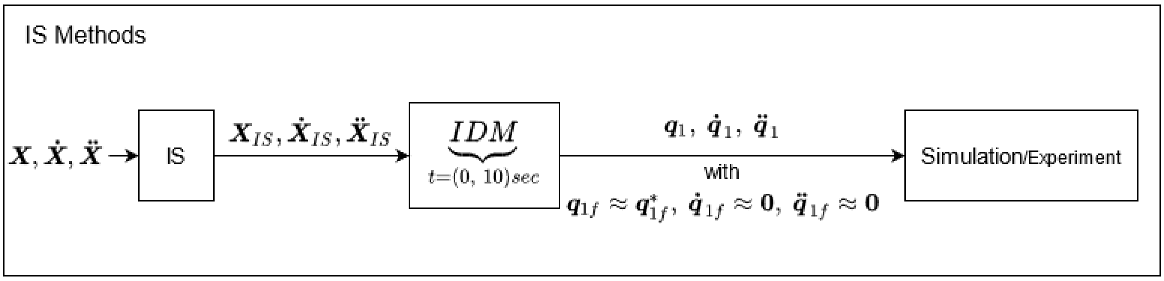

Figure 2.14: Passing from reference EE trajectories to joint level trajectories

These actuated coordinates are, then, given to R-min to be tracked. However, because of the undesired residual oscillations introduced by ISs, actuated coordinate positions do not converge desired positions which is shown in Figure 2.15 and velocities and accelerations are not null. Also, It is clearly seen from Figure 2.15 that the residual oscillations are introduced after the motion is completed and from lowest to highest, oscillation magnitudes are listed as ZVDDD, ZVDD, EI and ZVD respectively.

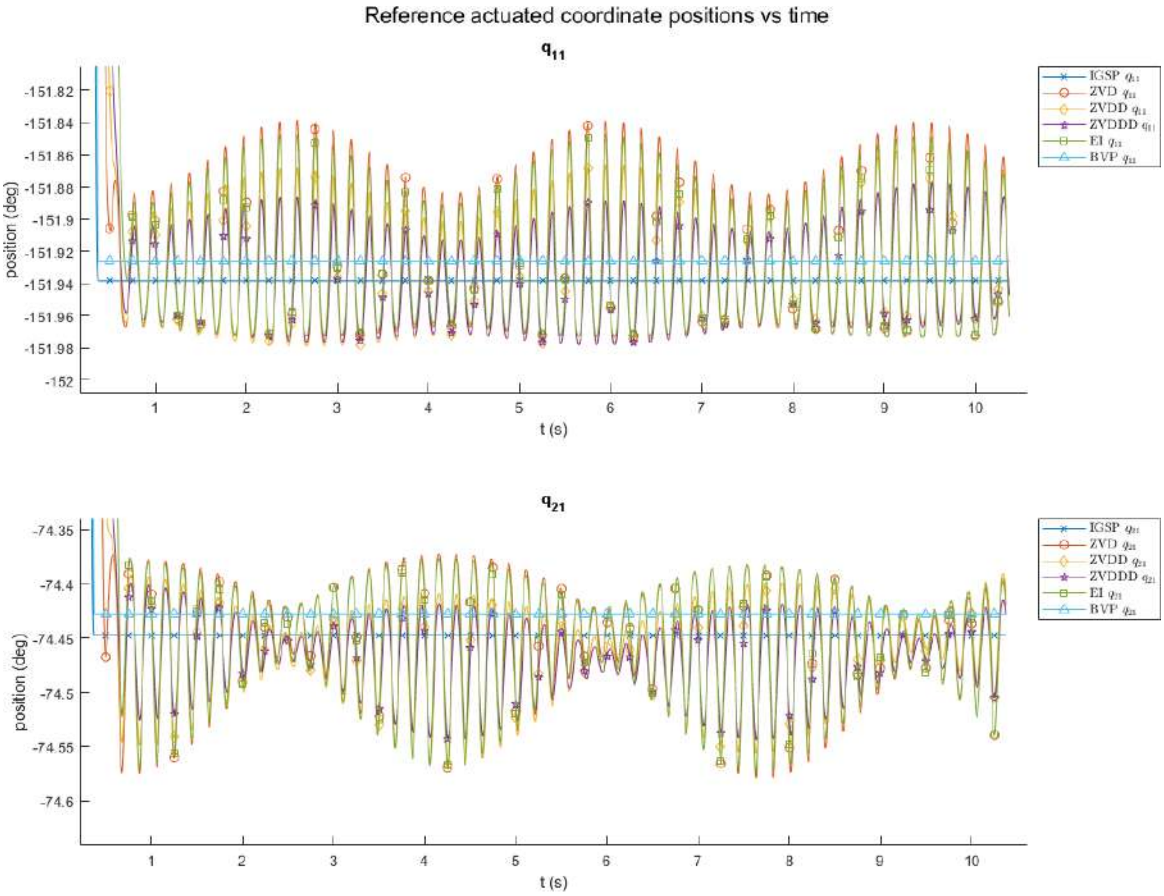

Figure 2.15: Oscillations caused by ISs in actuated joint coordinates

To eliminate this problem, trajectories were created from $t = 0$ to $t \approx 0.72$ as:

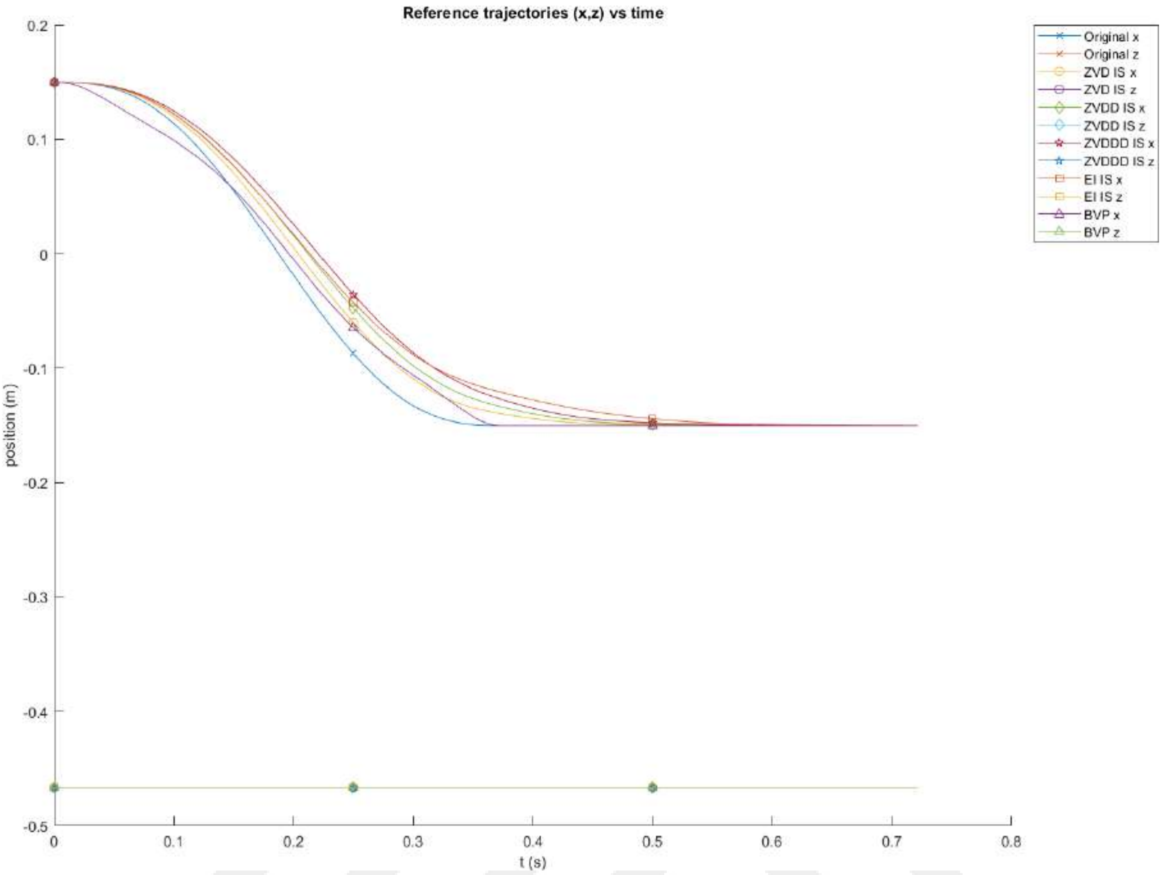

Figure 2.16: Reference EE trajectories

The same procedure is followed as in Figure 2.14 but to make actuated coordinates reach to desired positions with zero velocities and accelerations, a simple spline trajectory is imposed after shaped trajectories are finished which is shown in Figure 2.17.

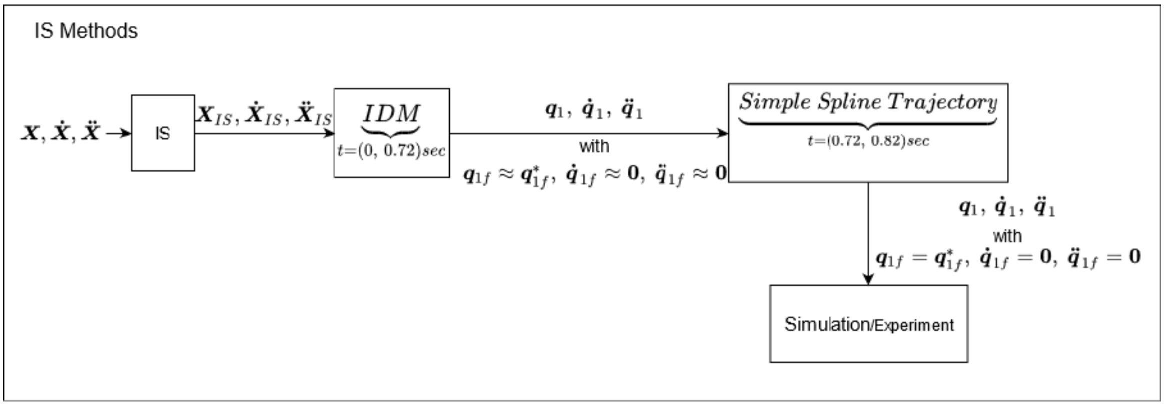

Figure 2.17: Passing from reference EE trajectories to joint level trajectories

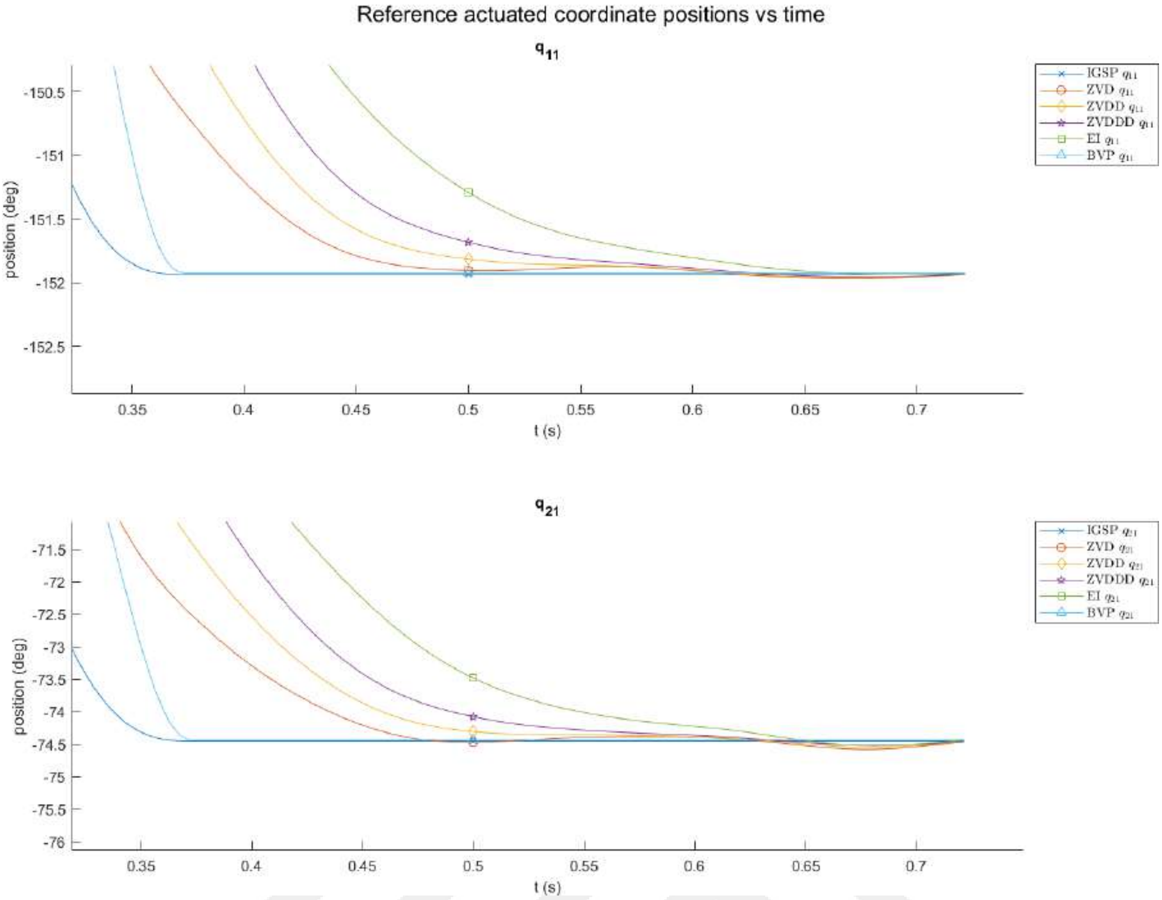

Figure 2.18: Actuated joint coordinates

Thomsen et al. implemented *time-varying input shaping* (TVIS) on UR robots. Despite the efficiency of IS on systems with time and state independent dynamics is proven, it does not provide enough robustness on systems with time and state dependent [13]. As an example, ZV IS for for systems with time and state independent dynamics is given as:

$$A_1 = \tfrac{1}{D}, \quad A_2 = \tfrac{K}{D} \tag{2.70}$$

$$t_1 = 0, \quad t_2 = \tfrac{\tau_d}{2} \tag{2.71}$$

where τ_d is defined in Equation (2.34) and

$$K = e^{\frac{-\xi\pi}{\sqrt{1-\xi^2}}}, \quad D = K + 1 \tag{2.72}$$

and ZV IS for systems with time and state dependent dynamics is given as:

$$A_1\Big(\xi(t)\Big) = \frac{1}{D\Big(\xi(t)\Big)}, \quad A_2\Big(\xi(t)\Big) = \frac{K\Big(\xi(t)\Big)}{D\Big(\xi(t)\Big)} \tag{2.73}$$

$$t_1 = 0, \quad t_2\Big(\omega(t), \xi(t)\Big) = \frac{\tau_d\Big(\omega(t), \xi(t)\Big)}{2} \tag{2.74}$$

To sum up, if the model of the system is perfectly known or close to perfectly known, RTR trajectory planning method is the best method because the time of the motion is predefined by the user whereas for ISs, introduced time delays are inevitable and not predetermined. Also RTR gives the least oscillatory motion for the unactuated coordinates in comparison to ISs. In contrast, ISs are straightforward methods of filtering and easier to implement in comparison to RTR and also ISs provide robustness against model uncertainties.

Chapter 3

Results and discussion

Simulation and experimental results are shown in this chapter to compare the effect of the original spline trajectory, shaped trajectories of the original trajectory with different ISs and the RTR trajectory are compared for different time of motions. All the trajectories are created between $\mathbf{X}_0 = \begin{bmatrix}0.15 & -0.4666\end{bmatrix} m$ and $\mathbf{X}_f = \begin{bmatrix}-0.15 & -0.4666\end{bmatrix} m$. As an example, RTR of trial 2 is followed in Adams environment and shown in Figure 3.1 as:

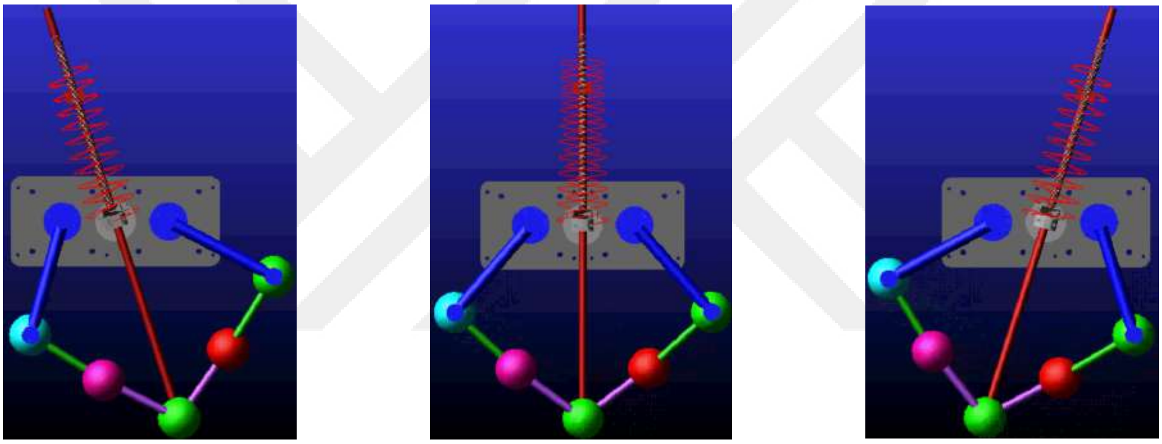

(a) t=0s (b) t=0.175s (c) t=0.335s

Figure 3.1: RTR (Trial 2) in *Adams* simulation environment

The colorful ball shaped objects at the joints are mass points but they are just representative in this case. Then, the same trajectory is tested on R-min and shown in Figure 3.2 as:

(a) t=0s (b) t=0.175s (c) t=0.335s

Figure 3.2: RTR (Trial 2) on R-min

The original trajectory which is created by splines and then by giving it to IGSP to obtain the trajectory in joint level. Shaped trajectories and RTR trajectory are given to IDM to obtain trajectories in joint level. The simulations are made in the *Adams* environment connected to *Simulink* environment. The PID CTC controls R-min model which is found in *Adams* from *Simulink.* The trajectories which were created in *Matlab* are given to the controller as reference signals. Both in *Adams* and *IDM* in *Matlab*, friction models were implemented.

3.1 Simulation results

3.1.1 Trial 1

At the time of trial 1, RTR did not obtain a good trajectory so original trajectory and the shaped trajectories of this original trajectory were tested.

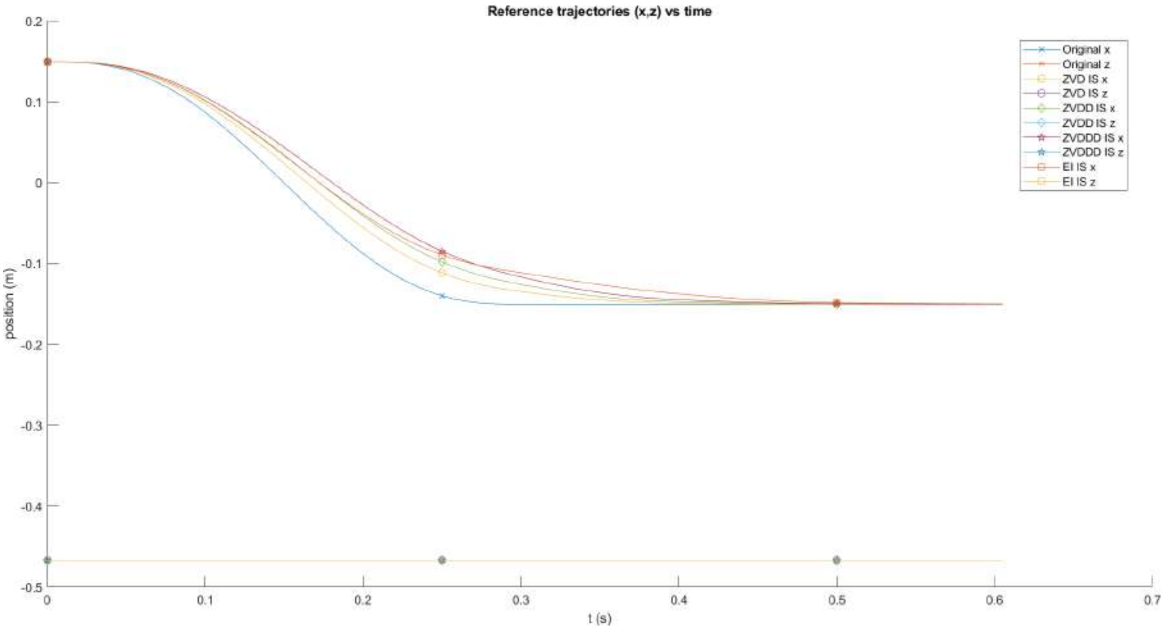

Figure 3.3: Reference EE trajectory

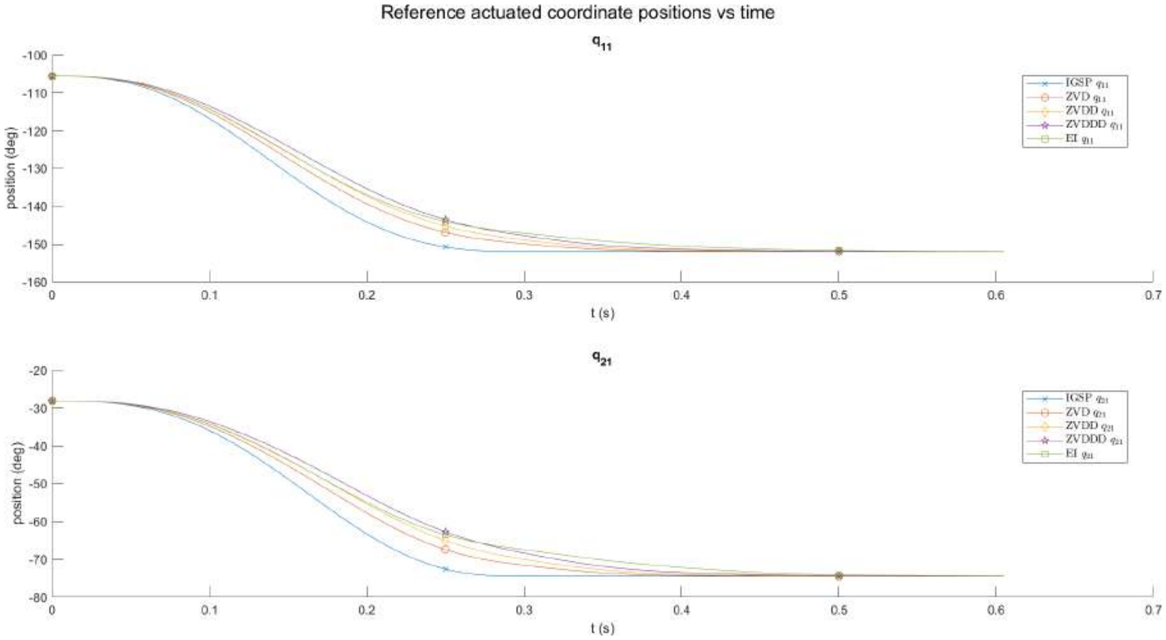

Figure 3.4: Reference actuated coordinate trajectory

	IGSP	ZVD	EI	ZVDD	ZVDDD	RTR
5% t_{ss} EE position (s)	0.2486	0.3368	0.4402	0.3627	0.3895	NaN
% of Introduced time delay (s)	0	35.4453	77.0292	45.8855	56.6419	NaN
Max $\lvert\boldsymbol{\tau}\rvert$ (Nm)	17.5206	16.1404	15.6985	15.6508	15.1966	NaN
SS $\lvert\mathbf{p}_e\rvert$ (m)	$5.6282E^{-5}$	$2E^{-4}$	$1.5E^{-4}$	$4.7772E^{-5}$	$4.8122E^{-5}$	NaN
q_{13} Overshoot (deg)	15.6338	11.8992	10.971	10.3791	9.08559	NaN
q_{23} Overshoot (deg)	3.3171	0.08334	-0.18225	-0.89466	-1.5993	NaN
q_{13} Undershoot (deg)	-4.83	-0.41142	-0.09208	-0.056471	0.29346	NaN
q_{23} Undershoot (deg)	-13.0296	-10.5409	-9.58843	-9.49135	-8.58825	NaN
RMS of q_{13} (deg)	96.6486	80.952	75.8619	70.4171	66.5793	NaN
RMS of q_{23} (deg)	88.0666	80.0325	73.1361	74.5859	71.4077	NaN

Table 3.1: Comparison of trajectory planning methods

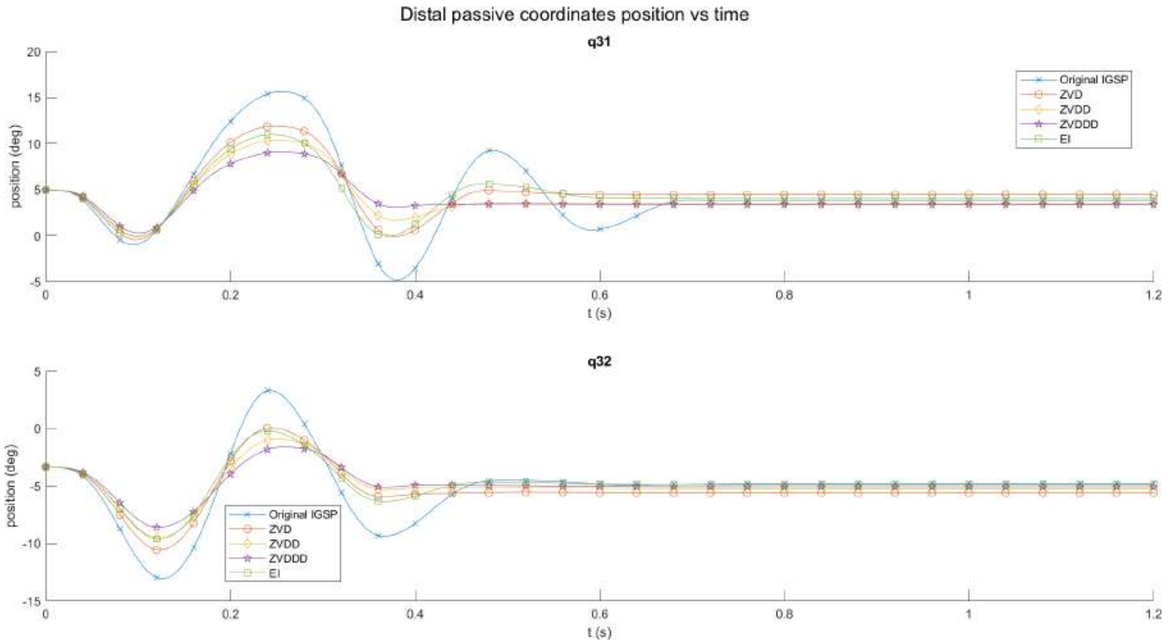

Figure 3.5: Distal unactuated coordinate oscillations

Residual oscillations of distal unactuated coordinates are listed ZVDDD, ZVDD, EI, ZVD and IGSP from best to worst respectively. 5% t_{ss} EE trajectory tracking, EE trajectory tracking error, 5% t_{ss} EE trajectory tracking error and applied torques are given in Section A.1.1.

3.1.2 Trial 2

In this trial, RTR is included to comparison and the motion time of the original trajectory is slightly lower.

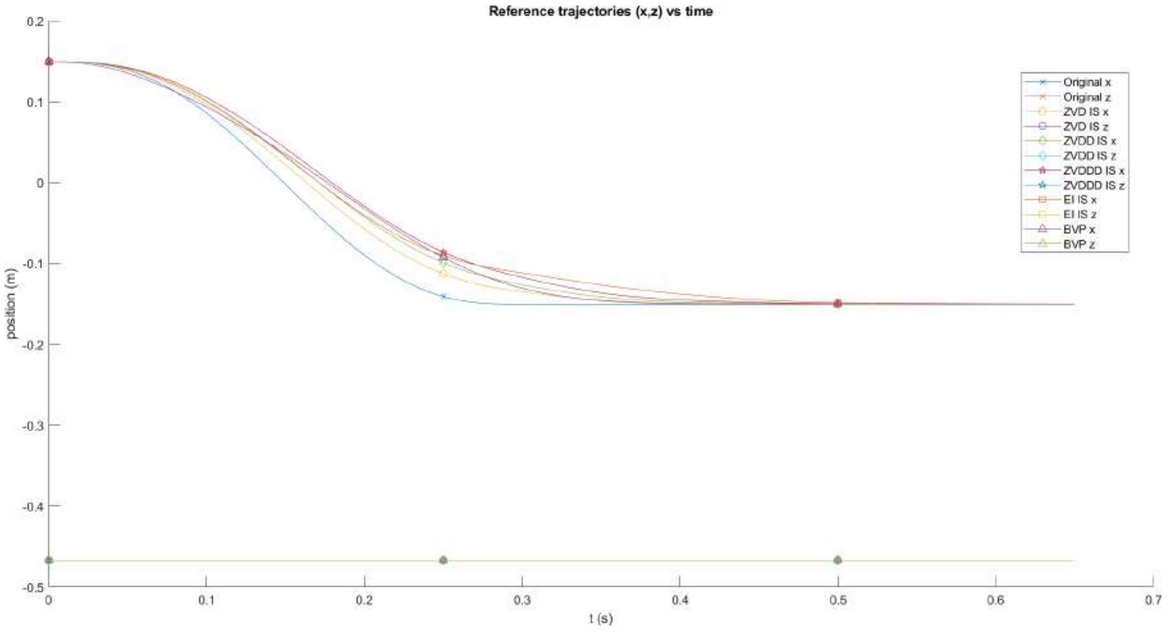

Figure 3.6: Reference EE trajectory

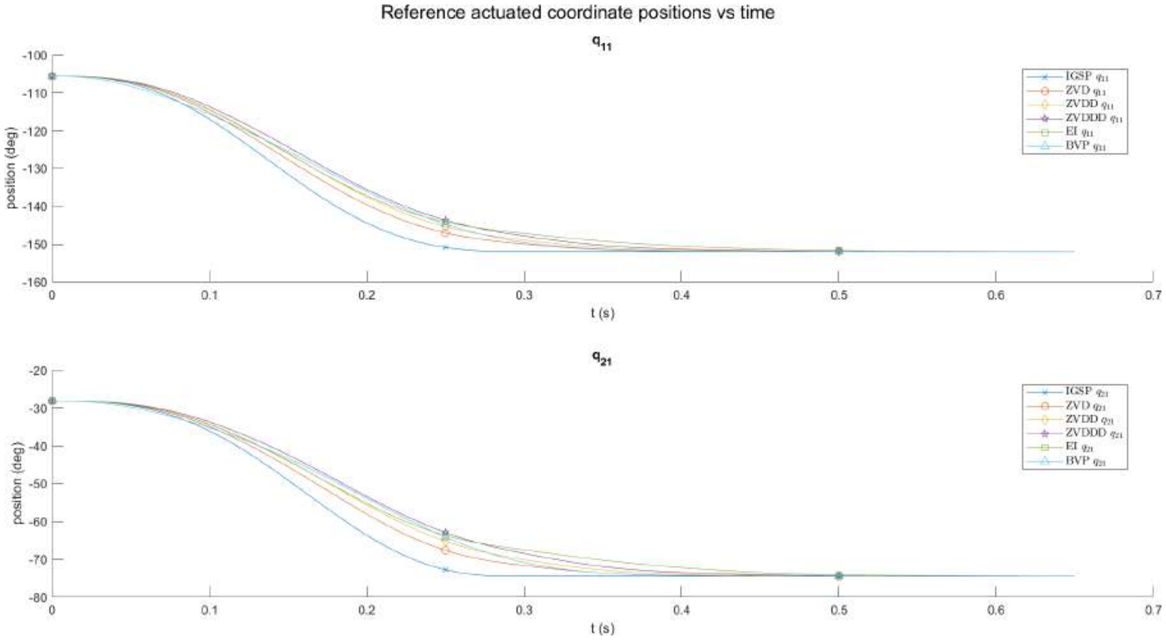

Figure 3.7: Reference actuated coordinate trajectory

	IGSP	ZVD	EI	ZVDD	ZVDDD	RTR
5% t_{ss} EE position (s)	0.24699	0.33483	0.44093	0.36137	0.38882	0.33544
% of Introduced time delay (s)	0	35.5635	78.5211	46.3081	57.4209	35.8111
Max $\lvert\boldsymbol{\tau}\rvert$ (Nm)	17.6211	16.2115	15.7652	15.717	15.2587	15.9045
SS $\lvert\mathbf{p}_e\rvert$ (m)	$8.48E^{-5}$	$2.73E^{-4}$	$1.499E^{-4}$	$2.807E^{-5}$	$2.683E^{-7}$	$1.766E^{-4}$
q_{13} Overshoot (deg)	15.9408	12.1124	11.1755	10.5498	9.21666	6.98714
q_{23} Overshoot (deg)	3.5563	0.23802	-0.042683	-0.7791	-1.5176	-1.9632
q_{13} Undershoot (deg)	-5.1377	-0.4795	-0.25789	-0.11177	0.24101	0.27414
q_{23} Undershoot (deg)	-13.2196	-10.6938	-9.72005	-9.6211	-8.69875	-7.74113
RMS of q_{13} (deg)	333.8367	268.96	252.533	237.4655	221.3829	214.9655
RMS of q_{23} (deg)	293.2537	255.5201	234.3958	236.8179	225.8291	220.3778

Table 3.2: Comparison of trajectory planning methods

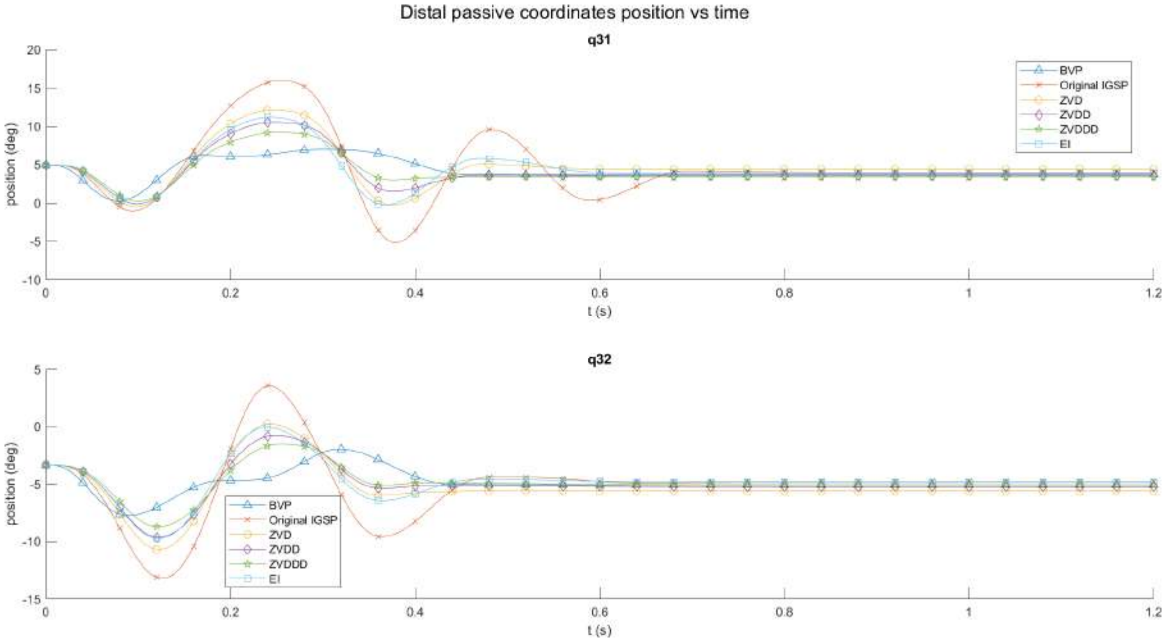

Figure 3.8: Distal unactuated coordinate oscillations

The RTR has the same t_{ss} with the worst IS which is ZVD however the residual oscillations of distal unactuated coordinates noticeably smaller than the best IS which is ZVDDD IS. Also, in the interval of $\begin{bmatrix}0.43 & 1.2\end{bmatrix}$s, distal unactuated coordinates with RTR converges to it's final position whereas for IGSP, it is still in action. This behavior of IGSP can be seen for both q_{13} and q_{23} in comparison to other methods. This can cause a problem in case IGSP is used as a fast P&P trajectory because even if the motion with IGSP is finished at 0.247s, distal unactuated coordinates stop moving at nearly 0.7s. If R-min forced to move back to the original position after 0.25s, the oscillation frequency of the distal unactuated coordinates will increase due to the potential energy stored by the first motion. This is definitely an unwanted behavior for repeated tasks such as P&P operations. At the end, residual oscillations of distal unactuated coordinates are listed RTR, ZVDDD, ZVDD, EI, ZVD and IGSP from best to worst respectively. 5% t_{ss} EE trajectory tracking, EE trajectory tracking error, 5% t_{ss} EE trajectory tracking error and applied torques are given in Section A.1.2.

3.1.3 Trial 3

In this trial, to compare fairly IGSP and RTR trajectory planning methods, their t_{ss} are set to be equal.

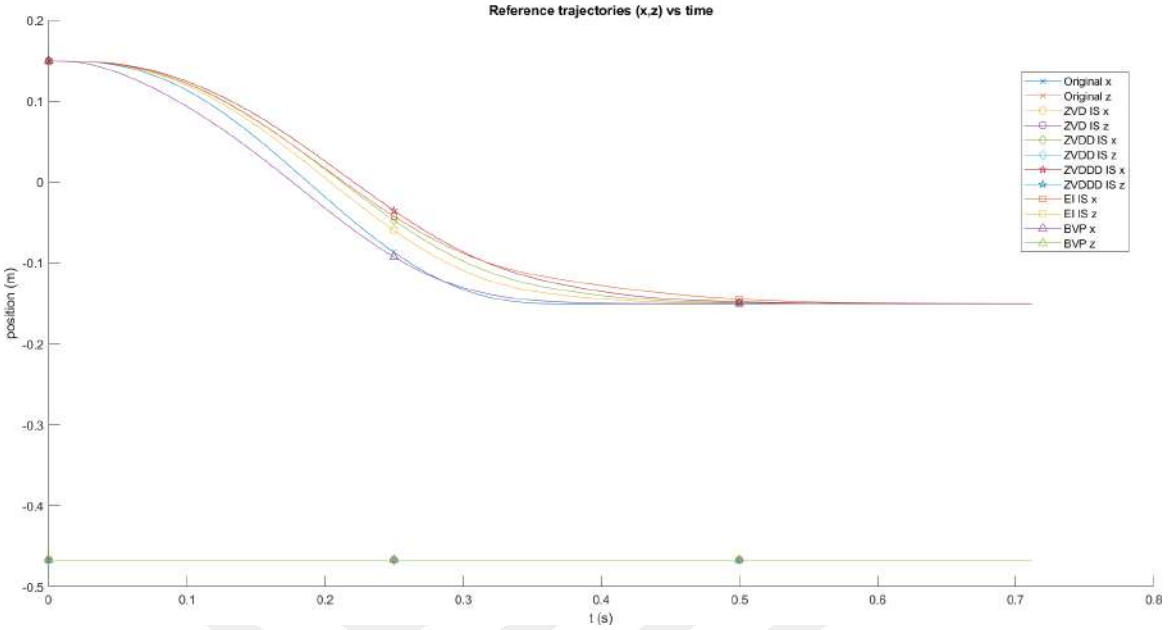

Figure 3.9: Reference EE trajectory

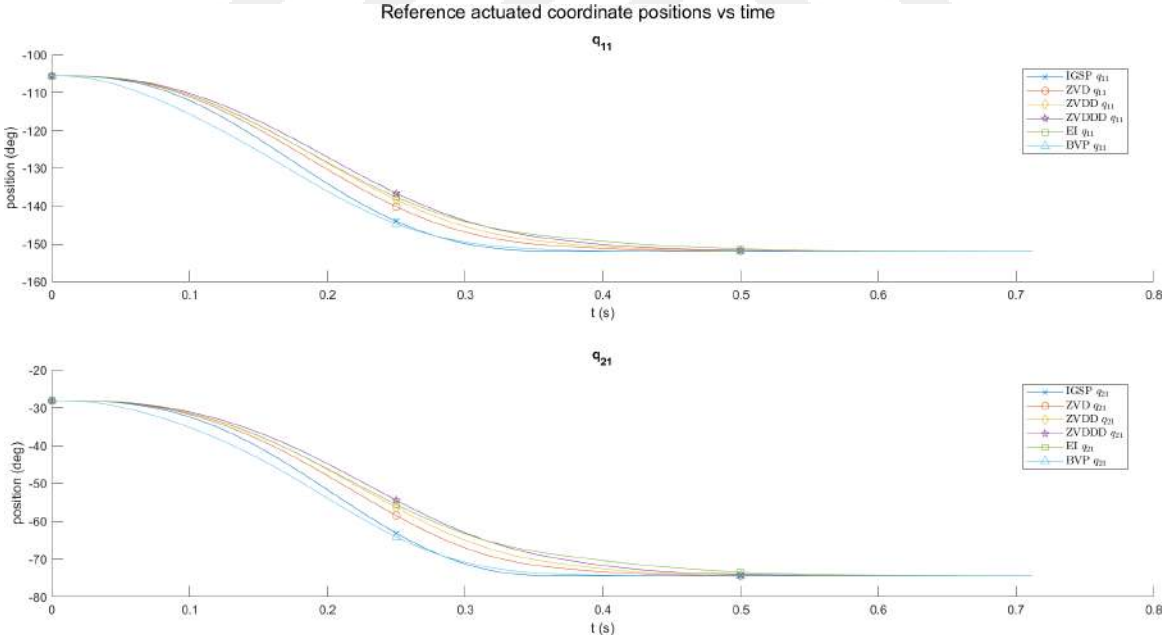

Figure 3.10: Reference actuated coordinate trajectory

	IGSP	ZVD	EI	ZVDD	ZVDDD	RTR
5% t_{ss} EE position (s)	0.31785	0.39312	0.49036	0.41748	0.43994	0.33562
% of Introduced time delay (s)	0	23.6793	54.2721	31.3448	38.4114	5.58874
Max $\|\boldsymbol{\tau}\|$ (Nm)	15.0892	14.2612	13.9566	13.9239	13.7142	15.9045
SS $\|\mathbf{p}_e\|$ (m)	$1.126E^{-4}$	$7.12E^{-5}$	$1.138E^{-4}$	$9.547E^{-5}$	$1.15E^{-4}$	$1.059E^{-4}$
q_{13} Overshoot (deg)	8.7512	7.1129	6.3665	6.7795	6.52	6.9871
q_{23} Overshoot (deg)	-2.1395	-2.478	-3.0258	-2.5926	-2.7729	-1.9632
q_{13} Undershoot (deg)	0.73493	1.2821	1.5531	1.58	1.84	0.27414
q_{23} Undershoot (deg)	-8.1901	-6.7936	-6.2731	-6.2346	-5.7414	-7.7411
RMS of q_{13} (deg)	214.255	207.7548	205.5076	212.3329	214.6556	207.0094
RMS of q_{23} (deg)	239.733	213.7628	216.3267	211.2964	208.2982	221.4868

Table 3.3: Comparison of trajectory planning methods

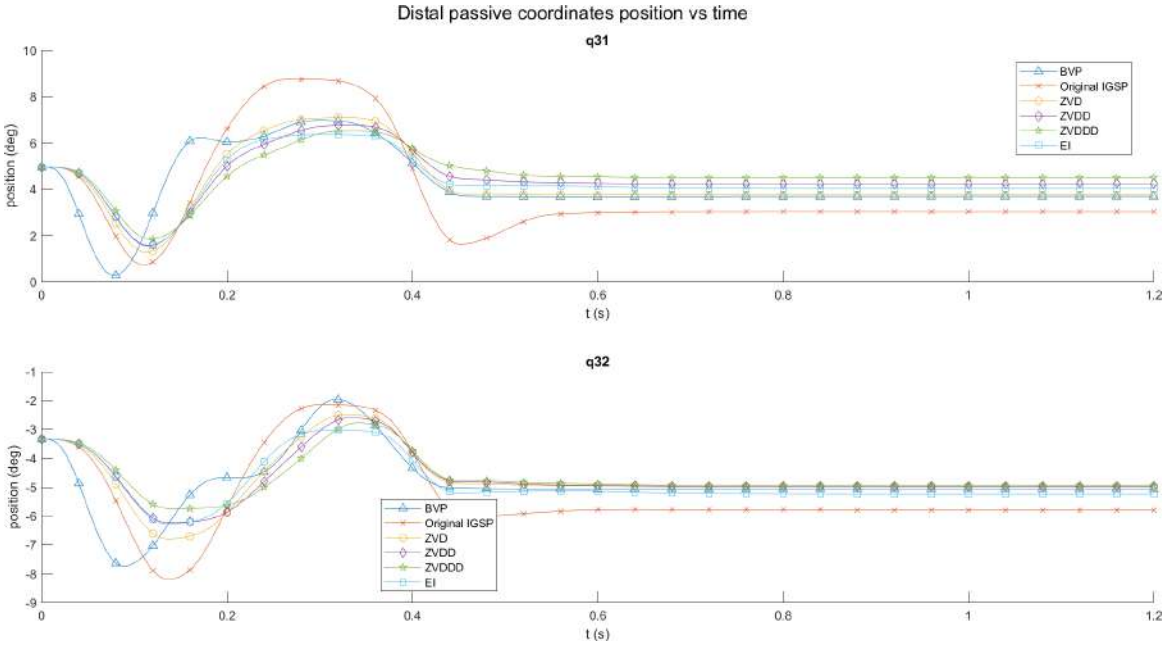

Figure 3.11: Distal unactuated coordinate oscillations

Except slightly lower undershoot of q_{13} with RTR in comparison to IGSP, overall, RTR oscillates less. This can be observed easier on q_{13} however it is not easy to say for q_{23} oscillations. In the interval of $\begin{bmatrix}0.175 & 0.3\end{bmatrix}$s RTR has a settled point which stays stable for couple of milliseconds and then reaches the overshoot value with IGSP. Like in trial 2, in the interval of $\begin{bmatrix}0.43 & 1.2\end{bmatrix}$s, distal unactuated coordinates with RTR converges to it's final position whereas for IGSP, it is still in action. This behavior of IGSP can be seen for both q_{13} and q_{23} in comparison to other methods. This can cause a problem in case IGSP is used as a fast P&P trajectory because even if the motion with IGSP is finished at 0.34s, distal unactuated coordinates stop moving at nearly 0.6s. If R-min forced to move back to the original position again 0.34s, the oscillation frequency of the distal unactuated coordinates will increase due to the potential energy stored by the first motion. This is definitely an unwanted behavior for repeated tasks such as P&P operations. To compare ISs with RTR, one should note that there is a compromise. For faster motion, which can be very useful for fast P&P operations, RTR is the best candidate however it is clearly seen that all the ISs have lesser residual oscillations but they are slower than RTR. Among ISs, ZVDDD, ZVDD, EI and ZVD are listed from best to worst in terms of residual oscillations respectively. Thus, depending on the need, best candidate can be chosen accordingly. 5% t_{ss} EE trajectory tracking, EE trajectory tracking error, 5% t_{ss} EE trajectory tracking error and applied torques are given in Section A.1.3.

3.2 Experimental results

Experimental results of all the trials that were simulated in Section 3.1 are shown in this Section. One should note that there is no automated setup to calibrate R-min and hence it is calibrated manually. Also, with different trajectories, distal unactuated coordinate reach different final positions. Thus, the more trajectories are tested, the more error accumulates.

3.2.1 Trial 1

Simulated trajectories in Section 3.1.1 were implemented on R-min. The results are shown below as:

	IGSP	ZVD	EI	ZVDD	ZVDDD	RTR
5% t_{ss} EE position (s)	0.25899	0.3559	0.45164	0.39212	0.42792	NaN
% of Introduced time delay (s)	0	37.4384	74.3868	51.4047	65.2287	NaN
Max $\|\boldsymbol{\tau}\|$ (Nm)	19.0549	18.5656	18.0078	18.5307	17.563	NaN
SS $\|\mathbf{p}_e\|$ (m)	$6.655E^{-3}$	$6.7408E^{-3}$	$6.6649E^{-3}$	$6.1224E^{-3}$	$6.087E^{-3}$	NaN
q_{13} Overshoot (deg)	18.4801	11.9665	9.78394	10.4457	9.79656	NaN
q_{23} Overshoot (deg)	0.50955	-1.655	-1.8066	-2.0623	-2.012	NaN
q_{13} Undershoot (deg)	-4.1422	0.25521	0.5957	0.72003	1.0062	NaN
q_{23} Undershoot (deg)	-9.7658	-7.7157	-6.829	-6.5762	-5.8211	NaN
RMS of q_{13} (deg)	105.9174	77.44362	74.22776	77.52765	78.12546	NaN
RMS of q_{23} (deg)	76.5166	64.7946	62.4594	62.9478	60.2584	NaN

Table 3.4: Comparison of trajectory planning methods

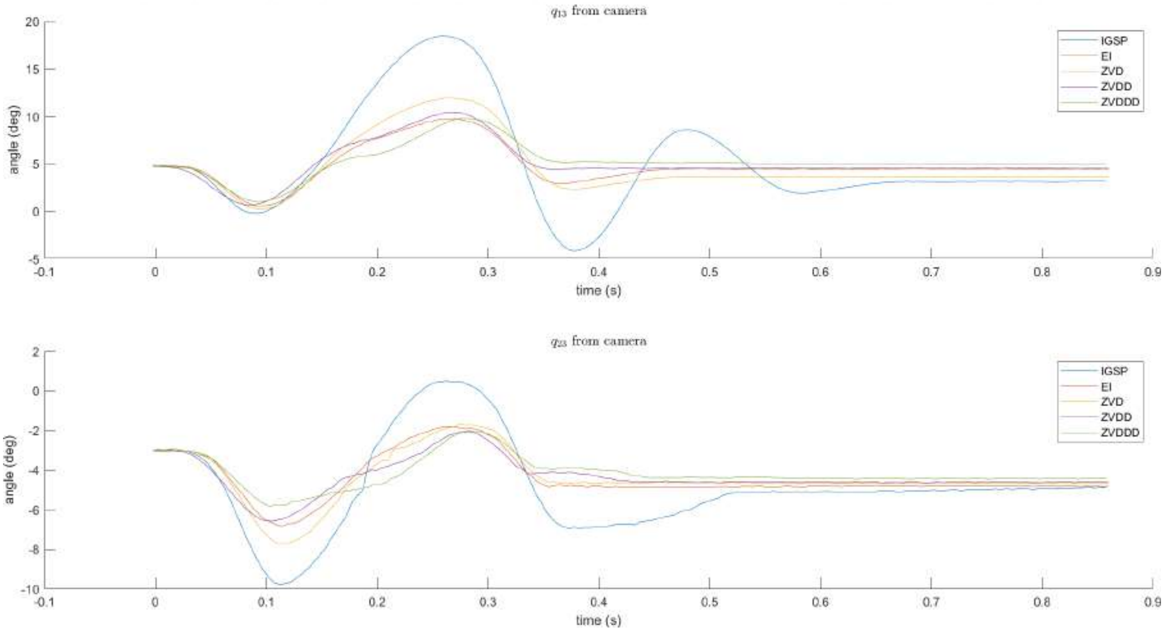

Figure 3.12: Distal unactuated coordinate oscillations

All the trajectories start the motion with $\approx 6E^{-3}$m position error. It is clearly seen from Figures 3.5 and 3.12 that the friction forces acting on q_{23} on R-min is more than the simulation model. The residual oscillations are listed ZVDDD, ZVDD, EI, ZVD and IGSP from best to worst respectively. The SS EE position error remained maximum of $\approx 0.75E^{-3}m$ w.r.t. initial calibration error. Followed trajectories, proximal unactuated coordinates and applied torques are given in Section A.2.1.

3.2.2 Trial 2

Simulated trajectories in Section 3.1.2 were implemented on R-min. The results are shown below as:

	IGSP	ZVD	EI	ZVDD	ZVDDD	RTR
5% t_{ss} EE position (s)	0.26875	0.34488	0.45202	0.38033	0.41615	0.35802
% of Introduced time delay (s)	0	28.3266	68.1932	41.516	54.8463	33.216
Max $\lvert\boldsymbol{\tau}\rvert$ (Nm)	22.4117	21.552	21.0836	21.201	19.684	19.3802
SS $\lvert\mathbf{p}_e\rvert$ (m)	$5.35E^{-3}$	$5.42E^{-3}$	$4.89E^{-3}$	$5.66E^{-3}$	$5.30E^{-3}$	$4.98\text{E}E^{-3}$
q_{13} Overshoot (deg)	17.2616	10.3149	6.59322	7.60466	6.73313	9.31335
q_{23} Overshoot (deg)	1.2461	-0.4181	-0.13272	-0.85717	-1.6364	-2.5212
q_{13} Undershoot (deg)	-1.6249	0.61846	0.78564	0.97328	0.86181	1.0521
q_{23} Undershoot (deg)	-11.0598	-9.21822	-8.23771	-8.20455	-7.77261	-7.04866
RMS of q_{13} (deg)	336.2289	259.4919	222.6673	248.4344	230.2125	247.9253
RMS of q_{23} (deg)	253.2001	236.6566	224.1047	223.9055	220.5714	223.3375

Table 3.5: Comparison of trajectory planning methods

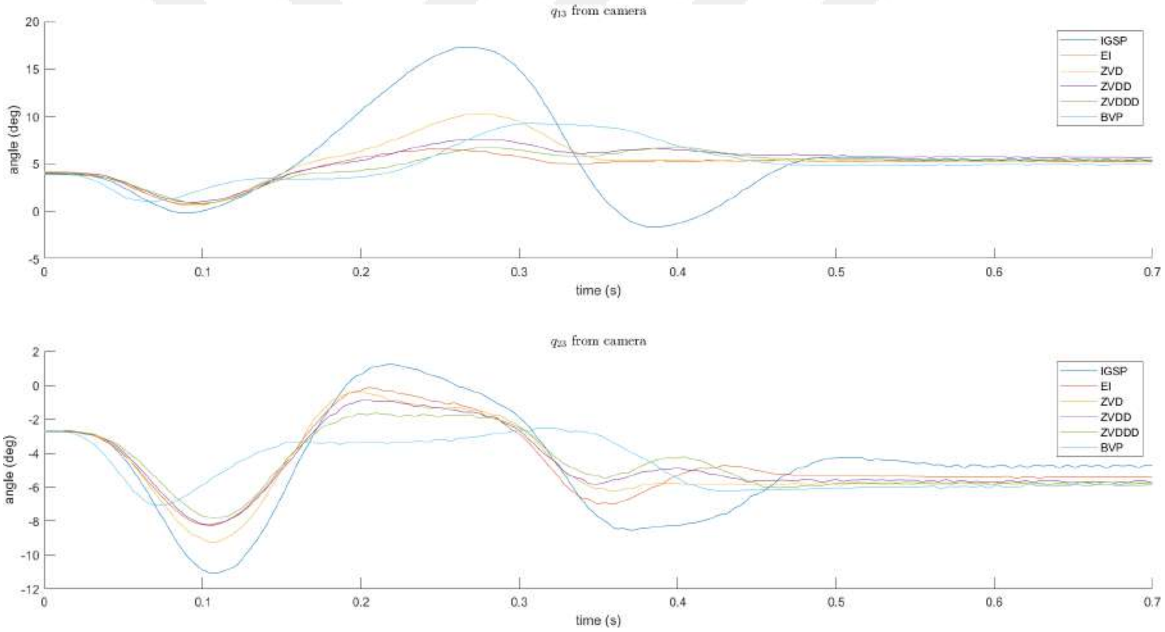

Figure 3.13: Distal unactuated coordinate oscillations

All the trajectories start the motion with $\approx 4E^{-3}$m position error. It is clearly seen from Figures 3.8 and 3.13 that the residual oscillations of distal unactuated coordinates from simulation and experiment. However, the residual oscillation of q_{13} with IGSP trajectory in the interval of $\left[0.4 \quad 0.7\right]$s in simulation is not observed in experiment. This friction on q_{13} of R-min also drastically reduced the oscillations with other trajectory planning methods as well. That makes a bit hard to decide for q_{13} because except IGSP, other methods are close to each other but for q_{23}, it is obvious that RTR has the least oscillatory behavior hence, that makes RTR best trajectory planning method for this case. The SS EE position error remained maximum of $\approx 1.5E^{-3}m$ w.r.t. initial calibration error. Followed trajectories, proximal unactuated coordinates and applied torques are given in Section A.2.2.

3.2.3 Trial 3

Simulated trajectories in Section 3.1.3 were implemented on R-min. The results are shown below as:

	IGSP	ZVD	EI	ZVDD	ZVDDD	RTR
5% t_{ss} EE position (s)	0.33621	0.40859	0.50564	0.42964	0.46116	0.3579
% of Introduced time delay (s)	0	21.528	50.3917	27.7873	37.1628	6.45043
Max $\|\boldsymbol{\tau}\|$ (Nm)	20.6968	20.1278	19.2356	19.0029	19.6665	20.6905
SS $\|\mathbf{p}_e\|$ (m)	$4.85E^{-3}$	$5.44E^{-3}$	$5.62E^{-3}$	$5.17E^{-3}$	$5.53E^{-3}$	$5.02E^{-3}$
q_{13} Overshoot (deg)	9.3414	8.3474	6.0336	7.1387	6.8644	8.9754
q_{23} Overshoot (deg)	-1.7736	-2.3396	-2.1447	-2.0908	-2.3897	-2.6802
q_{13} Undershoot (deg)	1.3165	1.9404	2.0465	1.8877	2.3178	0.8622
q_{23} Undershoot (deg)	-8.023	-6.5357	-6.2423	-5.9838	-5.8646	-7.1979
RMS of q_{13} (deg)	221.8884	249.6108	229.4627	228.7039	240.7693	237.497
RMS of q_{23} (deg)	225.2443	223.9005	214.0166	216.7185	213.1925	233.0802

Table 3.6: Comparison of trajectory planning methods

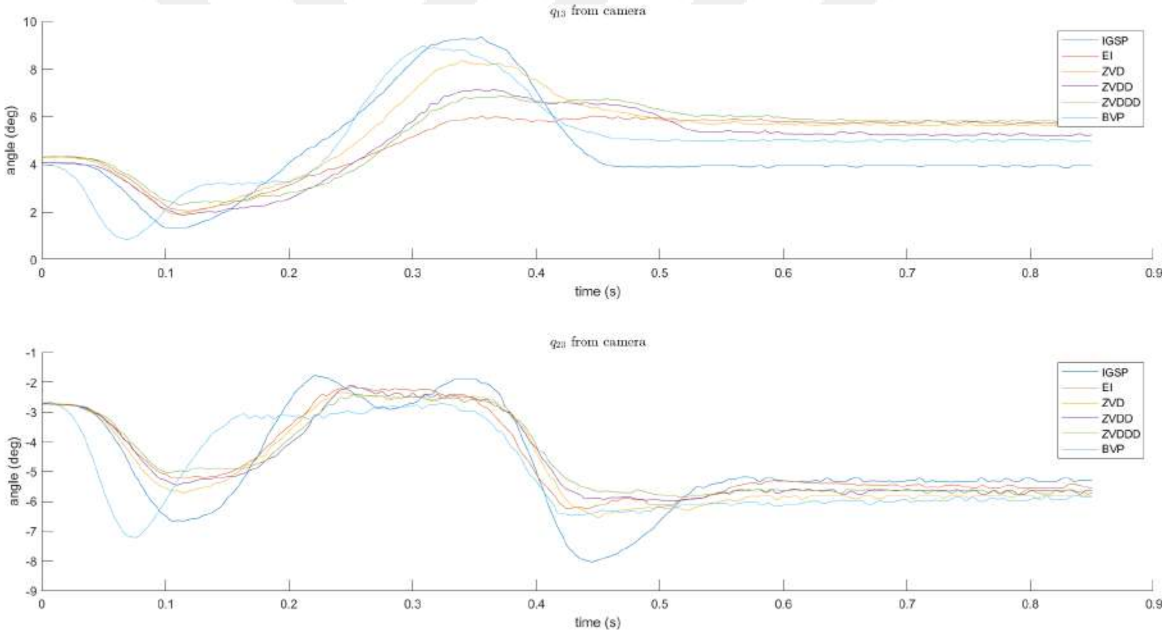

Figure 3.14: Distal unactuated coordinate oscillations

All the trajectories start the motion with ≈ $4.5E^{-3}$m position error. The same problem that is stated for IGSP trajectory in Section 3.1.3 was valid for experimental results. Also, for q_{23}, in the interval of $\begin{bmatrix}0.2 & 0.35\end{bmatrix}$s, an additional small oscillation happened which did not happen in simulation. The experiemntal result of unactuated coordinates came out as expected from simulation but the oscillation undershoot and overshoot magnitudes are less due to actual friction. For safety cautions, except IGSP, all trajectories can be implemented for P&P operations. RTR is the fastest motion with slightly more oscillations in comparison to ISs. In the interval $\begin{bmatrix}0 & 0.15\end{bmatrix}$s, RTR oscillation bounced back with an oscillation for both distal unactuated coordinates but thereafter it was kept constant in the interval of $\begin{bmatrix}0.15 & 0.375\end{bmatrix}$s for q_{23}. For q_{13}, the only noticeable difference happened in the interval of $\begin{bmatrix}0.22 & 0.4\end{bmatrix}$s. In those seconds, the overshoot of RTR was 2° more than ZVDDD. Overall, RTR is better than ZVDDD except some small differences thus it is selected the best for the purpose of this study. However, if the time is not essential and one desires the least oscillatory motion, among

ISs, ZVDDD, ZVDD, EI are listed from best to worst. The SS EE position error remained maximum of $\approx 1.5E^{-3}m$ w.r.t. initial calibration error. Followed trajectories, proximal unactuated coordinates and applied torques are given in Section A.2.3.

3.3 Comparison of simulation and experimental results

The modeled robot and physical robot are slightly different in terms of inertial parameters, friction coefficients and calibration errors. For IS methods, robustness to model uncertainties increases by equating higher order derivatives of Equation (2.20) or by allowing it to have small percentage of oscillation. In trial 1, oscillations of distal unactuated coordinates from best to worst ZVDDD, ZVDD, EI, ZVD IS were listed. In trial 2, RTR trajectory has almost the same t_{ss} with ZVD IS which is considered the worst IS for the residual oscillations among ISs presented in this master thesis. However, with RTR, the residual oscillations are taken care of even better than ZVDDD IS which is the best IS. Thus, that makes RTR trajectory planning method the best candidate for P&P operations with R-min. In trial 3, a fair comparison between IGSP and RTR were made by setting the t_{ss} same. For IGSP, it took more time to stop after RTR stopped. The residual oscillations are considerably smaller for RTR in comparison to IGSP but not for ISs. This is the compromise to be made. To sum up, in the scope of this study, safety and the speed of P&P operation are essential. The oscillations are in acceptable level for RTR and ISs except the initial oscillations were caused by the force acting on the distal unactuated coordinates when the motion starts. The fastest and safe motion, BVP is one to choose, for lesser residual oscillations, one should ZVDDD, ZVDD, EI, ZVD from best to worst respectively.

Conclusion

In this master thesis, considerably new robotic type, UA mechanical systems, their raison d'être, their characteristics and dynamics, what makes them appealing were explained. R-min, an example robot to this kind, was designed to work collaboratively in a work environment with an operator. Due to its elastic kind of behavior which makes it oscillate and change its configuration as it is shown in Figure 1.2. To prevent this, proven robust trajectory planning methods were examined and implemented both in simulation environment and experimentally.

In Chapter 1, carried out work of R-min's design, dynamics, trajectory planning and control studies were explained. The existing trajectory planning was based on extraction of static equilibrium points to obtain a trajectory but in motion, the robot passes these points with non-zero velocity and acceleration. This causes R-min to oscillate. The control strategy, conventional CTC, uses the aforementioned trajectory as well as the velocity and acceleration profiles to compute necessary torques to track. However, the control approach also contributes to this residual oscillations and passively limit applied torque inputs.

In Chapter 2, five trajectory planning methods and their implementation on R-min were explained elaborately. The first one was RTR which was experimentally validated on a CDPR. The remaining four were robust ISs that are used in various applications. These ISs were ZVD, EI, ZVDD and ZVDDD which reduce residual oscillations at the modeling frequency and provide robustness against model uncertainties.

In Chapter 3, simulation and experimental results of the mentioned methods were compared. The comparison criteria were 5% t_{ss} of EE position $\mathbf{p}$, SS EE position error $|\mathbf{p}_e|$, applied torques $\boldsymbol{\tau}$ and amount of residual oscillations of the distal unactuated coordinates $\mathbf{q}_3$. From best to worst in terms of residual oscillations of $\mathbf{q}_3$, RTR, ZVDDD, ZVDD, EI, ZVD, IGSP were listed. But of course, in every engineering field, when there is a gain there is also loss. For this case, RTR is computationally expensive and cumbersome because at each iteration the optimization evaluates ODE $\begin{bmatrix}0 & T\end{bmatrix}$s. Also, it does not guarantee to find a global minimum. Furthermore, the bounds of the optimization parameters are not known because they do not represent physical quantities. During the optimization, it took 23 hours to converge to a local minimum by exploring 105000 functions with *patternsearch* which was better than the local minimum of *fmincon*. IS methods, in contrast, are straightforward and not as computationally expensive. However, the time delays introduced by ISs are deterministic and inevitable whereas the duration of motion is predefined in RTR. One should remember that for elastic systems conventional IS methods introduce residual oscillations. For R-min oscillations with two different magnitudes and periods were introduced to the actuated coordinates by maximum of $\approx 0.1deg$ which is shown in Figure 2.15 however a simple solution was introduced as it is shown in Figure 2.17 and these oscillations were damped by the joint frictions on the physical robot. To sum up, for the considerably lesser oscillation and the fastest motion, one should chose RTR but only if the system parameters are perfectly known. For ISs, the only drawback is the introduced time delays. One should note that, for R-min, the introduced time delay was at maximum of 74.3768% (in experiment) w.r.t. IGSP but for repeating P&P operations, these time delays accumulate the time more than RTR trajectory. Other than that, ZVDDD, ZVDD, EI and ZVD are the options listed from best to worst. For less time delay and easy computation, one should chose ZVD, ZVDD, ZVDDD and EI. To sum up, this study aimed for the UA robot, R-min, to track a fast and oscillation-free trajectory with acceptable SS EE position error. RTR and ZVDDD are finest methods out of all for all the criteria.

Appendix A

Results

A.1 Simulation results

A.1.1 Trial 1

Detailed simulation result shows in Section 3.1.1 is given below as:

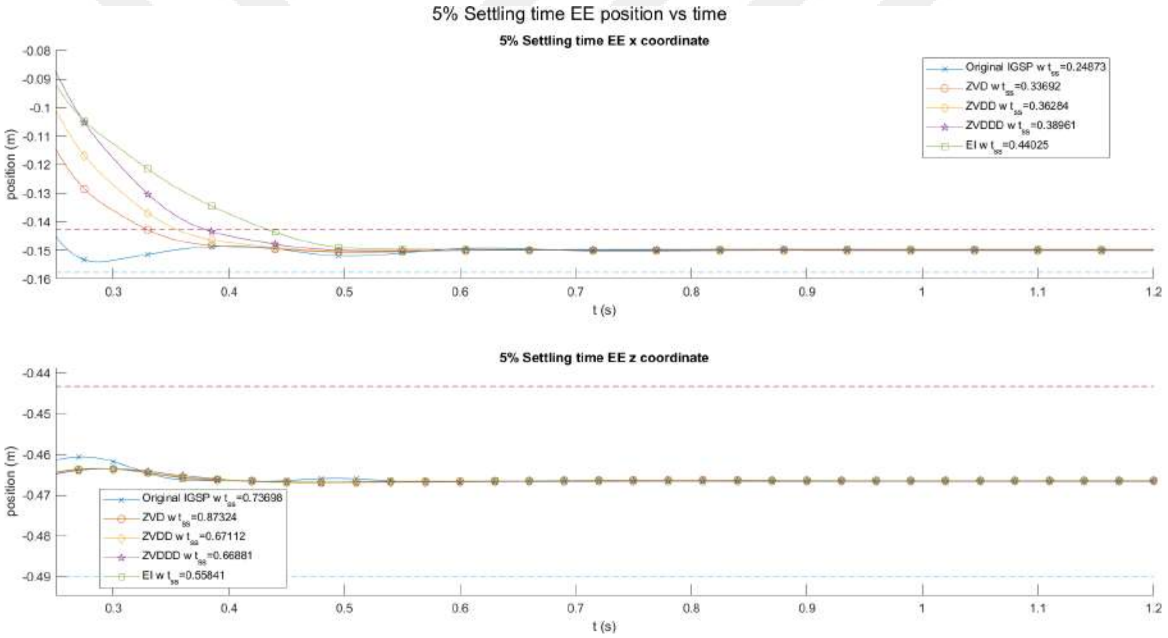

Figure A.1: EE trajectory tracking with t_{ss}

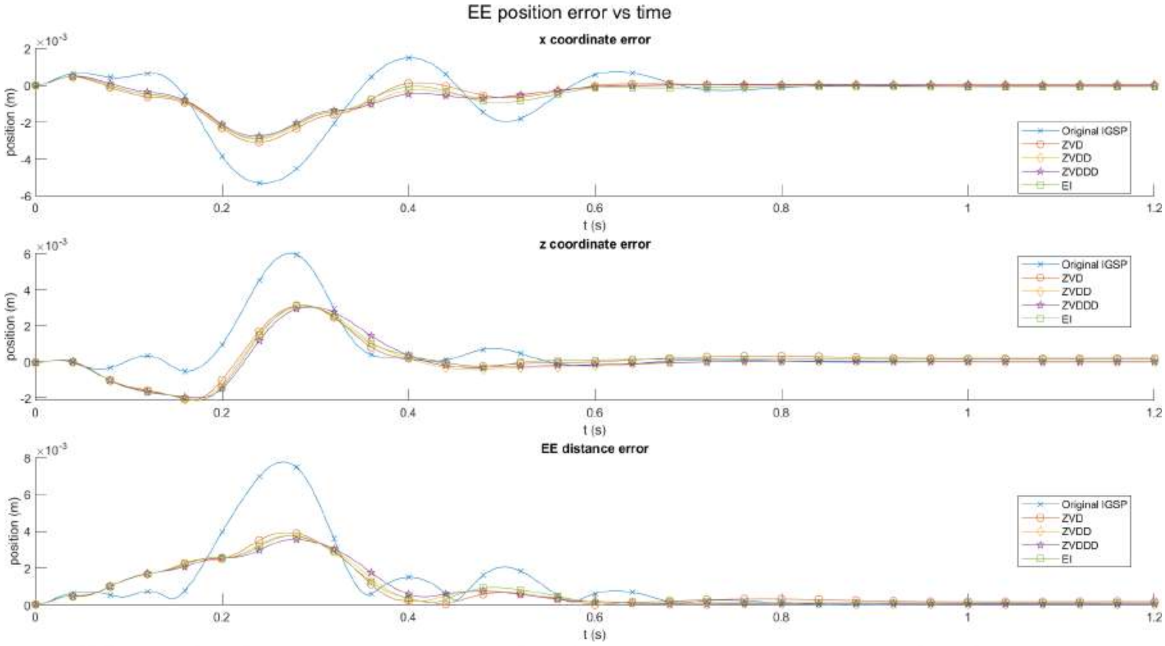

Figure A.2: EE trajectory tracking error

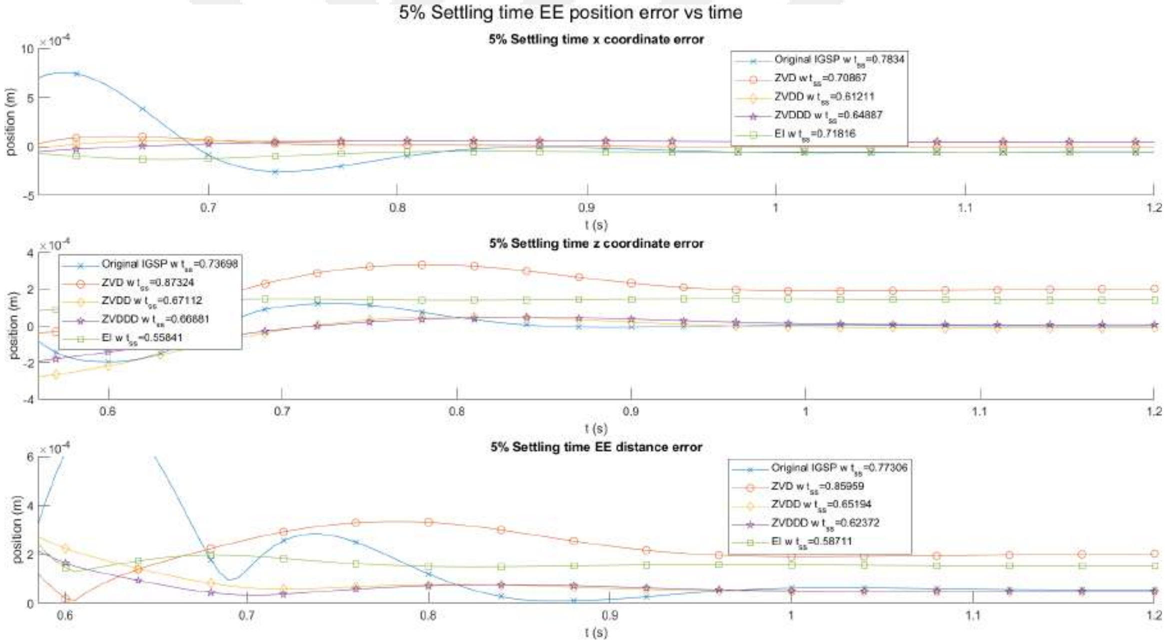

Figure A.3: EE trajectory tracking error with t_{ss}

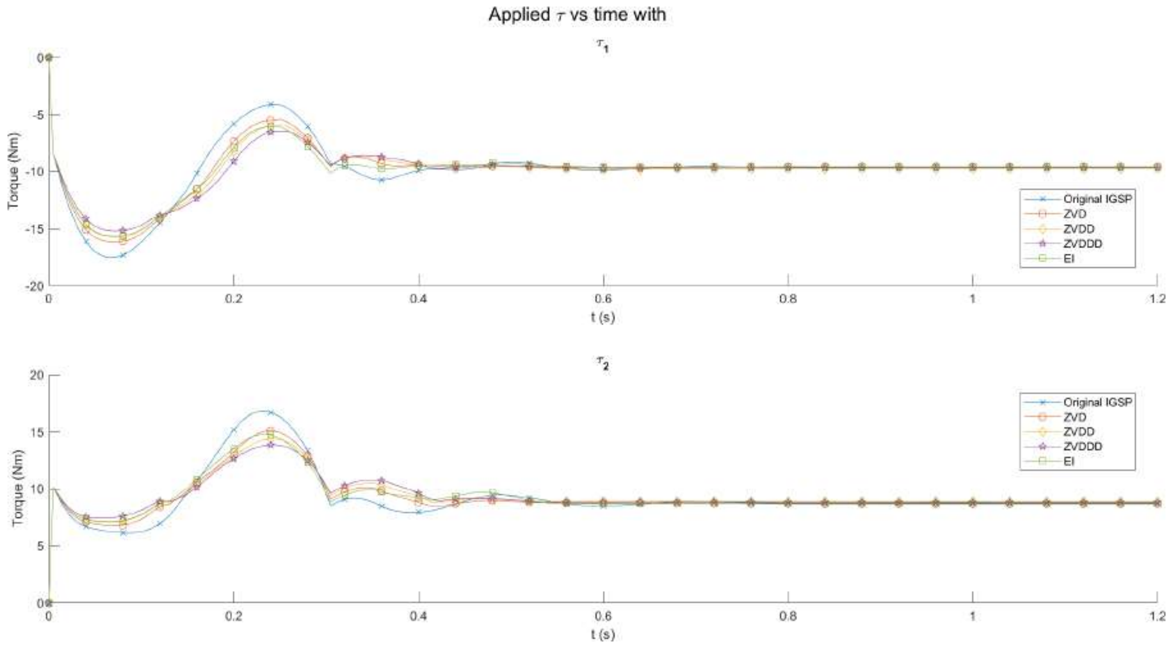

Figure A.4: Applied $\boldsymbol{\tau}$

A.1.2 Trial 2

Detailed simulation result shows in Section 3.1.2 is given below as:

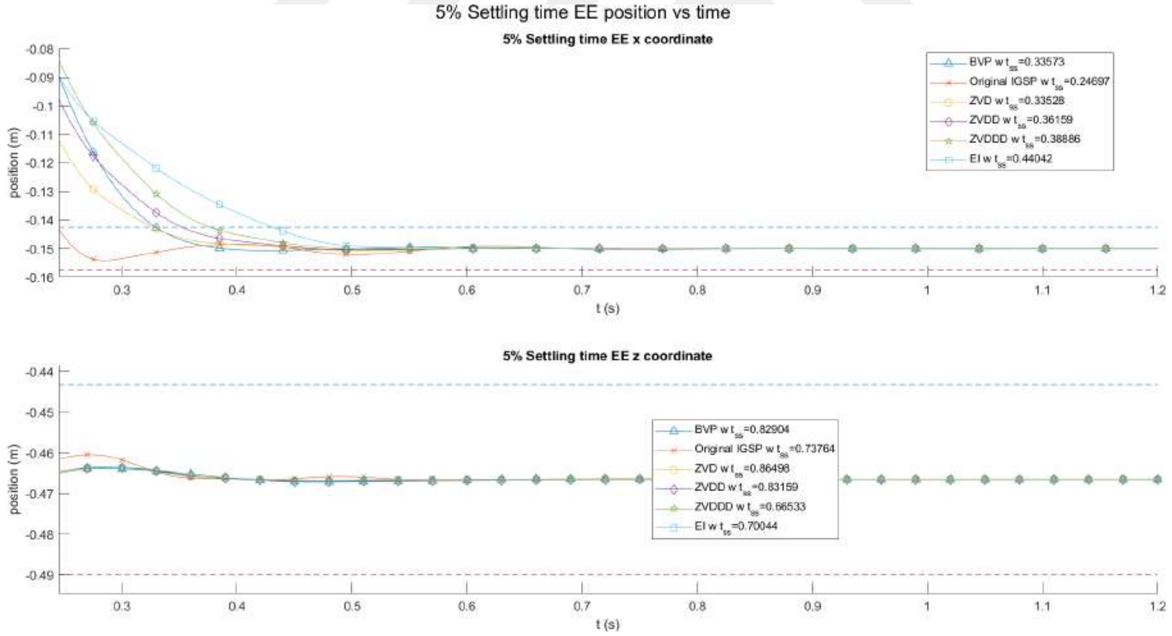

Figure A.5: EE trajectory tracking with t_{ss}

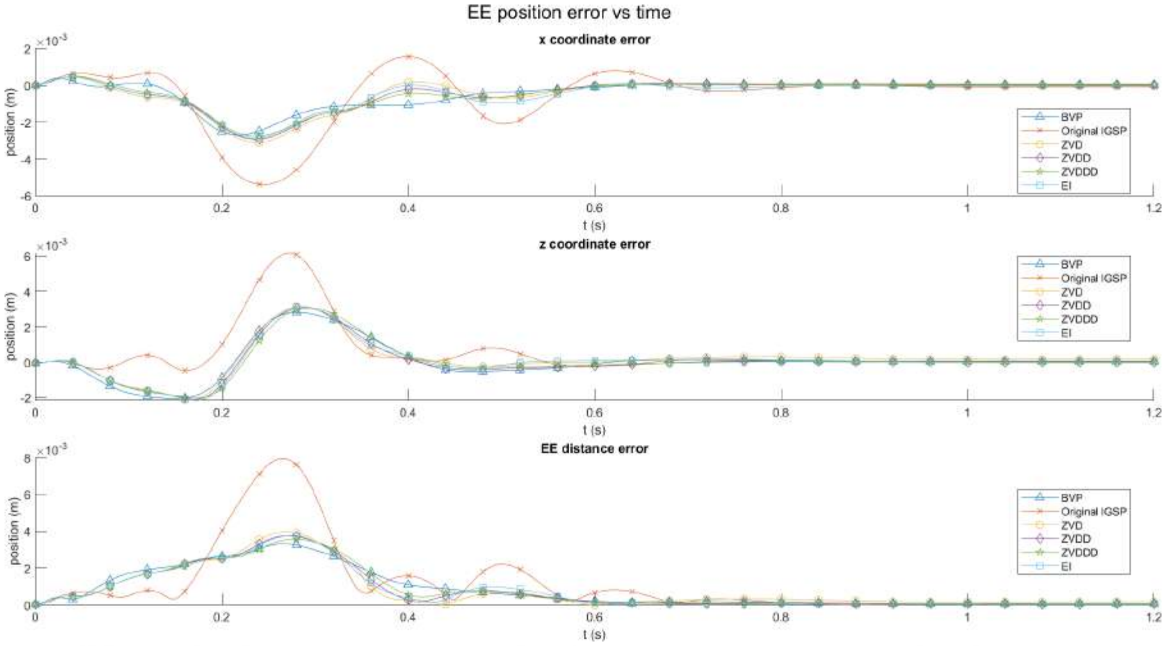

Figure A.6: EE trajectory tracking error

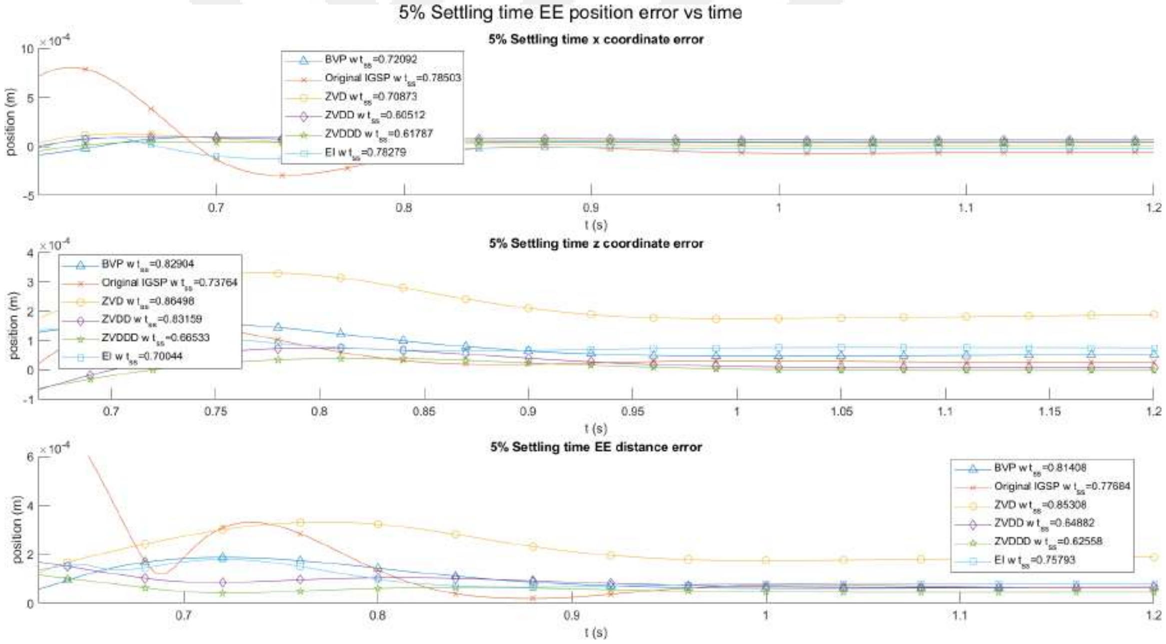

Figure A.7: EE trajectory tracking error with t_{ss}

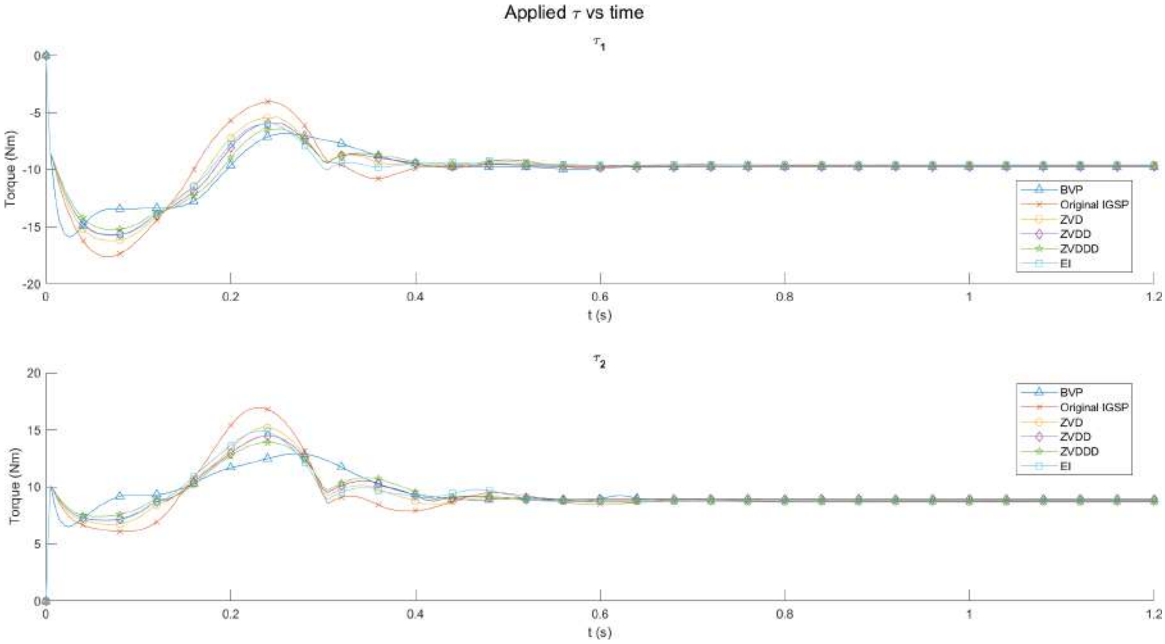

Figure A.8: Applied $\boldsymbol{\tau}$

A.1.3 Trial 3

Detailed simulation result shows in Section 3.1.3 is given below as:

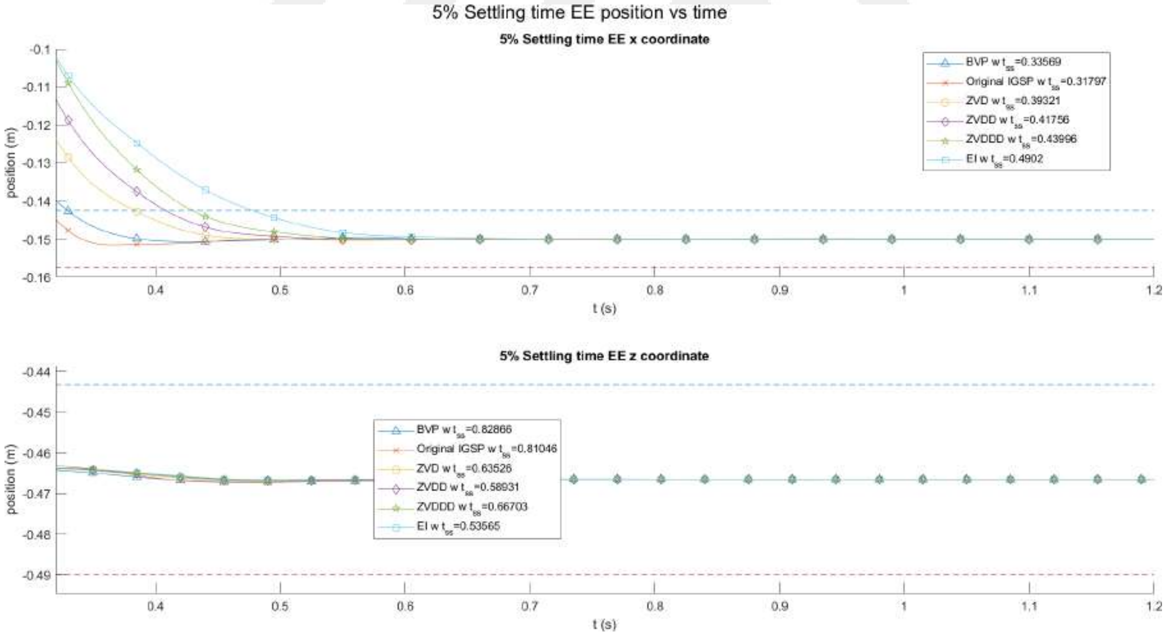

Figure A.9: EE trajectory tracking with t_{ss}

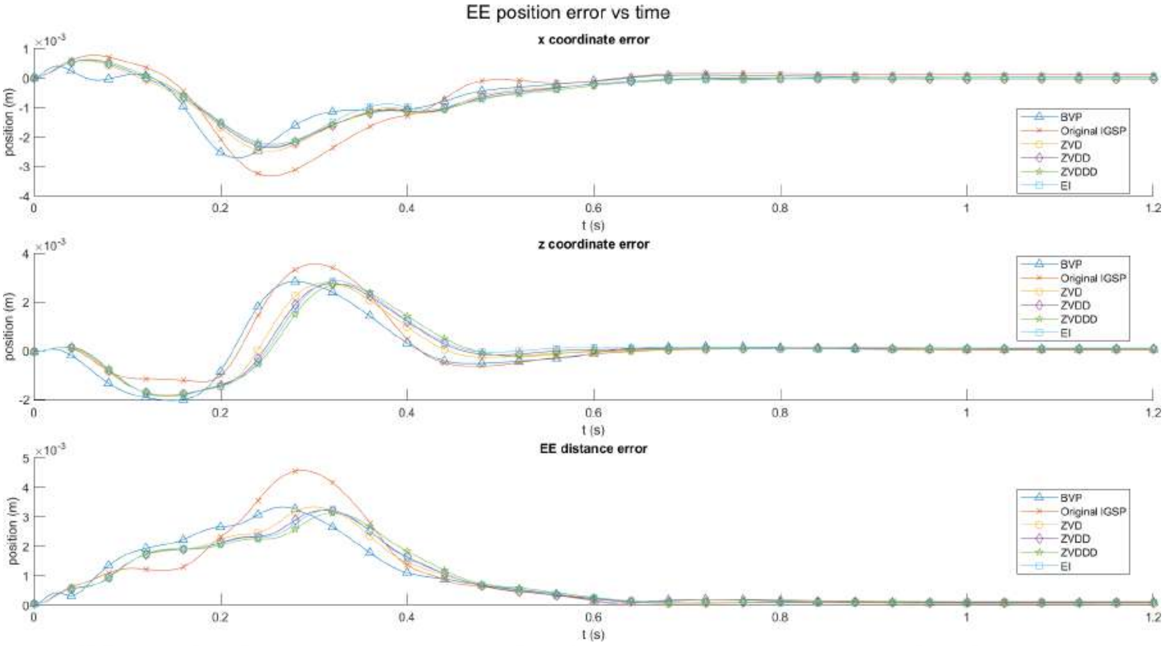

Figure A.10: EE trajectory tracking error

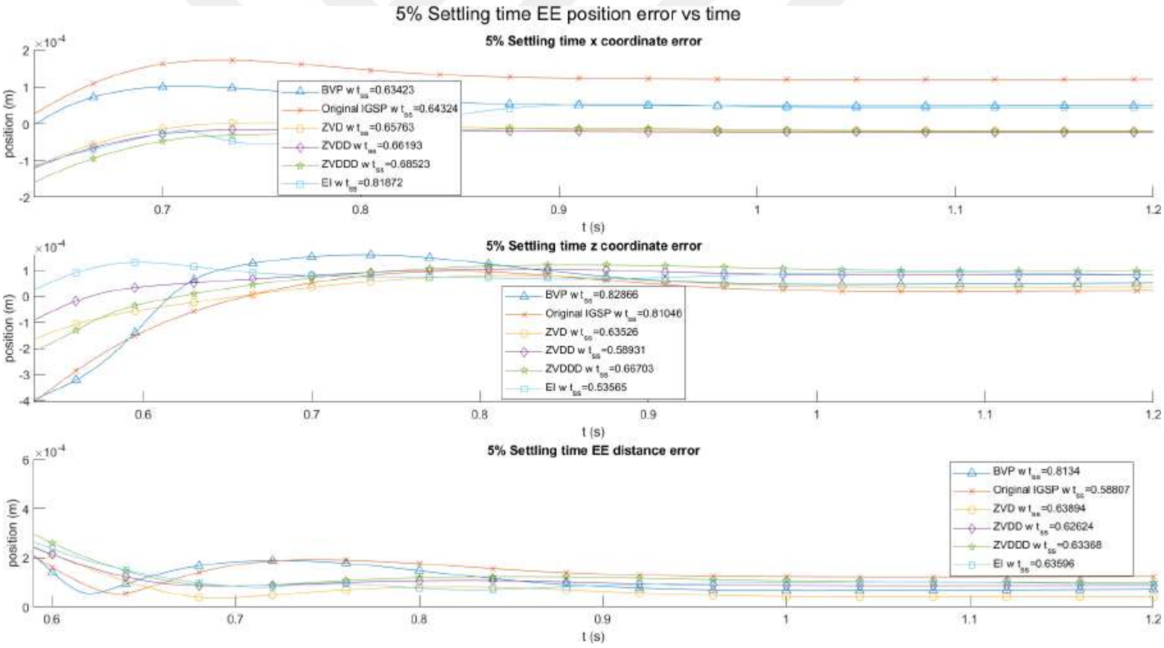

Figure A.11: EE trajectory tracking error with t_{ss}

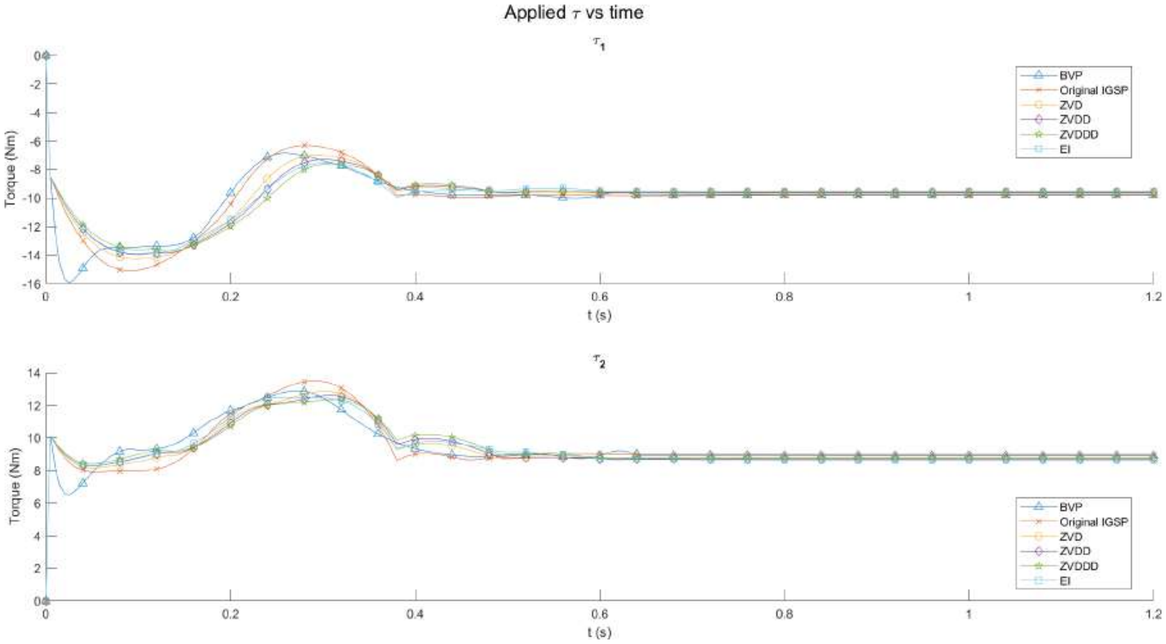

Figure A.12: Applied $\boldsymbol{\tau}$

A.2 Experimental results

A.2.1 Trial 1

Detailed experimental result shows in Section 3.2.1 is given below as:

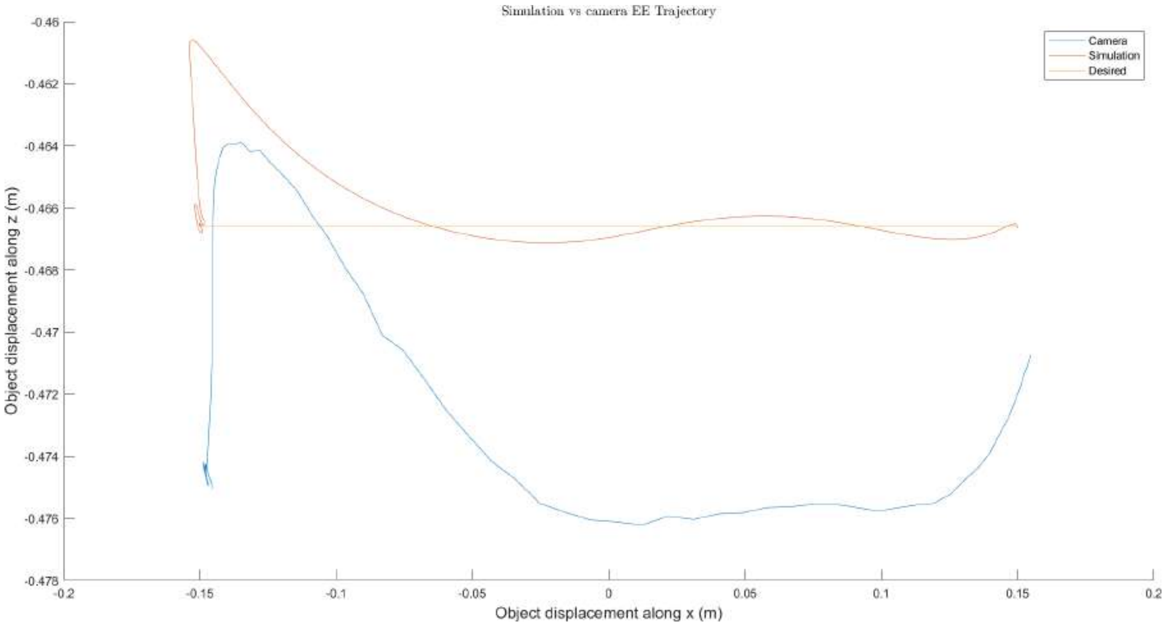

Figure A.13: EE trajectory tracking (IGSP)

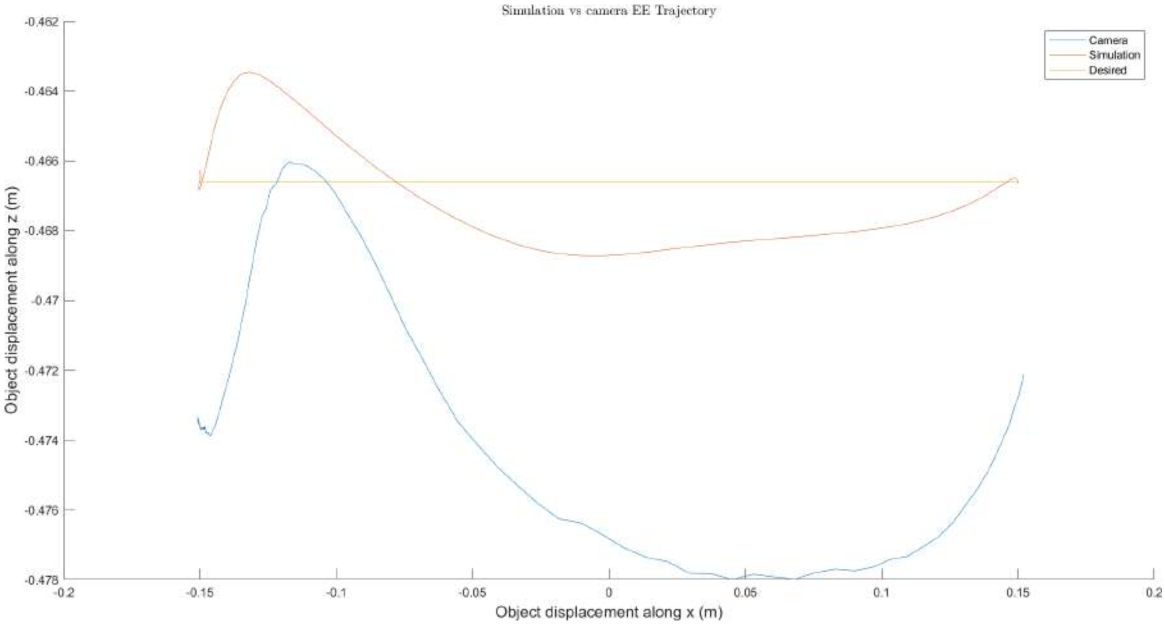

Figure A.14: EE trajectory tracking (ZVD)

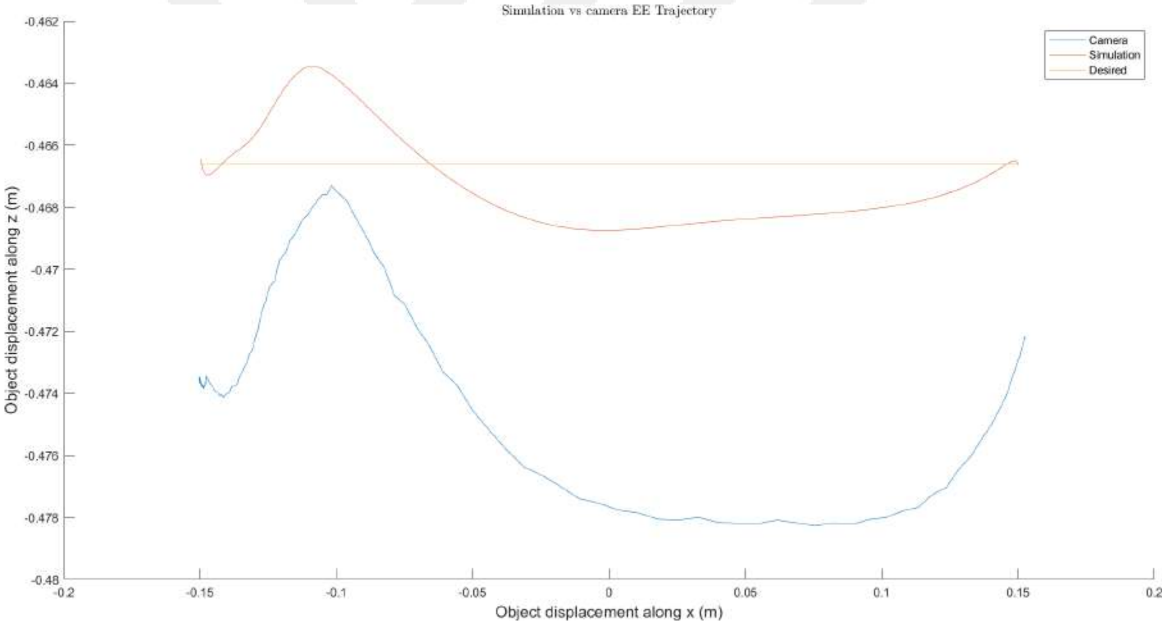

Figure A.15: EE trajectory tracking (EI)

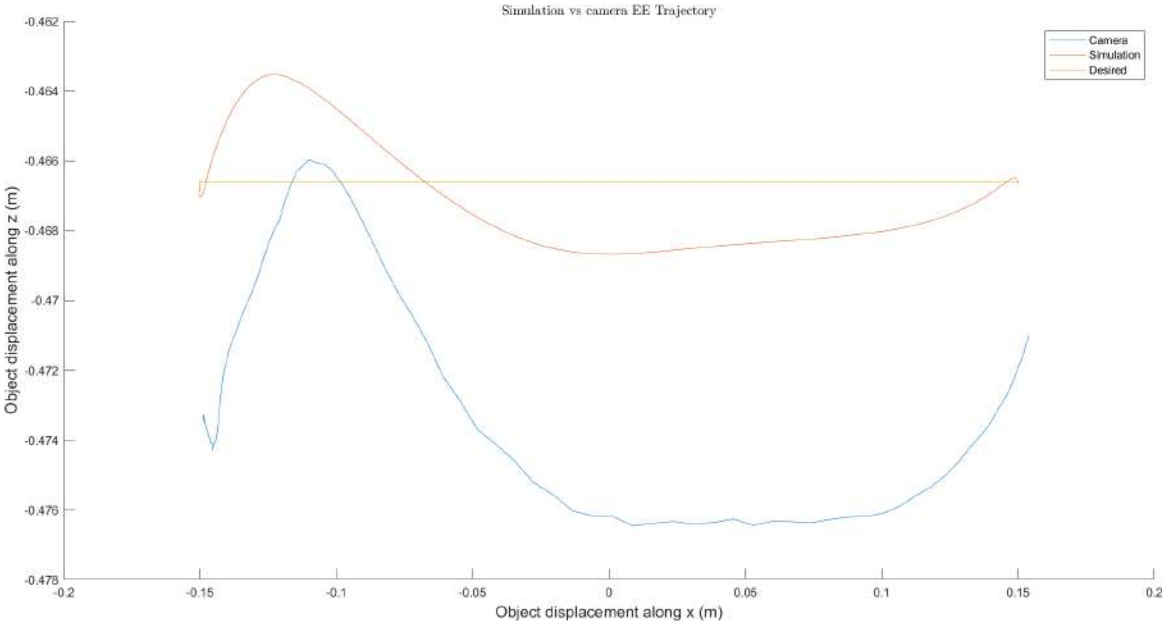

Figure A.16: EE trajectory tracking (ZVDD)

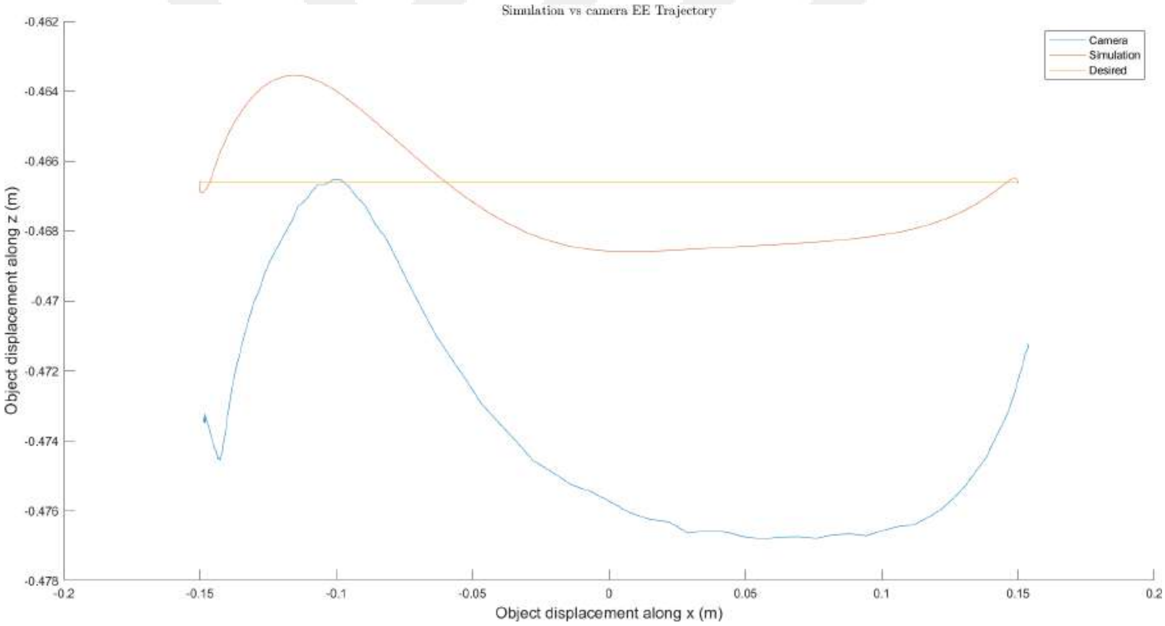

Figure A.17: EE trajectory tracking (ZVDDD)

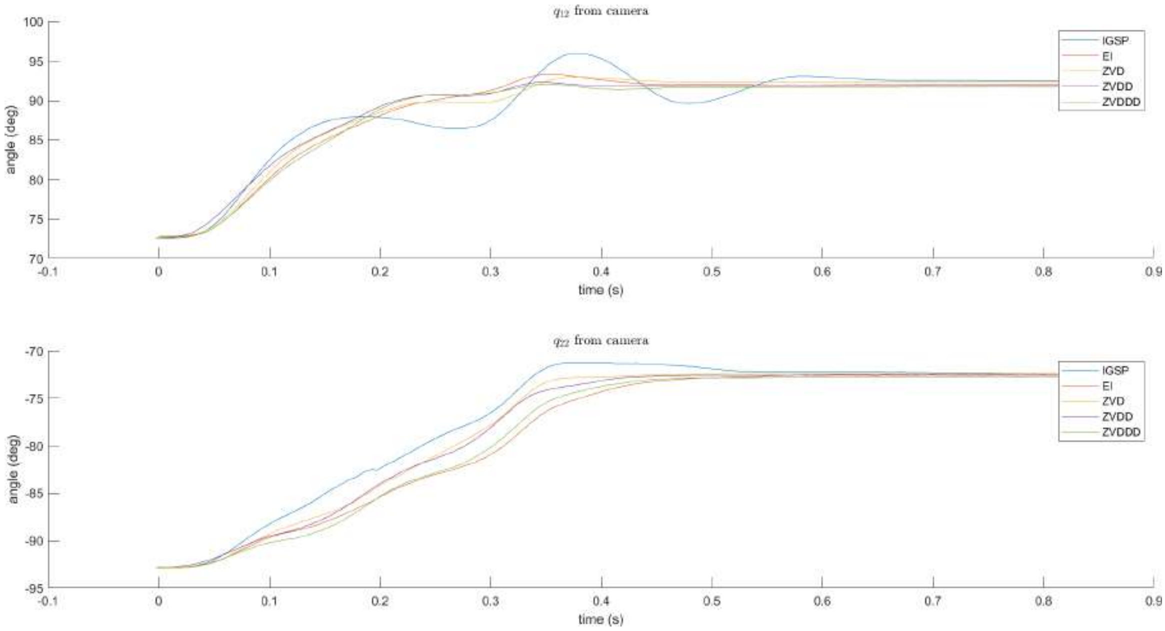

Figure A.18: Proximal unactuated coordinate oscillations

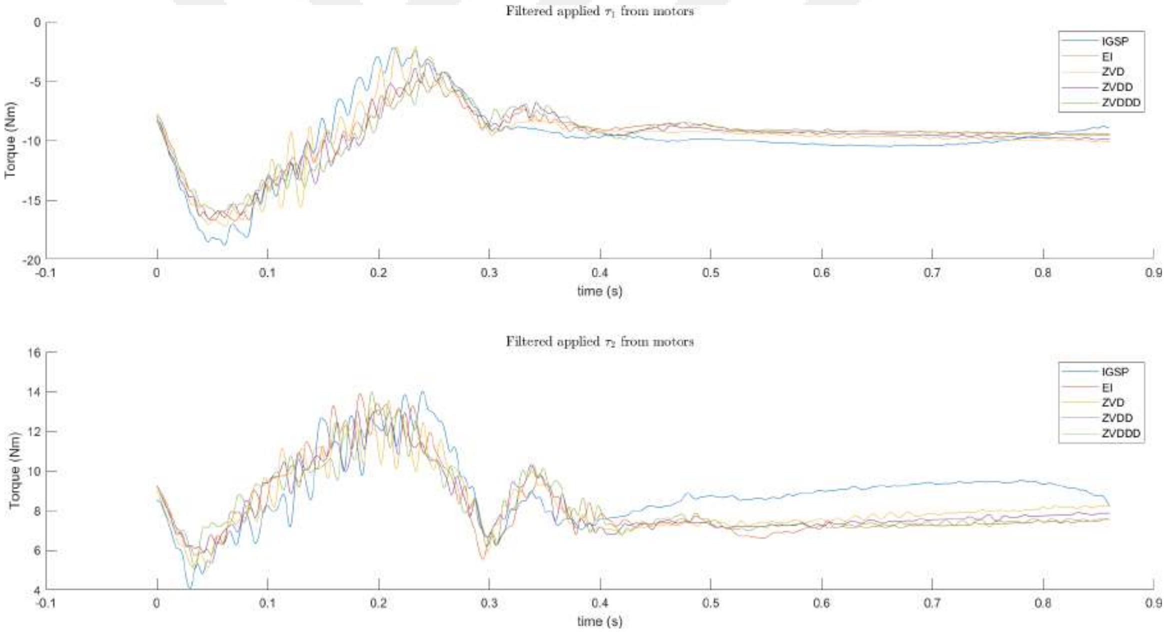

Figure A.19: Applied $\boldsymbol{\tau}$

A.2.2 Trial 2

Detailed experimental result shows in Section 3.2.2 is given below as:

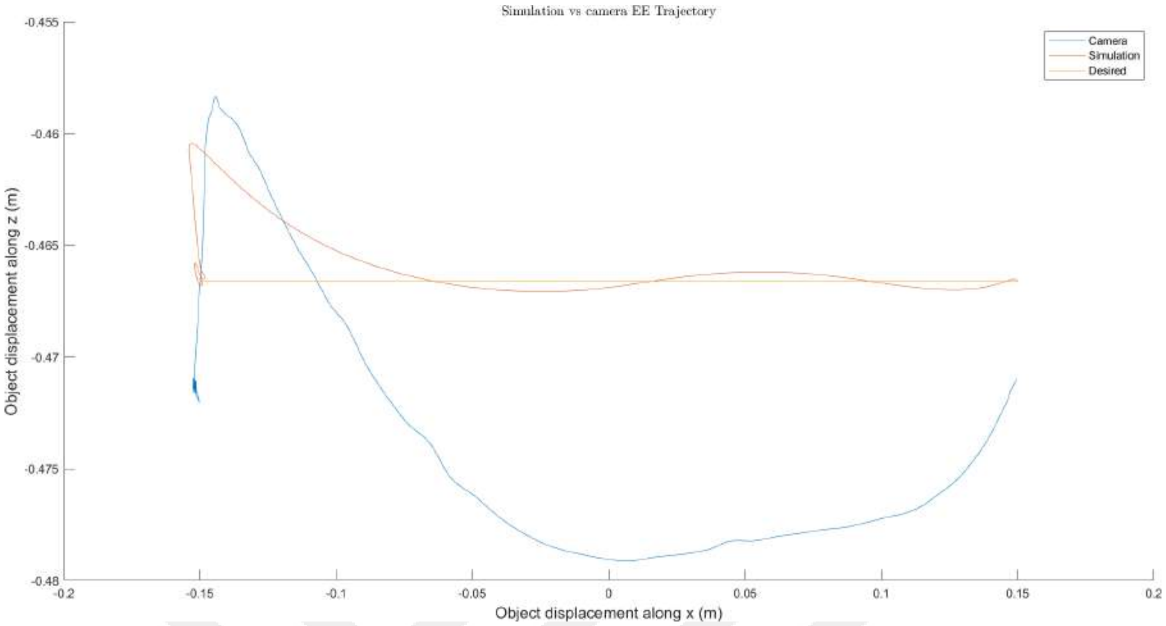

Figure A.20: EE trajectory tracking (IGSP)

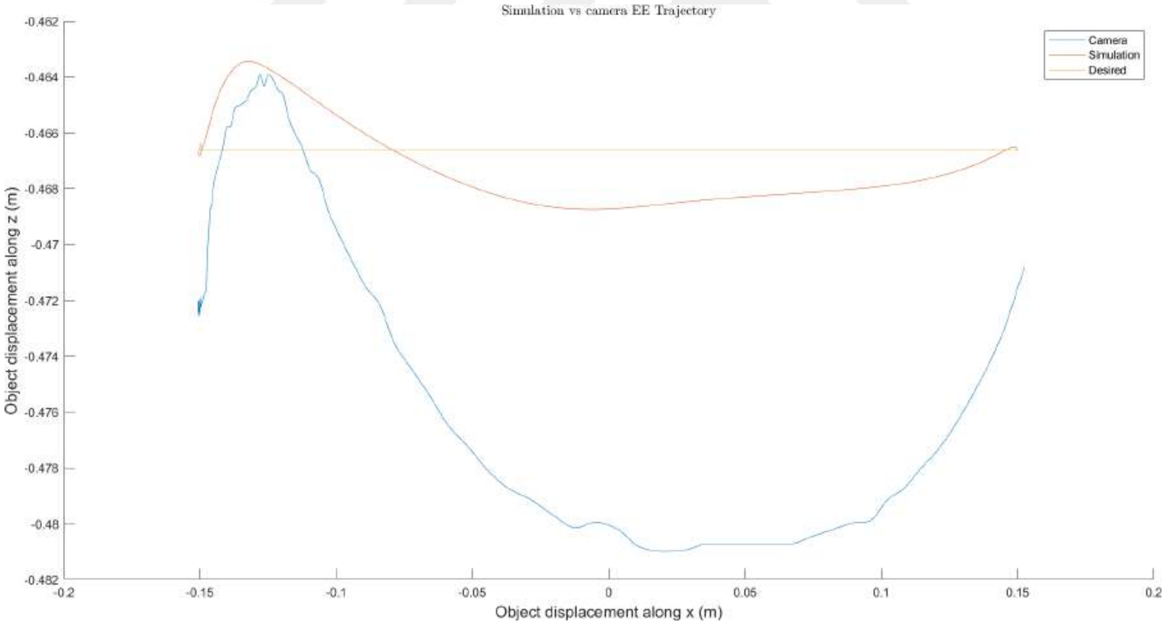

Figure A.21: EE trajectory tracking (ZVD)

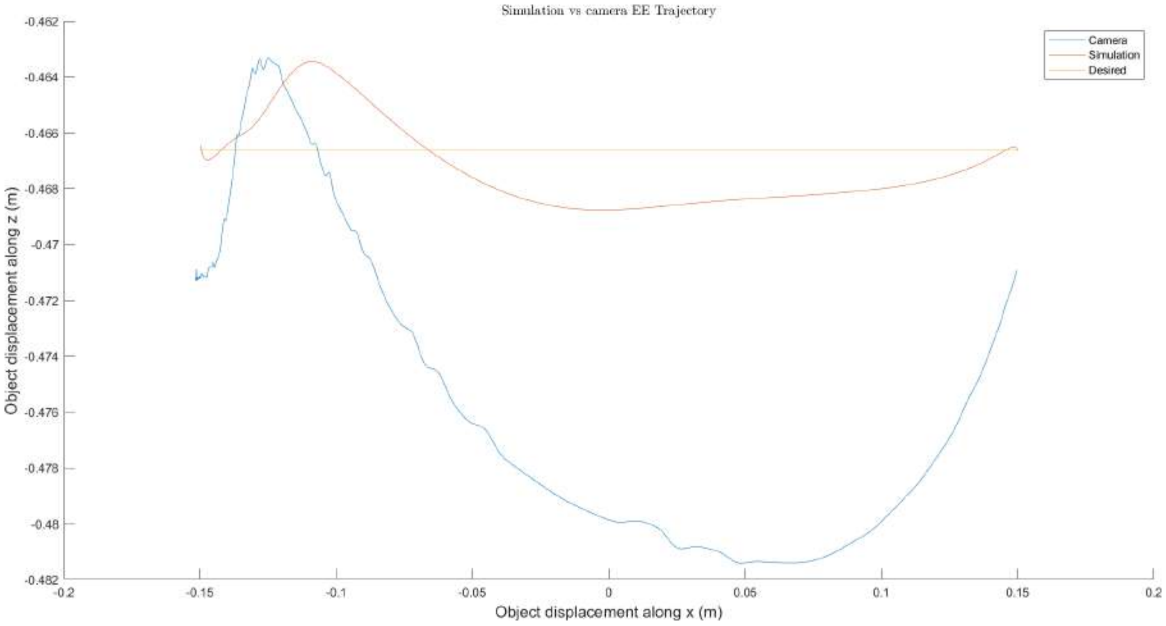

Figure A.22: EE trajectory tracking (EI)

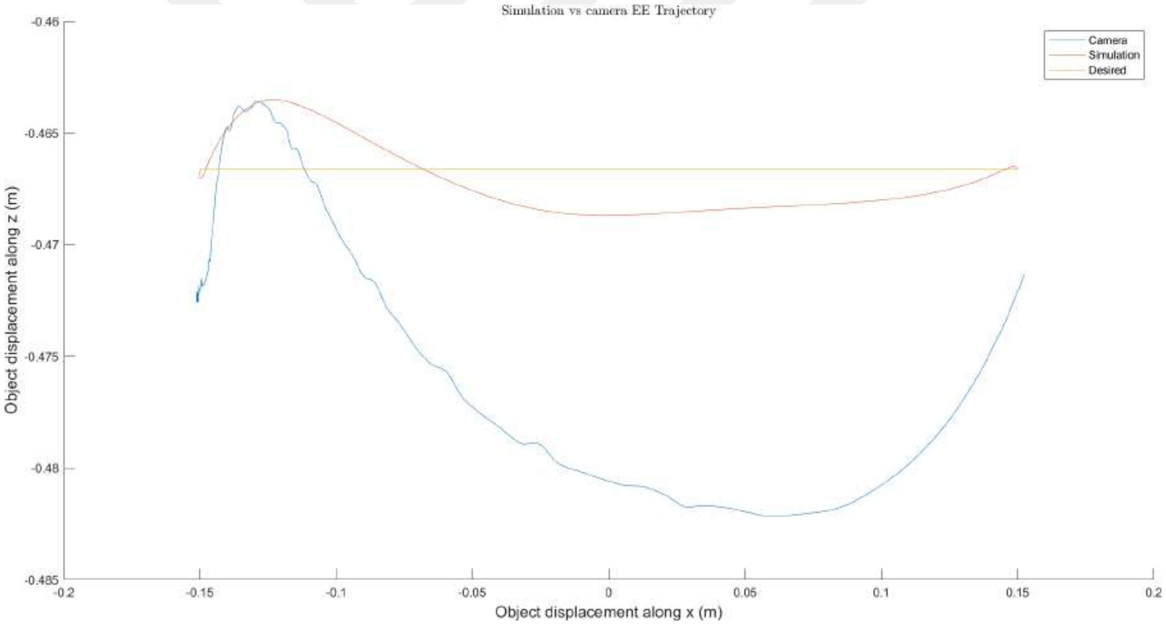

Figure A.23: EE trajectory tracking (ZVDD)

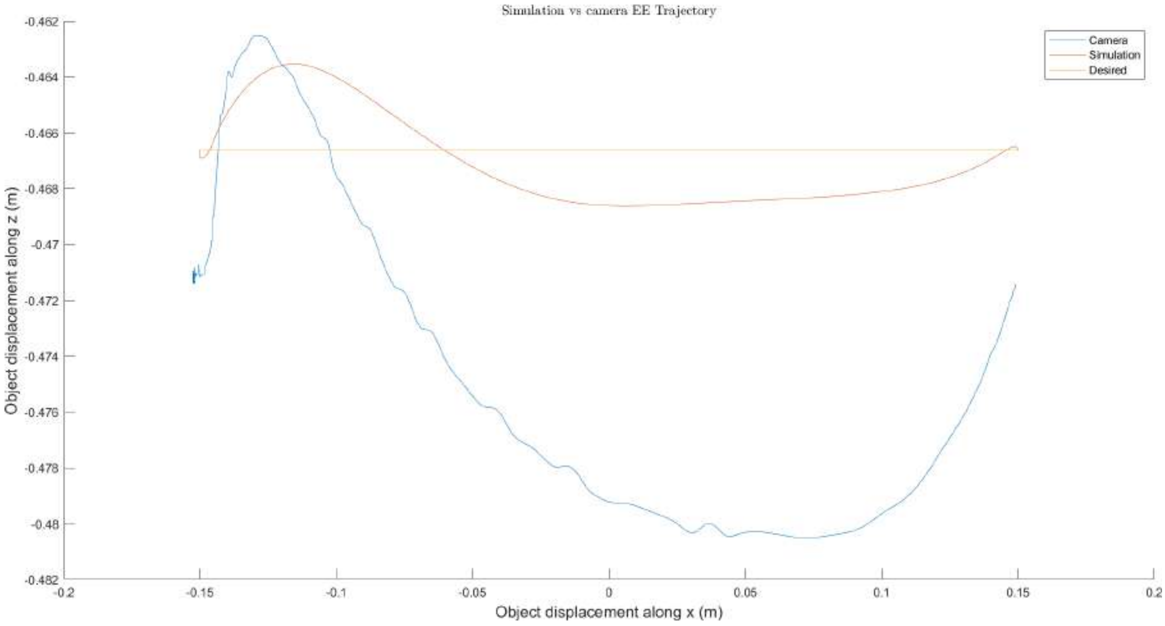

Figure A.24: EE trajectory tracking (ZVDDD)

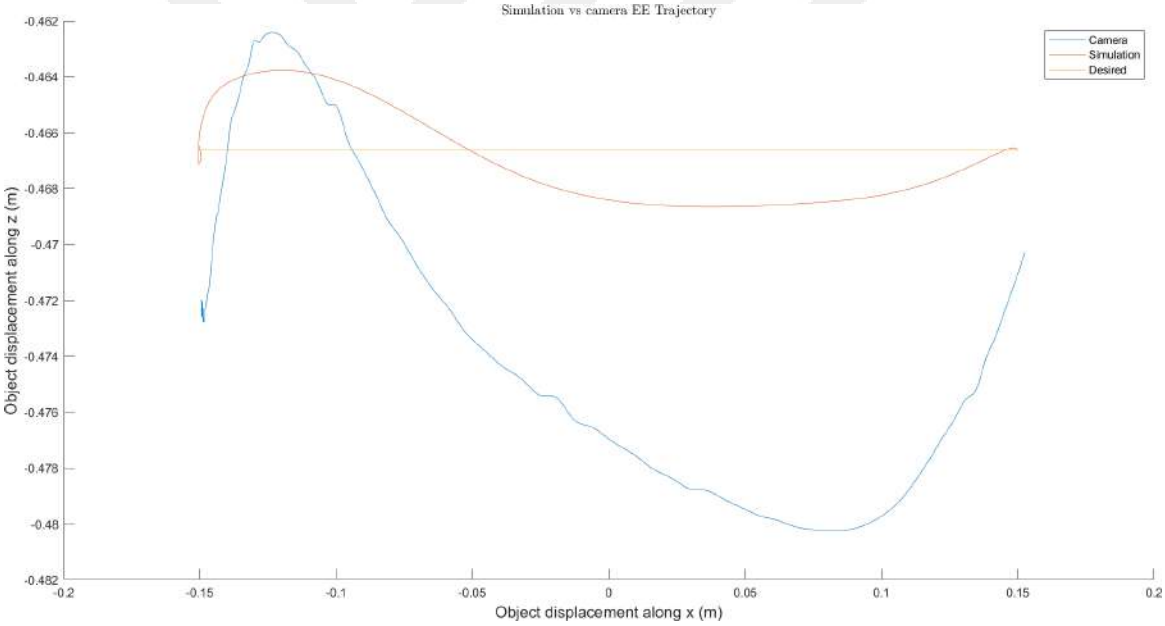

Figure A.25: EE trajectory tracking (BVP)

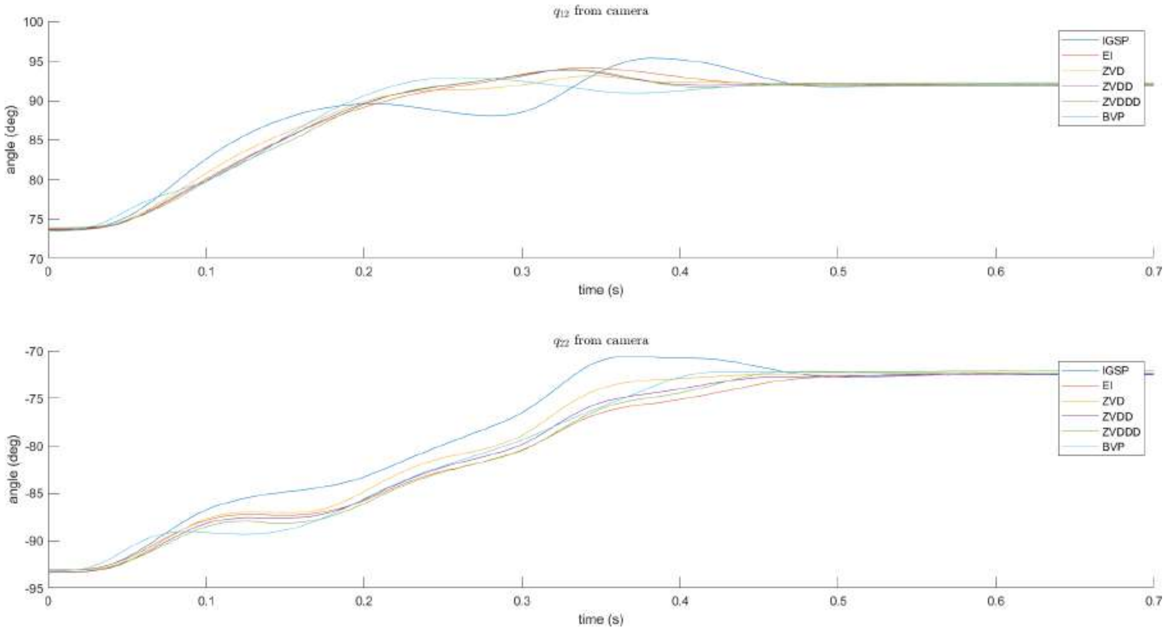

Figure A.26: Proximal unactuated coordinate oscillations

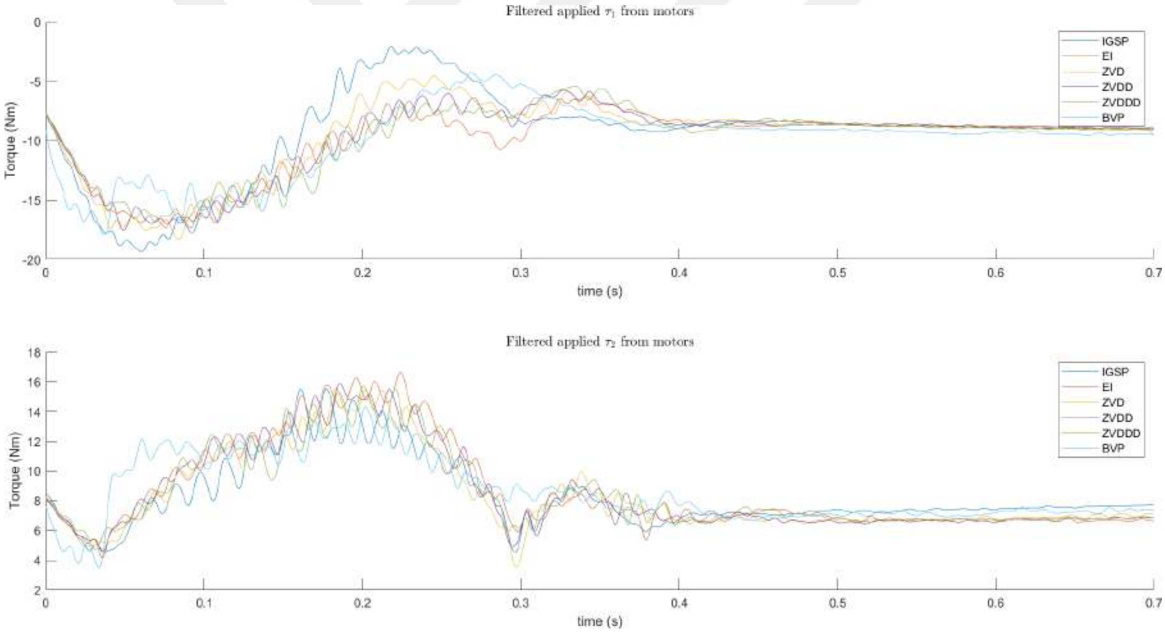

Figure A.27: Applied $\boldsymbol{\tau}$

A.2.3 Trial 3

Detailed experimental result shows in Section 3.2.3 is given below as:

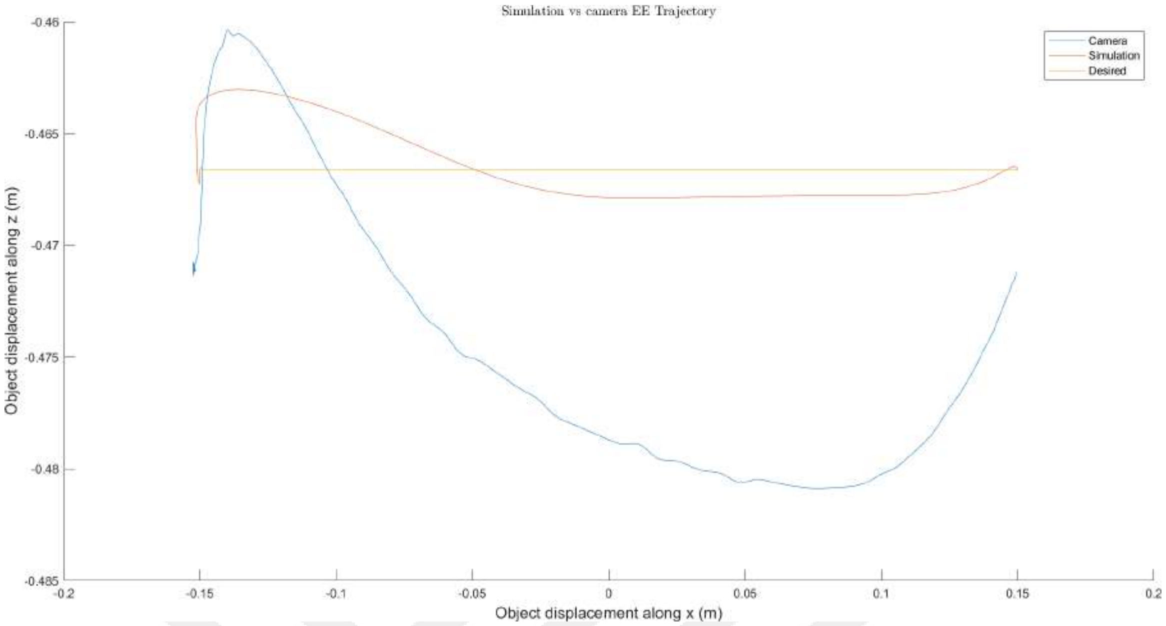

Figure A.28: EE trajectory tracking (IGSP)

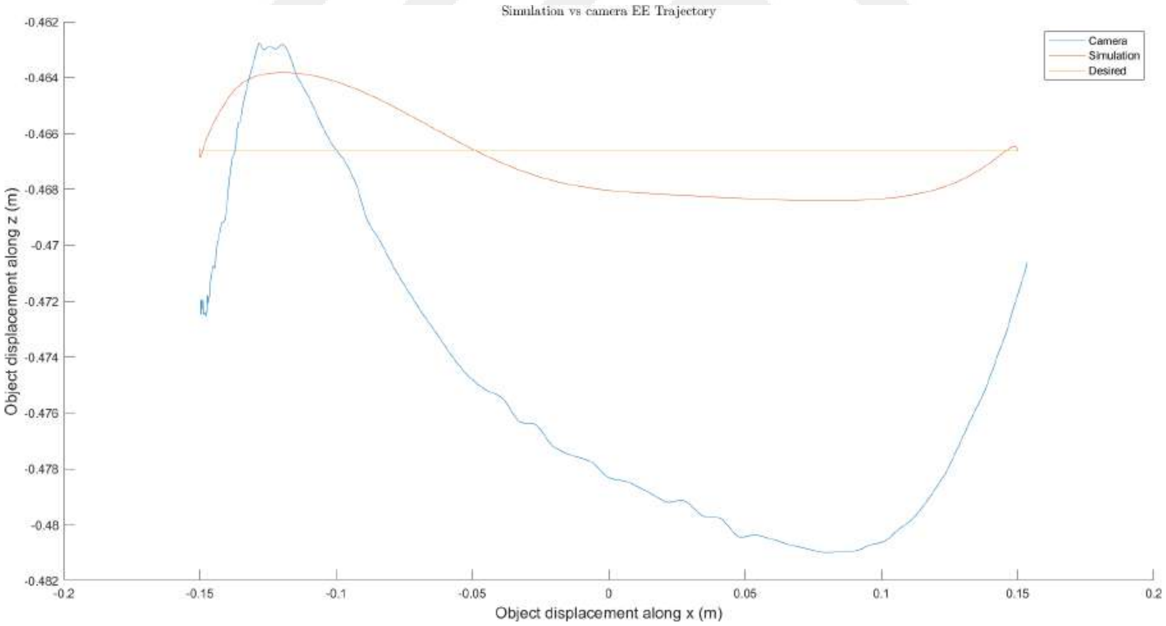

Figure A.29: EE trajectory tracking (ZVD)

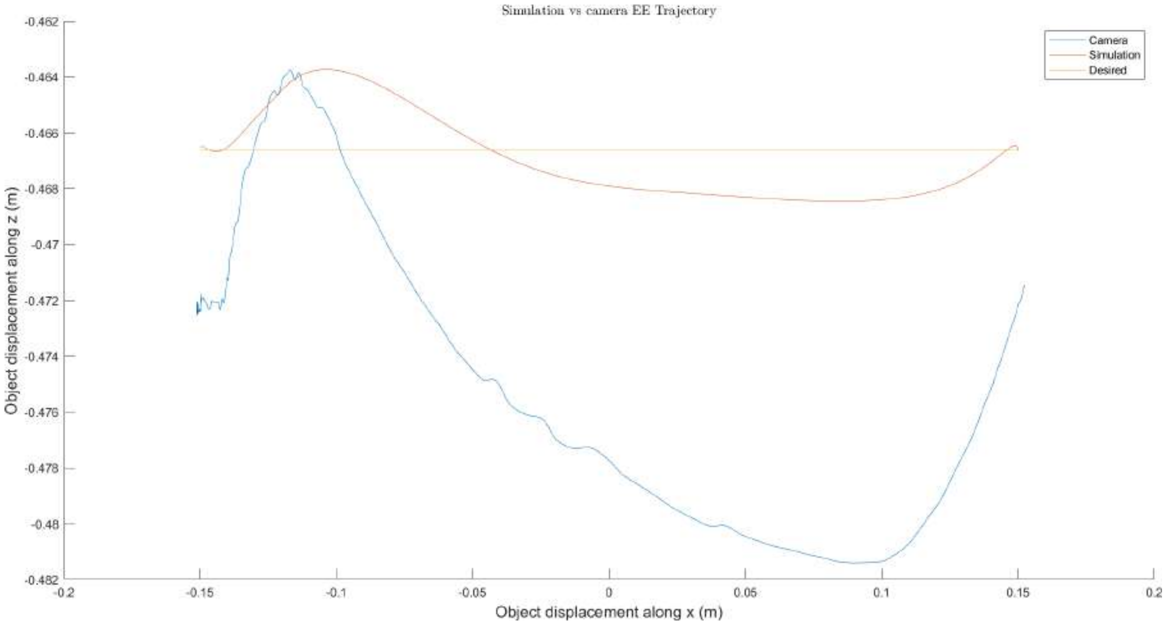

Figure A.30: EE trajectory tracking (EI)

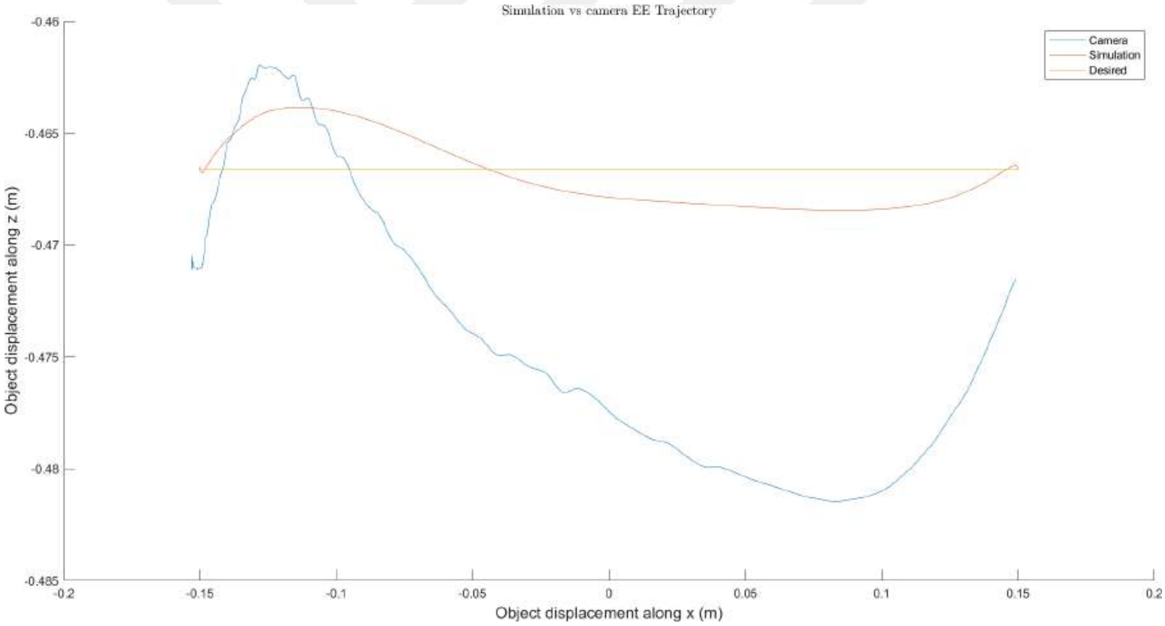

Figure A.31: EE trajectory tracking (ZVDD)

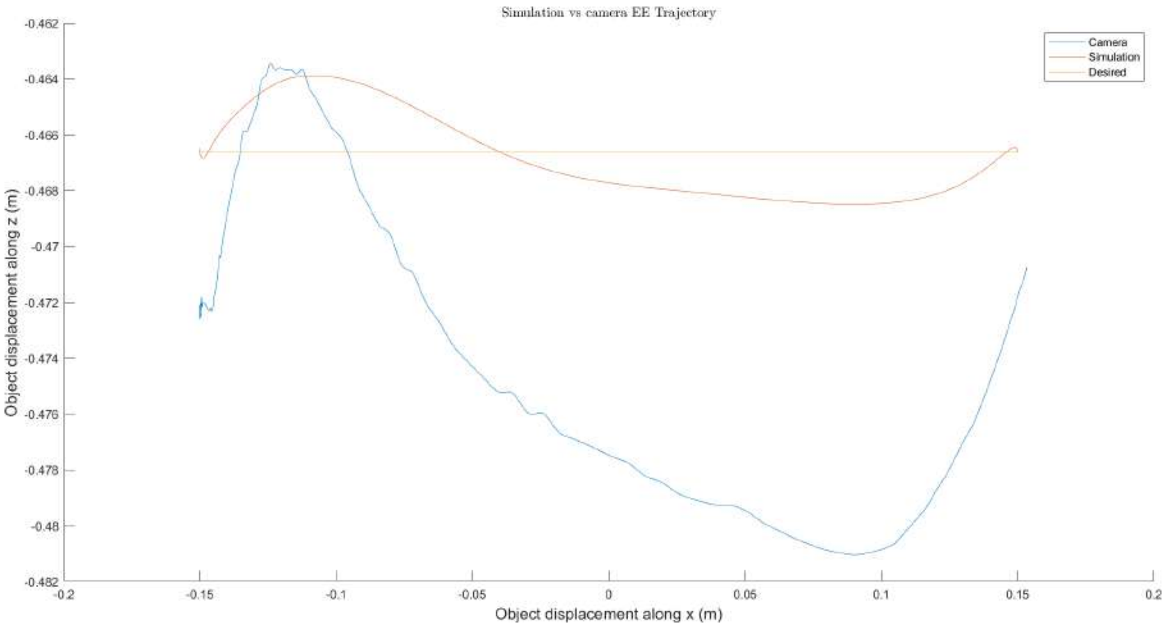

Figure A.32: EE trajectory tracking (ZVDDD)

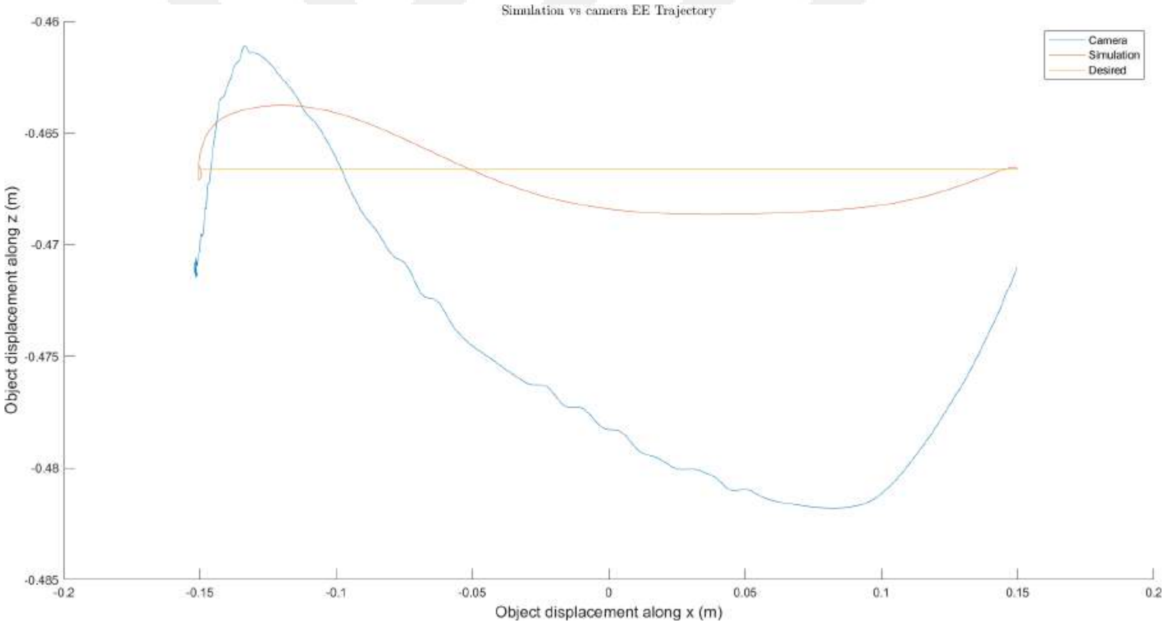

Figure A.33: EE trajectory tracking (BVP)

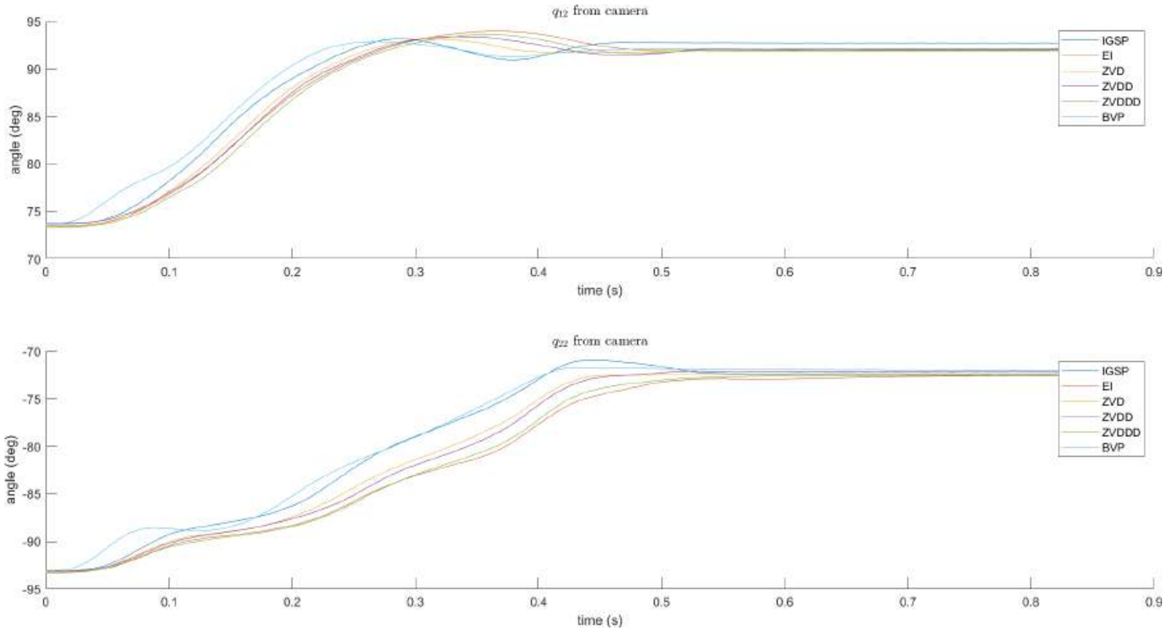

Figure A.34: Proximal unactuated coordinate oscillations

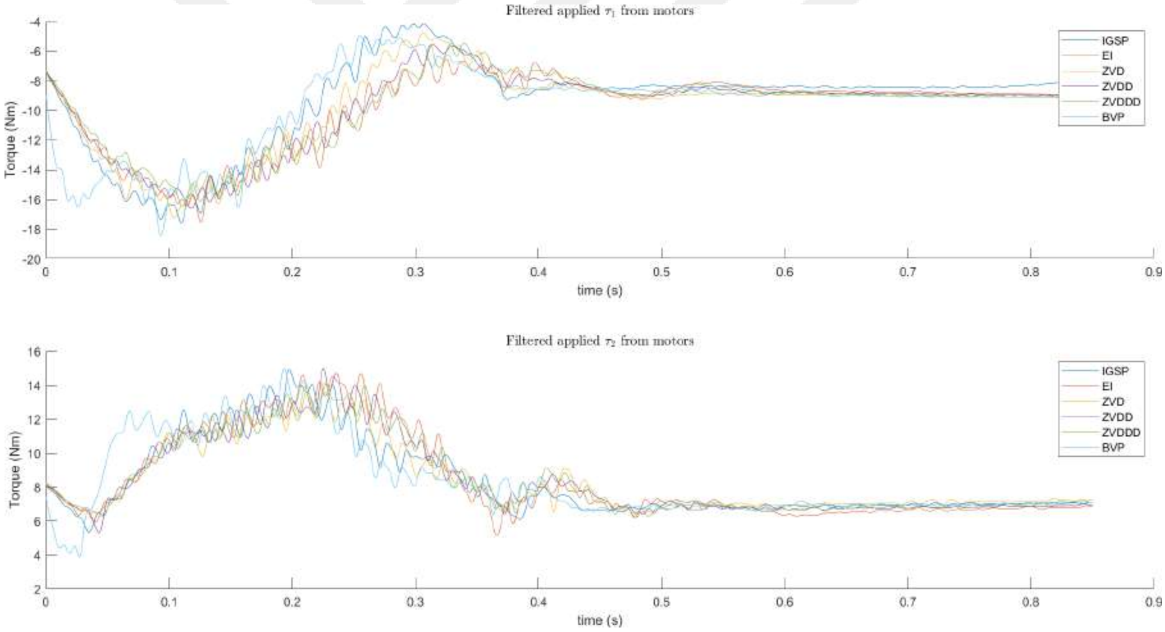

Figure A.35: Applied $\boldsymbol{\tau}$

Bibliography

[1] L. Márton, A. S. Hodel, B. Lantos, and J. Y. Hung, "Underactuated robot control: comparing lqr, subspace stabilization, and combined error metric approaches," *IEEE Transactions on Industrial Electronics*, vol. 55, no. 10, pp. 3724–3730, 2008.

[2] L. Udawatta, K. Watanabe, K. Izumi, and K. Kiguchi, "Fuzzy rules extraction by ga for controlling 2-dof underactuated planar manipulators: Switching computed torque approach," in *Proceedings of the 41st SICE Annual Conference. SICE 2002.*, vol. 4, pp. 2172–2177, IEEE, 2002.

[3] L. Udawatta, K. Watanabe, K. Izumi, and K. Kiguchi, "Control of underactuated manipulators using fuzzy logic based switching controller," *Journal of Intelligent and Robotic Systems*, vol. 38, no. 2, pp. 155–173, 2003.

[4] H. Chen and N. Sun, "Nonlinear control of underactuated systems subject to both actuated and unactuated state constraints with experimental verification," *IEEE Transactions on Industrial Electronics*, vol. 67, no. 9, pp. 7702–7714, 2019.

[5] S. U. Din, Q. Khan, F.-U. Rehman, and R. Akmeliawanti, "A comparative experimental study of robust sliding mode control strategies for underactuated systems," *IEEE Access*, vol. 5, pp. 10068–10080, 2017.

[6] R. Xu and Ü. Özgüner, "Sliding mode control of a class of underactuated systems," *Automatica*, vol. 44, no. 1, pp. 233–241, 2008.

[7] H. Ashrafiuon and R. S. Erwin, "Sliding mode control of underactuated multibody systems and its application to shape change control," *International Journal of Control*, vol. 81, no. 12, pp. 1849–1858, 2008.

[8] G. Jeanneau, V. Bégoc, and S. Briot, "Geometrico-static analysis of a new collaborative parallel robot for safe physical interaction," in *ASME 2020 International Design Engineering Technical Conferences and Computers and Information in Engineering Conference*, American Society of Mechanical Engineers Digital Collection, 2020.

[9] G. Jeanneau, V. Bégoc, S. Briot, and A. Goldsztejn, "R-min: a fast collaborative underactuated parallel robot for pick-and-place operations," in *2020 IEEE International Conference on Robotics and Automation (ICRA)*, pp. 10365–10371, IEEE, 2020.

[10] E. Idá, A. Berti, T. Bruckmann, and M. Carricato, "Rest-to-rest trajectory planning for planar underactuated cable-driven parallel robots," in *Cable-Driven Parallel Robots*, pp. 207–218, Springer, 2018.

[11] E. Idá, S. Briot, and M. Carricato, "Robust trajectory planning of under-actuated cable-driven parallel robot with 3 cables," in *International Symposium on Advances in Robot Kinematics*, pp. 65–72, Springer, 2020.

[12] V. Perrin, "Réduction des oscillations du robot r-min." Scientific Paper, 2020.

[13] D. K. Thomsen, R. Søe-Knudsen, D. Brandt, and X. Zhang, "Experimental implementation of time-varying input shaping on ur robots.," in *ICINCO (1)*, pp. 488–498, 2019.

[14] W. Singhose, E. Crain, and W. Seering, "Convolved and simultaneous two-mode input shapers," *IEE Proceedings-Control Theory and Applications*, vol. 144, no. 6, pp. 515–520, 1997.

[15] J. Vaughan, A. Yano, and W. Singhose, "Comparison of robust input shapers," *Journal of Sound and Vibration*, vol. 315, no. 4-5, pp. 797–815, 2008.

[16] S. Gürleyük and Ş. Cinal, "Robust three-impulse sequence input shaper design," *Journal of Vibration and Control*, vol. 13, no. 12, pp. 1807–1818, 2007.

[17] W. E. Singhose, W. P. Seering, and N. C. Singer, "Input shaping for vibration reduction with specified insensitivity to modeling errors," *Japan-USA Sym. on Flexible Automation*, vol. 1, pp. 307–13, 1996.

[18] D. P. Magee and W. J. Book, "The application of input shaping to a system with varying parameters," Georgia Institute of Technology, 1992.

[19] "Nonholonomic system." `https://en.wikipedia.org/wiki/Nonholonomic_system`. Accessed: 27.11.2020.

[20] "Modern Robotics, Chapter 13.3.1: Modeling of nonholonomic wheeled mobile robots." `https://www.youtube.com/watch?v=fPHVhlRFFCk`. Accessed: 27.11.2020.

[21] G. Jeanneau, "Optimization using lagrange multipliers." Seminar, 2019.

[22] "Brown University introduction to vibration of systems with many degrees of freedom." `https://www.brown.edu/Departments/Engineering/Courses/En4/Notes/vibrations_mdof/vibrations_mdof.htm`. Accessed: 2021-03-25.